Dykes and Embankments
a Geostatistical Analysis of Soft Terrain

de Gast, Tom

DOI
10.4233/uuid:4ce3b4ec-0a6a-4886-9a82-5945a1f9ea50

Publication date
2020

Document Version
Final published version

Citation (APA)
de Gast, T. (2020). *Dykes and Embankments: a Geostatistical Analysis of Soft Terrain*. [Dissertation (TU Delft), Delft University of Technology]. https://doi.org/10.4233/uuid:4ce3b4ec-0a6a-4886-9a82-5945a1f9ea50

DYKES AND EMBANKMENTS: A GEOSTATISTICAL ANALYSIS OF SOFT TERRAIN

(DEGAST)

DYKES AND EMBANKMENTS: A GEOSTATISTICAL ANALYSIS OF SOFT TERRAIN

(DEGAST)

Proefschrift

ter verkrijging van de graad van doctor
aan de Technische Universiteit Delft,
op gezag van de Rector Magnificus prof. dr. ir. T. H. J. J. van der Hagen,
voorzitter van het College voor Promoties,
in het openbaar te verdedigen op woensdag 29 januari 2020 om 10:00 uur

door

Tom DE GAST

Civiel ingenieur, Technische Universiteit Delft, Nederland,
geboren te Den Helder, Nederland.

Dit proefschrift is goedgekeurd door:

prof. dr. M. A. Hicks	promotor
dr. P. J. Vardon	promotor

Samenstelling promotiecommissie:

Rector Magnificus,	voorzitter
prof. dr. M. A. Hicks	Technische Universiteit Delft
dr. P. J. Vardon	Technische Universiteit Delft
Onafhankelijke leden:	
prof. dr. D. G. Toll	Durham University
prof. dr. S. Larsson	KTH Royal Institute of Technology
ir. H. van Hemert	Rijkswaterstaat, STOWA
prof. dr. C. Jommi	Politecnico di Milano, Technische Universiteit Delft
prof. dr. ir. S. N. Jonkman	Technische Universiteit Delft

Keywords: Field experiment, Hetereogeneity, RFEM, Site investigation, Slope failure, Statistical analysis

Printed by: IPSKAMP printing

Front & Back: Edited picture of the dyke failure test at the Leendert de Boerspolder and a numerical model mesh.

ISBN 978-94-028-1915-1

An electronic version of this dissertation is available at
http://repository.tudelft.nl/.

The presence of those seeking the truth is infinitely to be preferred to the presence of those who think they've found it.

Terry Pratchett

CONTENTS

SUMMARY

This thesis presents an investigation of the use and applicability of statistical methods in site investigation and subsequent analyses of dykes and embankments. This comprises a comprehensive site investigation via Cone Penetration Tests (CPTs) and laboratory experiments on sampled material, a large scale field test, and statistical analysis of both the site investigation data and the failure test.

This work offers the potential to better design site investigations in order to provide reliable estimates of heterogeneity and to demonstrate how these can be used in practical analyses. Such analyses are computationally expensive, but can offer significant benefits in reducing the requirements of dyke upgrades.

The controlled field experiment, in which an existing dyke was brought to failure by saturating the dyke and excavating a ditch in front (dry side) of it, is presented. To prepare for this test, an extensive site investigation was performed, consisting of Cone Peneteration Tests with measurement of water pressure (CPTu) and borings to collect material used for laboratory testing. Based on the site investigation, sensors were installed to track the behaviour of the dyke during the experiment; these included horizontal and vertical deformation sensors and pore water pressure sensors. In initial numerical analyses, the variation in material properties was not taken into account. The results of these deterministic numerical analyses and data from the failure experiment are (qualitatively and quantitatively) reasonably well-matched.

Theoretical development was undertaken in measuring and quantifying the heterogeneity (spatial correlation and point statistics), in particular, to quantify the uncertainty in the estimate of spatial correlation based on the intensity and design of the site investigation. Using synthetically generated data, the importance of the amount and spacing of information for making a reliable estimate of the SoF was demonstrated. A method has been proposed for estimating the Coefficient of Variation (CoV, standard deviation divided by the mean) of the calculated spatial correlation known as Scale of Fluctuation (SoF). The accurate estimation of the horizontal SoF using CPT within a budget is a difficult task, given the large range of values that may be expected for the horizontal SoF. However, grouping CPTs can yield an improved estimate of the SoF with a limited number of CPTs, given no prior knowledge of the SoF.

The developed methods were applied to the field site CPT data. The analysis revealed a difference between the vertical and horizontal SoF. Based on these results, the horizontal SoF was seen to be better represented by the weighted average of two component scales of fluctuation, whereas the vertical SoF was adequately described by a single SoF. This is hypothesised to be due to be a combination of natural geological processes and anthropogenic maintenance.

A method to utilse the measures of heterogeneity and uncertainty in slope stability analyses is the Random Finite Element Method (RFEM). The conditions before the field experiment started and at failure were compared in a series of numerical analyses using

deterministic FEM and RFEM approaches. It was shown that by utilising the measures of heterogeneity and as much of the available data as possible, including their locations, gave those results which best fitted the test results.

The observed and calculated failure modes were similar, although the computed factors of safety differ significantly depending on the adopted approach (deterministic FEM versus RFEM) and on the relative use of data (i.e. conditional versus unconditional analysis). Using the measured heterogeneity allows the quantification of uncertainty. By incorporating heterogeneity, the confidence in the stability assessment can generally be increased, and by incorporating the location of the measurements the confidence can usually be further increased. This resulted in a method to enable dyke systems to be analysed in a more accurate and less conservative manner, which can lead to better choices in dyke maintenance and re-design.

SAMENVATTING

Dit proefschrift presenteert een onderzoek naar het gebruik en de toepassing van statistische gegevens uit grondonderzoeksdata en het gebruik van deze gegevens in de analyse van dijkstabiliteit. Het werk heeft bestaan uit een uitgebreid grondonderzoek met behulp van sonderingen (CPT) en boringen, en laboratoriumonderzoek op geselecteerde monsters, het gecontroleerd laten bezwijken van een dijk en een statistische analyse op het grondonderzoek en de bezweken dijk.

Dit onderzoek geeft een richting voor het beter ontwerpen van grondonderzoek om betrouwbaar de heterogeniteit vast te kunnen stellen en heeft gedemonstreerd hoe deze gebruikt kan worden in geotechnische analyses. De gebruikte analyses vereisen aanzienlijke rekentijd maar hebben significante voordelen in het reduceren van de benodigde verbeteropgave ten opzichte van traditionele stabiliteitsanalyses.

In het veldexperiment is een bestaande dijk tot bezwijken gebracht door eerst de dijk te verzadigen en vervolgens de teen van de dijk te ontgraven. Voorafgaand aan het experiment is een uitgebreid grondonderzoek uitgevoerd bestaande uit sonderingen met meting van de waterspanning (CPTu) en mechanische boringen om monsters te verzamelen voor het laboratoriumonderzoek. Hierna zijn op basis van het grondonderzoek, sensoren geïnstalleerd om het gedrag van de dijk tijdens het experiment te volgen. Met deze sensoren zijn de horizontale en verticale deformaties en de waterspanningen gemeten. In de initiële numerieke analyses, is de variatie in materiaalparameters buiten beschouwing gelaten. Deze deterministische numerieke analyses komen zowel kwalitatief als kwantitatief goed overeen met de data van het bezwijkexperiment.

Het meten en kwantificeren van heterogeniteit (ruimtelijk variatie, gemiddelde en standaarddeviatie), specifiek het kwantificeren van de onzekerheid in de schatting van de ruimtelijke correlatie op basis van de intensiteit en de plaatsing van het grondonderzoek is verbeterd. Met synthetisch gegenereerde data is het belang van de hoeveelheid en tussenafstand van data voor het bepalen van de ruimtelijke variatie beschouwd. Er is een methode gepresenteerd voor het schatten van de variatiecoëfficiënt (CoV, standaarddeviatie gedeeld door het gemiddelde) van de berekende ruimtelijke variatie ook bekend als Scale of Fluctuation (SoF). Het economisch nauwkeurig schatten van de horizontale SoF met sonderingen is niet eenvoudig, gegeven de grote variatie in verwachtte horizontale SoF. Als er vooraf geen gegevens over de SoF zijn en een beperkt aantal sonderingen beschikbaar is, kan het groeperen van de sonderingen tot een verbeterde schatting van de SoF leiden.

De ontwikkelde methoden zijn toegepast op de CPT velddata. Bij de analyse hiervan is aangetoond dat er een verschil tussen verticale en horizontale SoF aanwezig is. Op basis van de gevonden autocorrelatie functies, kan de horizontale SoF beter geschat worden door twee (gewogen) auto-correlatiefuncties te gebruiken. De verticale SoF kan goed beschreven worden door een enkele auto-correlatiefunctie. Er wordt aangenomen dat dit

het resultaat is van een combinatie van natuurlijke geologische processen en onderhoud door de mens.

Een methode om de mate van heterogeniteit en onzekerheden in dijkstabiliteit te benutten is de Random Finite Element Method (RFEM). De initiële fase, voor de start van de test, en de eindfase van de test zijn vergeleken in een serie numerieke analyses waarin zowel FEM als RFEM gebruikt is. Het is aangetoond dat met het gebruik van de gemeten heterogeniteit en zoveel mogelijk beschikbare data inclusief de locatie van de data, de resultaten van de RFEM analyses het best overeenkomen met de data van het bezwijktest.

De geobserveerde en berekende glijvlakken zijn vergelijkbaar, maar afhankelijk van de toegepaste methode (deterministische FEM of RFEM) en de gebruikte hoeveelheid data (geconditioneerde of ongeconditioneerde analyse) verschillen de berekende stabiliteitsfactoren significant. Door gebruik te maken van de gemeten heterogeniteit kan de onzekerheid gekwantificeerd worden. Door heterogeniteit als factor toe te voegen in de stabiliteitstoets wordt de betrouwbaarheid van de stabiliteitstoets over het algemeen verbeterd. Door daarnaast ook de locaties van de metingen toe te voegen kan de betrouwbaarheid nog verder verbeterd worden. Dit heeft geresulteerd in een methode waarmee dijkstrekkingen nauwkeuriger en minder conservatief beoordeeld kunnen worden, waarmee betere keuzes in dijkonderhoud en herontwerp kunnen worden gemaakt.

LIST OF SYMBOLS

ACRONYMS

1D	1 Dimensional
2D	2 Dimensional
3D	3 Dimensional
C	Conditional
CMD	Covariance Matrix Decomposition
COW	Centrum Onderzoek Waterkeringen
CPT	Cone Penetration Test
CPTu	Cone Penetration Test with measurement of water pressure
CRS	Constant Rate of Strain
DEGAST	Dykes and Embankments: a Geostatistical analysis of Soft Terrain
DSS	Direct Simple Shear
ENW	Expertise Netwerk Waterveiligheid
FEM	Finite Element Method
IPO	Interprovinciaal Overleg
K_0-CRS	Constant Rate of Strain including measurement or radial stress
LAS	Local Average Subdivision
LEM	Limit Equilibrium Method
MCM	Monte Carlo Method
NAP	Normaal Amsterdams Peil (reference level)
NDFT	Non-uniform Discrete Fourier Transform
RFEM	Random Finite Element Method
RLEM	Random Limit Equilibrium Method
SoF	Scale of Fluctuation
STOWA	Stichting Toegepast Onderzoek Waterbeheer
TxCU	Isotopically Consolidated Undrained Triaxial tests
UC	Unconditional
UTC	Coordinated Universal Time / Temps Universel Coordonné
WFD	Water Framework Directive

LATIN SYMBOLS

c'	effective cohesion
c_i	weights for weighted average
CoV	coefficient of variation

D	domain length
D_g	domain length of a cpt group
D_t	domain length of all data
D_p	perpendicular domain length
$Er(x), Er(\rho)$	error of x or ρ
E'	effective Young's modulus
F	factor of safety
F_{2D}	factor of safety for a 2D section
F_{3D}	factor of safety for a 3D section
f_r	sleeve friction
$G_{(\omega_k)}$	spectral density function
in	interval between data points
j, k, l, t	various counters
k	constant (0.7) in Equation (1.4)
K	constant (10.6) in Equation (1.4)
K_0	at rest stress ratio
$k_{x,y}$	hydraulic conductivity
n	number of data points
n_t	number of frequencies considered
N_{kt}	empirical correction factor for shear strength from CPT
nf	number of independent data sets
nf_{max}	maximum number of independent data sets
ng	number of data groups
q_t	corrected cone resistance
$r_{n,V}$	factor for measure of the distribution of the shear strength
s'	effective mean stress
s_u	undrained shear strength
$s_{u,\mu}$	mean undrained shear strength
$s_{u,\sigma}$	standard deviation of undrained shear strength
t	deviatoric stress
t	number of pairs of data at lag distance τ
u_2	water pressure (behind the cone)
W, X, Y, Z	parameters of Equation (3.16)
x_j	data point
y_j	data point
y'_j	data point at location separated by a lag distance

GREEK SYMBOLS

β	reliability index
γ	unit weight
γ_d	sensitivity factor for the calculation method
γ_{dry}	dry unit weight
γ_g	global reduction factor
γ_m	material reduction factor

γ_n	damage factor
γ_{sat}	saturated unit weight
$\hat{\gamma}(\tau)$	experimental covariance function
$\Gamma^2(x)$	reduction factor
Δj	index difference
θ	scale of fluctuation (auto-correlation length)
θ_{avg}	average scale of fluctuation
θ_{com}	scale of fluctuation, part of a combined auto-correlation function
θ_e	equivalent scale of fluctuation
θ_{max}	maximum scale of fluctuation investigated
θ_h	horizontal scale of fluctuation
θ_i	component of the scale of fluctuation
θ_p	perpendicular scale of fluctuation
θ_v	vertical scale of fluctuation
μ	mean (or trend)
$\hat{\mu}$	estimated mean (or trend)
ν'	effective Poisson's ratio
ρ	correlation
$\rho(\tau)$	auto-correlation function
ρ_{com}	combined autocorrelation function
ρ_{θ_i}	component of a combined autocorrelation function
$\hat{\rho}(\tau)$	experimental autocorrelation function
σ_v	total vertical stress
σ	standard deviation
τ	shear strength
τ	lag distance
ϕ'	effective friction angle
ω_k	domain frequency

1

INTRODUCTION

Section 1.4 is based on de Gast *et al.* (2015)

1

1.1. INTRODUCTION

There is a continuous need to maintain and improve the geotechnical safety of dykes in delta regions throughout the world. In the Netherlands, regular (regional) dyke assessment is one part of reducing the risk of flooding. Specifically, ~18 000 km of dykes are assessed at regular intervals, of which 14 000 km are classified as regional dykes (STOWA, 2005) and do not protect against flooding from major rivers or the sea. The methods of assessing regional dykes are strongly intertwined with the methods of assessing primary dykes; however, they differ due to the lower risk levels and significantly shorter lengths.

Around 1 billion euros per year are required to maintain and upgrade the Dutch dyke network (Veerman *et al.*, 2008), which protects around 40% of the Netherlands from inundation by the sea or by rivers. Research is needed to improve understanding in dyke geo-engineering, so that: (a) financial savings can be made; and (b) financial resources can be more effectively focussed in areas of real need. In particular, there is a need to fill knowledge gaps relating to the 14,000 km of regional dykes, which are currently maintained and upgraded using rules mainly derived from research on primary dykes (a very different type of structure). Both types of dyke are often founded on soft soils, but, whereas primary dykes are mainly engineered using selected sand or clay, regional dykes may be constructed of locally found clays, peat, debris, and occasionally sand. Moreover, the hydraulic boundary conditions are different: primary dykes are designed to withstand tidal, storm and wave loadings, whereas regional dykes are characterised by artificially controlled high water tables, with, in general, only 10-20 cm change in external water level and only small wind waves due to the size of the water areas.

Initially, local experience was relied upon for maintaining dykes, prior to the utilisation of calculations based on soil mechanics to determine the safety/stability of dykes. Over the years, new approaches have been developed leading to different assessment criteria.

The current assessment criteria for regional dykes in Dutch norms/guidelines were initially developed and subsequentially evolved after the devastating storm surge of 1953. They started with the probabilistic assessment of water heights and global factors of safety for slope stability, and progressed through to the adaption of statistical models which enabled the use of partial factors in dyke assessment. Partial factors allow for the inclusion of improved and more detailed knowledge, which limit the uncertainties and the level of acceptable risk in the calculation. The introduction of risk-based design enables assessment criteria based on the expected damage due to inundation.

In this thesis, the development of the statistical approach is more fundamentally and comprehensively addressed than by applying partial factors. The development of the use of partial factors in the Netherlands is adressed in Section 1.4. That approach includes conservative estimates of the strength of the material and has led to the calculation of very low factors of safety (as low as 0.35) for existing embankments, some of which have remained standing for hunderds of years. However, by applying the full distribution of the material properties, including the heterogeneity within a soil layer, a better picture is obtained of how stable an embankment really is. By linking this approach with the results of a field test in this thesis, a deterministic solution of a failure may be compared to the statistical approach.

1.2. RELIABLE DYKES

This thesis has been written as part of the Nederlandse Organisatie voor Wetenschappelijk Onderzoek (NWO) Toegepaste en Technische Wetenschappen (TTW) programme Reliable Dykes, which aims to provide industry with focused scientific insight relating to regional dykes. This research programme has focused on quantifying and analysing the impact of uncertainties in the assessment of regional dykes, with 4 PhD projects examining different aspects: The first PhD (this thesis) has focused on a full-scale dyke failure experiment and simulating the induced failure with the Random Finite Element Method (RFEM), as well as the measurement of soil heterogeneity and linking of these measurements with the induced failure; the second PhD focussed on the material behaviour of peat, a material which is found in the structure of several thousand kilometres of dykes; the third PhD is further developing RFEM analysis techniques, including the consideration of geometry variation in 3D and the benchmarking and upgrading of simplified semi-analytical methods; and the fourth PhD, is examining the soil-atmosphere interaction and hydraulic conditions during dyke operation. In addition, a post doctoral researcher has been building geomechanical assessment tools to link the different projects for the needs of industry partners, and, in particular, investigating the simulation of low probability failure events. The project began in 2014 and is expected to finish in 2020.

1.3. FACTORS OF SAFETY ACCORDING TO EUROCODE 7

Eurocode 7 stipulates (partial) factors of safety to account for uncertainty in material properties, loads and the effect of loading, as reviewed by Orr (2000). The distribution of partial factors for these uncertainties follows three different approaches:

1. Two combinations of partial factors are checked. The first combination checks the effects of the loads, whereas the second combination checks the resistance effects. This approach is primarily concerned with uncertainties in favourable permanent loads and unfavourable variable loads, and is most applicable for problems where the hydrostatic forces are the main loads and soil strength has little contribution.

2. Partial factors are applied to the resistance, and on the variable actions or the effects of these actions. This approach is mainly concerned with actions that are uncertain and is most applicable for problems where the response of the soil is sensitive to the loading.

3. Partial factors are applied on the loads and load effects from the structure, and to the material parameters. This approach is mainly concerned with uncertainties in the soil properties, and is most applicable for problems where the soil determines the size of the structural elements in the gound.

All three design approaches require characteristic input parameters. Marques *et al.* (2011) discussed, via the example of a strip foundation on a $c' - \phi'$ soil and various semi-probablistic approaches, the effect of the input parameters on the reliability index. They showed that for a given characteristic value, the target reliablity varies significantly with the different design approaches.

Soil heterogeneity influences the reliability of geotechnical structures. Therefore, choosing a characteristic value depends on the geometry of the geotechnical structure, the nature of the loading, and the spatial variation of soil properties in the ground.

1.4. THE HISTORY OF FACTORS OF SAFETY FOR DUTCH REGIONAL DYKES

A brief history of the development of design safety required in the Netherlands is given below as an example of how safety has been considerd and addressed over time. While the Delta Works were still being constructed to reduce the coastal length of the Netherlands, on 14 January 1960 a breach of a regional dyke protecting the Noorder IJpolder occurred, flooding the Amsterdam district Tuindorp Oostzaan and triggering a long term research initiative to assess the safety of the Dutch polders against flooding. The methods and guidelines for the assessment are described in Belgraver (1973), and the assessments were also performed by Centrum Onderzoek Waterkeringen (COW), which was part of Rijkswaterstaat. However, added information, experience, research and increases in computing power have led to changes in the assessment criteria over the years. This section discusses the various assumptions that have been made and their effects on the required (global) factor of safety.

The initial guideline (Belgraver, 1973) was based on experience gained from 11 assessed dykes and archive data on past dyke failures. Different failure mechanisms which need to be taken into account during an assessment were discussed: overtopping, breaching, erosion, elements with significant stiffness difference, construction and (lack of) maintenance. In this initial guideline, the main focus for the assessment was based on breaching, overtopping and erosion, which are considered to be slow failure mechanisms that 'announce' themselves. In contrast, elements with significant stiffness difference (construction), and maintenance are temporary and very local occurrences. This section focuses on the prevention of breach and associated slope stability analysis.

Here, only the circular Bishop slope stability method is considered to calculate stability. Specifically, an overview is given on the changes in assessment criteria, in chronological order, which led to different factors of safety. For the purpose of comparison over time, partial factors (introduced in 1993) have been converted to global reduction factors using the formulae:

$$\frac{F}{\gamma_g} \geq 1 \tag{1.1}$$

$$\gamma_g = \gamma_d \gamma_m \gamma_n \tag{1.2}$$

where F is the calculated factor of safety, γ_g is the global reduction factor, γ_d is the sensitivity factor for the calculation method, γ_m is the material reduction factor and γ_n is the damage factor.

The calculated stability factor F is divided by γ_g to give a combined factor of safety (FoS) that should be equal to, or greater than, one. The comparison of the global reduction factors (which is the same as the required calculated factor of safety) is presented in Figure 1.1. For the case in which the required partial material factors for cohesion and friction

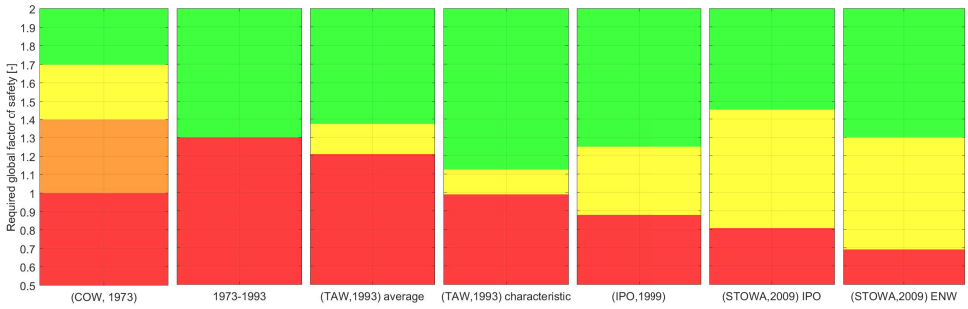

Figure 1.1: Overview of the required global factors of stability for regional dykes (1973 to the present day). In red (lowest), stability factor not acceptable; in orange, more detailed research is required; in yellow, acceptable depending on the material and economic value of the polder; and in green (highest), acceptable.

angle are different from each other, an average partial material factor was used. This section provides an overview of the changes in the assessment methods indicated in Figure 1.1.

COW (1973)

The Belgraver (1973) assessment was based on average values of material properties obtained from local site-investigation and laboratory testing (Dutch cell test). The stability factor was calculated using Bishop (1955), chosen because it was the most (internationally) accepted method to calculate slope stability at that time. However, Belgraver (1973) noted that Bishop's method was unsuitable in very deformable (soft) soils, because failure was expected not to be circular and anisotropy and heterogeneity would influence the shape of a possible failure. In small embankments, low stresses, cohesion, shear cracks and the shape of the failure mechanism can lead to large errors. The factors of safety presented in yellow in Figure 1.1 give a range of safe values, based on the unit weight of the material and the number of laboratory tests performed on the material. If the calculated stability factor was in the orange range in Figure 1.1, more investigation was required before the dyke safety could be considered acceptable. A stability factor lower than 1.0 was never deemed acceptable.

This assessment was explicitly based on information from the cross-section being evaluated; therefore, the calculated stability was not a combination of worse case geometry, soil profile and material properties.

1973-1993

According to TAW (1993) and van Hemert (2007), the required global factor of safety before 1993 was 1.3, altough the author has not found original documents reporting this required global factor of safety. This single value is lower than all single values required for unconditional approval by Belgraver (1973).

TAW (1993)

In 1993, partial factors were introduced. The sensitivity factor γ_d was introduced to account for uncertainty in the calculation method, and given a value of 1.0 for Bishop's analysis.

The material factor γ_m was introduced to account for uncertainty in the material and determination of material parameters. The material factor for cohesion was a constant (value), whereas the material factor for friction angle changed with the type of material and type of laboratory test used to determine the friction angle. The material factors were equal to these listed in TAW (1993), a guideline for primary dykes, and range from 1.10 to 1.25.

The damage factor γ_n was introduced to account for the consequences of inundation. This was varied based upon the method being used to obtain the material parameters. In calculations using average strength parameters, γ_n was 1.1, whereas, for the case in which the characteristic strength was determined according Belgraver (1993), γ_n was 0.9.

Belgraver (1993) reported that the damage factor was chosen so as to keep the global factor equal to 1.3 by using,

$$\gamma_n = 1.3 \frac{r_{(n,V)}}{(\gamma_d \gamma_m)} \tag{1.3}$$

where $r_{n,V}$ is a factor given in Belgraver (1993) representing a measure of the distribution of the shear strength, stated as ≈ 0.85. γ_m is therefore responsible for the range of required FoS for the ranges (Belgraver, 1993) in Figure 1.1. Changing to the use of partial factors should give the opportunity of different uncertainties being evaluated independently. To avoid complications when updating uncertainties, partial factors have to be independent. However, γ_n was chosen to prevent change in the required global factor of safety.

For the Bishop calculation the value of the sensitivity factor γ_d is taken to be 1.0, which implies a perfect calculation model, as the calculated stability factor is not reduced in contrast to the note in Belgraver (1973).

Applying characteristic values leads to a cautious estimate of the slope stability. However, the cautiousness of the estimate is reduced when a γ_n of less than 1 is applied.

IPO (1999)

The economic implications of inundation were taken into account in van der Meer (1999). The polders were divided into 5 different classes, with different safety norms of once per 10, 30, 100, 300 and 1000 years. These safety norms are translated into a reliability index β using the inverse of the standard normal distribution. The obtained β was used in Equation (1.4) to approximate the required damage factor,

$$\gamma_n = \frac{(K * k)}{(K - \beta)} \tag{1.4}$$

where β is the reliability index, k is stated to be 0.7, and K is stated to be 10.6; and K is said to depend on the ratio between the effect of the cohesion and friction angle on the stability, the coefficients of variation of the cohesion and friction angle, and the location of the phreatic surface. k was defined based on γ_d, γ_m and the range of shear strength parameters, $r_{n,V}$.

The required damage factor was implemented into the assessment. The requirements for a type III polder (safety norm 1/100 year) are the same as in the assessment according to TAW (1993), i.e. γ_n is equal to 0.9. A range of γ_n from 0.8 – 1.0 using Equation (1.4) leads to an equivalent β of 1.3 – 3.2.

Splitting the partial factors based on expected damage can improve the allocation of funds for maintenance and improvement, and fits in a risk-based framework where the costs are weighted to the expected benefits.

However, as γ_n is derived from the effects of the material parameters on shear strength, and effects of phreatic line and variation coefficients of friction angle ϕ' and cohesion c', it remains a mixed parameter depending on the expected damage, material and sensitivity of the calculation. Because the range of γ_n is increased, the range of required global factors of safety also increases.

STOWA (2007)

After the failure of a peat dyke during a dry summer in 2003, a new standard for the assessment of regional dykes was introduced. This standard collected the assessment methods from previous standards, added a drought criterion and became the new standard. The requirements for the macro stability assessment did not change (van der Meer, 1999), and therefore it is also represented in Figure 1.1.

STOWA (2009)

This document was not a new norm, although it offers a discussion on changing γ_m based on the required reliability index, β. This approach was an extension of Hoffmans (2007), written for the primary dykes, in which the material factor was determined for $\beta = 4.0$. In van Hemert (2009) the material factors are provided for a range of β from $2.0 - 4.0$.

In Andringa (1989), TAW (1993) and van der Meer (1999), γ_n depends on γ_m and γ_d, and this relation was discussed in van Hemert (2009). However, because of the dependence of γ_n on γ_m, an iteration would be required to obtain a new value of γ_n after γ_m has been calculated. If this is not done, it would lead to a less conservative estimate in the case of $\gamma_m < 1.2$.

In Hoffmans (2007) the damage factor was determined according to the relationship

$$\gamma_n = 1 + 0.13(\beta - 4.0) \tag{1.5}$$

As Equations (1.4) and (1.5) calculate the damage factor in different ways, both have been presented in Figure 1.1 as IPO Equation (1.4) and ENW Equation (1.5).

Using Equation (1.4) γ_n ranges from 0.86-1.12, whereas using Equation (1.5) γ_n ranges from 0.74-1.0. Both lead to a wider range of required factor of safety than the van der Meer (1999) method which has a range of γ_n of 0.8-1.0. Equation (1.5) is less conservative than Equation (1.4) and therefore leads to lower required factors of safety.

A possible further partial factor, the schematisation factor, γ_b, was described for possible inclusion in an analysis, but it was not part of the main discussion. This factor aimed to capture uncertainty in the interpretation of field data and was initially quantified as being $1.0 - 1.2$. Because this factor was at that time not decided, it has not been taken into account in this chapter; therefore, it has not been included in Figure 1.1.

1.5. AIMS AND OBJECTIVES OF THIS THESIS

In the light of the changes which have been (and continue to be) made in design guidelines, e.g. as summarised in Figure 1.1, quantifying uncertainty and the effects

of uncertainty is an important step in research. Policy allows and tries to capture the effects of uncertainty in assessing the stability of dykes.

There are a number of key knowledge gaps that have been identified in order to capture, quantify and validate the effects of variability and uncertainty in dyke stability. In the assessment guidelines reviewed in this chapter, material property uncertainty is mostly considered by utilising a single lower bound set of material properties. However, it is well known that the material properties are spatially variable and in slope stability this variability reduces the uncertainty in the calculated stability due to averaging along the failure surface. This knowledge gap is exemplified by the frequent occurrence of dykes which fail substantially assessments, but have remained standing for several centuries. Full probabilistic dyke stability analysis, while theoretically possible remains unexploited, partly due to the difficulty of quantifying inputs required, e.g. the variability and uncertainty of shear strength. In particular, there are very few studies in accurately calculating the spatial variability, and even fewer which quantify the uncertainty in the calculated variability. Field validation of calculated dyke stability is also rare, due to the expense and difficulty in undertaking full scale tests. A limited number of full scale validation tests for dykes have been performed, but in conditions that represented either carefully engineered primary dykes, or on newly constructed test embankments. In those cases, spatial variability was neither measured nor used in the back-analysis and therefore the validation of methods including spatial variability has not been done.

In this thesis it will be shown that quantifying the uncertainty of soil strength and taking account of this in assessments will lead to a better understanding of the actual strength of (regional) dykes. The main aim of this thesis is to do a full investigation of controlled dyke failure experiment, measuring variation in the subsurface and including variation in strength in the numerical analysis. This will be achieved through the following objectives:

- Collect data specifically aimed to measure the scale of fluctuation (i.e. spatial correlation) in different directions at the dyke location;
- Cause an existing embankment to fail while monitoring the failure;
- Investigate the accuracy of the determined spatial correlation;
- Investigate strategies to determine the insitu spatial variation;
- Assess the reliability of the embankment at failure, by conducting numerical analysis that accounts for the site investigation data, uncertaities and the derived spatial correlation.

1.6. OUTLINE OF THESIS

This thesis is devided into four further chapters:

Chapter 2 describes, the design of a dyke failure field test, including all technical preparations, as well as the main observations leading up to and during failure of the dyke. The field test included the monitoring of pore water pressures, and vertical and horizontal displacements, up to and during failure (until the sensors ceased operation). For the technical preparations, a site investigation and laboratory tests were performed, and this

information was used in deterministic analyses to investigate the point of failure using the Limit Equilibrium Method (LEM) and Finite Element Method (FEM). The numerical analyses were compared to the observed failure behaviour.

Chapter 3 starts by presenting a method to measure both vertical and horizontal spatial correlations using only vertical Cone Penetration Test (CPT) data. Then, a detailed investigation into the effectiveness of estimating spatial heterogeneity, i.e. correlation lengths, using synthetic data is presented. The investigation demonstrates how the accuracy of the measured correlation length changes as the amount of data and spacing between data points vary. From this, an equation is suggested to estimate the accuracy when investigating spatial correlaitons using limited numbers of CPTs and field data.

In Chapter 4, the measured spatial variability is combined with the random finite element method (RFEM) to simulate the dyke failure experiment, so that the variation and uncertainty in strength properties can be accounted for. The addition of spatial variabilty makes it possible to compare deterministic analysis using a five percentile characteristic value to a five percentile failure probability of the structure.

Conclusions and recommendations are given in Chapter 5, highligting some of the benifits of measuring and including soil spatial variability (i.e. heterogeneity) in dyke assessments.

REFERENCES

Andringa, R. (1989). Leidraad voor het ontwerpen van rivierdijken - deel 2. *Technical Report L2*, Rijkswaterstaat, DWW.

Belgraver, P. (1973). Systematisch onderzoek boezemkaden. *Technical Report D4 73.03*, COW (Centrum Onderzoek Watekeringen).

Belgraver, P. (1993). Systematisch kade-onderzoek: De resultaten. *Technical Report D4 93.16*, TAW.

Bishop, A. W. (1955). The use of the slip circle in the stability analysis of slopes. *Géotechnique* **5**, No. 1, 7–17.

de Gast, T., Vardon, P. J., Jommi, C. & Hicks, M. A. (2015). The history of safety factors for dutch regional dykes. In *Proceedings of the 5th International Symposium on Geotechnical Safety and Risk, Delft (The Netherlands)*, IOS Press, pp. 364–370.

Hoffmans, G. (2007). Addendum bij het technisch rapport waterkerende grondconstructies. *Technical Report TR19a*, Rijkswaterstaat, DWW.

Marques, S. H., Gomes, A. T. & Henriques, A. A. (2011). Reliability assessment of Eurocode 7 spread foundations design methodology. In *Geo-Risk 2011: Geotechnical Risk Assessment and Management, At Atlanta, USA*, ASCE, pp. 632–639.

Orr, T. L. L. (2000). Selection of characteristic values and partial factors in geotechnical designs to Eurocode 7. *Computers and Geotechnics* **26**, No. 3-4, 263–279.

STOWA (2005). Ontwikkelingsprogramma regionale waterkeringen. *Technical report*, STOWA.

TAW (1993). Technisch rapport voor het toetsen van boezemkaden. *Technical Report TR18*, Rijkswaterstaat, DWW.

van der Meer, M. T. (1999). Richtlijn ter bepaling van het veiligheidsniveau boezemkaden. *Technical report*, IPO.

van Hemert, H. (2007). Leidraad toetsen op veiligheid regionale waterkeringen. *Technical Report ORK 2007-02*, STOWA.

van Hemert, H. (2009). Materiaalfactoren boezemkaden. *Technical Report 2009-05 ORK*, STOWA.

Veerman, C., Stive, M. & Deltacommissie (2008). Working together with water: A living land builds for its future. *Technical report*, Deltacommissie.

2

Controlled dyke failure experiment: Leendert de Boerspolder

Few full scale failure tests of dykes or embankments have been undertaken; even fewer on dykes or embankments that have been in operation for several centuries. The design, site investigation and detailed in-situ monitoring data is presented of a controlled dyke failure of a ~400 year old dyke at the Leendert de Boerspolder. The site investigation consisted of Cone Penetration Tests (CPTs) and continuous borings, and an extensive laboratory testing programme of which a part is presented in this thesis. Sensors were installed to measure the displacements and changes in pore pressure throughout the test. The failure was induced by progressively excavating a ditch (initially filled with water) at the polder side of the dyke and removing the water from the ditch. The size and location of the excavated ditch were designed using the Limit Equilibrium Method (LEM) analyses, and the displacements and pore pressures during the test have been modelled using coupled Finite Element Method (FEM). The results of the numerical analyses and results of the failure experiment have similar qualitative behaviour.

2.1. INTRODUCTION

In this chapter, a controlled dyke failure experiment is presented. This failure experiment was designed to provide detailed information on the behaviour of a real dyke, built on a peat layer, leading up to failure. It was designed to investigate the behaviour of dykes failing under a combination of their own weight and environmental loading. Over the period of a month, the dyke was saturated with water and soil was removed (excavated) in front of the toe incrementally, effectively increasing the height of the dyke until it failed. This, in combination with an extensive site investigation and laboratory testing programme, provided detailed information used to understand the dyke failure and pre-failure behaviour. Similar large-scale failure tests have been performed before (Lindenberg *et al.*, 2002; Zwanenburg *et al.*, 2012; Lehtonen *et al.*, 2015). However, these tests were mainly aimed at larger dykes (greater than 3 m in height) and in different geotechnical settings.

The major differences between this test and the other large-scale failure experiments are: (1) this dyke was a relatively small regional dyke, with in general lower stresses in the soil and a less regulated maintenance history, often done using local or waste material. Due to the lower stresses and relatively small structure, the failure mechanisms are smaller and the material behaviour leading up to failure plays a larger role; (2) the dyke was designed to fail driven by its own weight, i.e. not loaded at the crest or by the injection of water. Additionally, the spatial variability of the soil was investigated immediately adjacent to the experiment (see Chapter 3).

First, a site-investigation and laboratory study were performed. The purpose of the site investigation was twofold: (1) to collect information on the geometry, stratigraphy and strength in preparation for the failure test; (2) to measure the spatial variation of soil properties and estimate the correlation length, also known as the scale of fluctuation (SoF), under and adjacent to the dyke. Based on the information provided from the site investigation, sensors were installed to measure deformations (horizontal and vertical) and changes in water pressure during the failure experiment.

The site investigation and failure test were designed and implemented by the author and university collaborators, the site investigation was performed by Wiertsema & Partners, the laboratory testing by Gemeentewerken Rotterdam and colleagues at the university, the sensors were installed by Inpijn-Blokpoel and Strukton and the management of the site activities during the failure test was a collaboration with Deltares.

The location of the failure test (Figure 2.1(a)) is a small polder called Leendert de Boerspolder, in South Holland. Because it was required to be flooded in 2015, the opportunity arose to use this site as the failure test location. It is located south of one of the more economically important polders of the Netherlands, the Haarlemmermeerpolder, where Schiphol airport is situated. Leendert de Boerspolder has been on maps since 1611 (Balthasar, 1611), as indicated in Figure 2.1(b), which covers the area indicated on Figure 2.1(a) by the red box. It can be seen that a polder structure is present near the mill drawn in the south east of the map under the Hanepoel, indicated by the black box. While building the Ringvaart and correspoding dyke ring of the Haarlemmermeerpolder (the body of water north of Leendert de Boerspolder in Figure 2.1(b) in around 1840, the polder obtained its current shape. Leendert de Boerspolder was last flooded in the second world war (Andriessen, 2015), most likely due to the cessation of pumping due to fuel

shortages. Figure 2.1(c) shows an aerial photograph of the dyke in normal operation and Figure 2.1(d) immediately prior to the test.

It was decided by the Rijnland waterboard to flood Leendert de Boerspolder in 2015, to comply with the European Water Framework Directive (WFD) which stipulates that when water storage capacity is removed (in this case, by extension and maintenance works of flood defence structures at other locations), water storage capacity has to be added elsewhere.

The following aspects are presented in this chapter: (1) the site investigation and laboratory results, along with their interpretation to calculate material model parameters; (2) the design of the field test; (3) the results of numerical analyses undertaken to design the test and predict the failure, using the Limit Equilibrium method (LEM) and Finite Element method (FEM); and (4) measurements during the test.

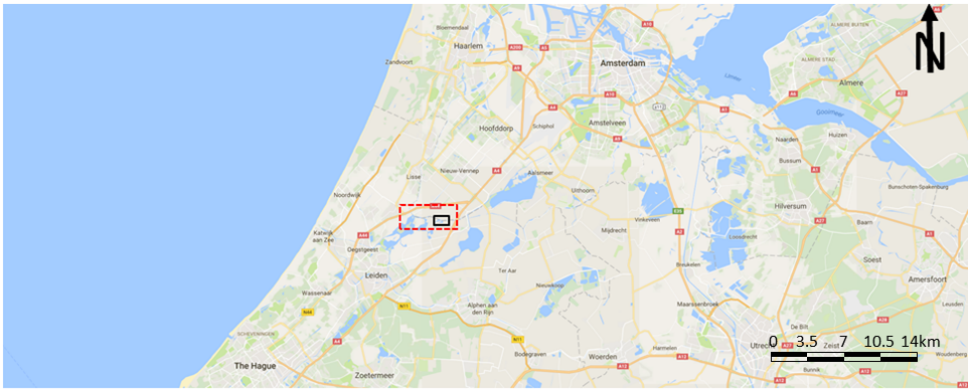

(a)

(b)

(c)

(d)

Figure 2.1: Maps and location of Leendert de boerspolder; (a) map indicating the location of Leendert de Boerspolder relative to Amsterdam, The Hague and Utrecht (after Google maps, 2017); (b) historical map where the southern shape of Leendert de Boerspolder can be recognised, dating from 1611 (Balthasar, 1611); (c) aerial photograph of Leendert de Boerspolder in normal operation (after Google maps, 2003); (d) aerial photograph of Leendert de Boerspolder with preparations for failure experiment in place (after Google maps, 2015).

2.2. SITE CONDITIONS

Figure 2.1(c) shows an aerial photograph of Leendert de Boerspolder before the preparations of the failure test had started. Figure 2.1(d) shows a triangular area in the south of the polder, where the test was undertaken after the preparations had been completed. This triangle was created by a dyke placed on the edges of ditches already present in the polder, so that the original hydraulic boundary conditions were maintained during the experiment and the rest of the polder could be flooded in a more controlled manner prior to the test.

In Figure 2.2 three locations can be seen: (A) the location where the office and data logging facilities where located, (B) the failure location and (C) the location of the heterogeneity study. In the preparation for the final flooding, the polder at locations A and C was deepened for the ecological design, whereas the polder depth at location B remained untouched.

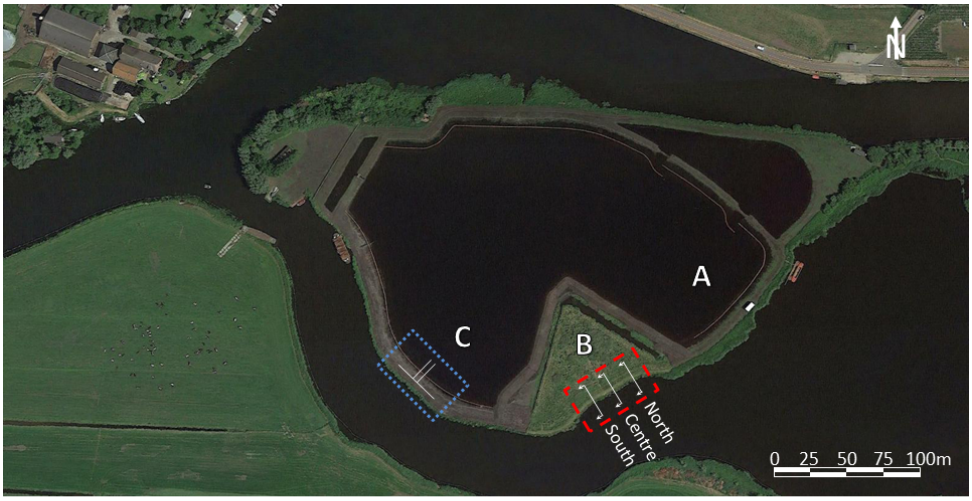

Figure 2.2: Aerial photograph of Leendert de Boerspolder with preparations for failure experiment in place, taken in 2015: (A) location of the site office, data logging and coffee making facility, (B) location of the failure (original ditches and hydraulic conditions preserved), (C) heterogeneity location (partly submerged).

Figure 2.3 shows a representative cross-section for Leendert de Boerspolder. This is for the failure location (B), although the geometry is similar to the geometry of the embankment found at location C. The crest of the embankment was NAP -0.4 m (where NAP is the national reference level) and the depth of the polder varied between NAP -1.9 m and NAP -2.1 m. The body of water south of the polder (the Hanepoel) has a fixed level of NAP -0.6 m, and over the course of the year this level varies ± 0.05 m. In the polder, the water level in the ditches was maintained at NAP -2.45 m .

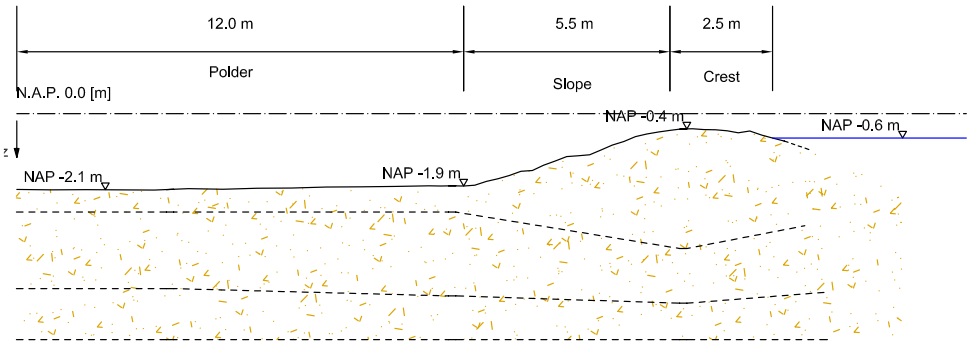

Figure 2.3: Geometry of Leendert de Boerspolder (Section B-Centre).

2.3. SITE INVESTIGATION

This section summarises the site investigation at the location of the failure test (location B), whereas the heterogeneity study, comprising 6 borings and 100 CPTu's, undertaken at location C (blue dotted box in Figure 2.2), is presented in Chapter 3. The 100 CPTs were obtained over a two week period by two different CPT-cones (calibrated before testing), CPT-rig and CPT opperator. At location B, a series of Cone Penetration Tests (CPT), with water pressure measured behind the tip (u_2), and one Ball Cone Penetration Test were performed between 26th and 29th August 2015. The specifications of the CPT penetrometer were according to NEN-ISO 22476-1 (Class 1). Three rows of 6 CPTu's, perpendicular to the dyke crest at 20 m intervals, were performed as shown in Figure 2.4. In each row, from the polder to the crest, the distance between each CPTu was 2.5 m, except for the 6th CPTu, which was located in the water and undertaken from a pontoon, 10 m away from the crest. In the centre row of measurements, one measurement was a Ball CPT. Equidistant between the rows of CPTu's, two rows of three borings were taken (Figure 2.4), using a 100 mm diameter piston sampler, providing semi-continuous samples (in 70 cm sections). Figure 2.5 shows the site investigation in progress, and a view of the polder and dyke.

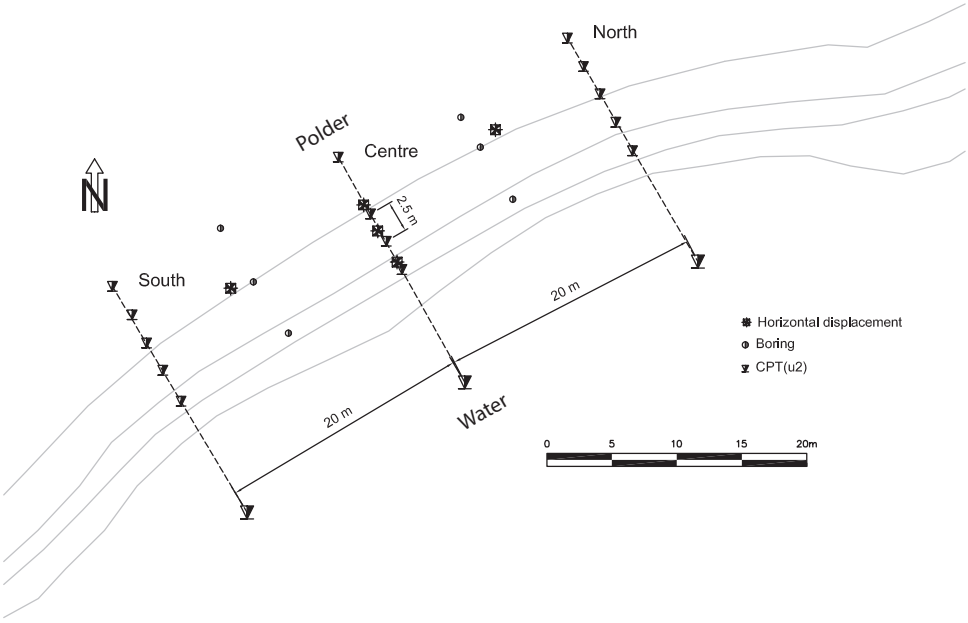

Figure 2.4: Plan view of the site investigation (red box in Figure 2.2): three lines, each with 5 closely spaced CPTs on land and one CPT in the water; two lines of 3 semi-continuous borings in the crest, slope and polder. From left to right, these lines are South, Centre and North, corresponding to Figure 2.2.

Figure 2.5: Site investigation at location B. Hand borings and installation of standpipes on the crest of the dyke. CPT investigation in progress on the slope and boring/sampling in the polder.

2.3.1. STRATIGRAPHY

The CPTu measurements provided three types of measurement data: (1) cone tip resistance q_t, (2) sleeve friction f_r, and (3) water pressure behind the cone u_2. These measurements, in combination with information obtained from the boring, were used to identify different material layers. The following four major layers were identified, starting from the surface:

1. Dyke material: this had been placed over time, since ~1600AD, to form the embankment and has been added to periodically for maintenance purposes. The materials used for construction and maintenance range from clay, silt, sand and rubble.

2. Peat: this layer has been affected by the overlying dyke material and, in the polder, by constant dewatering.

3. Organic clay: the layer starts with a high organic fraction at the top and, as the depth increases, the organic content decreases.

4. Silty clay: as the organic content decreases, the silt fraction increases and the clay layer continues until ~NAP -16.0 m depth, beyond which sand is found.

Figure 2.6 shows a cross-section through the layers, obtained from the interpretation of the different rows of CPTu. From the three cross-sections a representative geometry has been chosen by engineering judgement for the numerical analyses, indicated by the red line in Figure 2.6. This ordering of layers, as well as similar layer geometries and materials, was also found at section C.

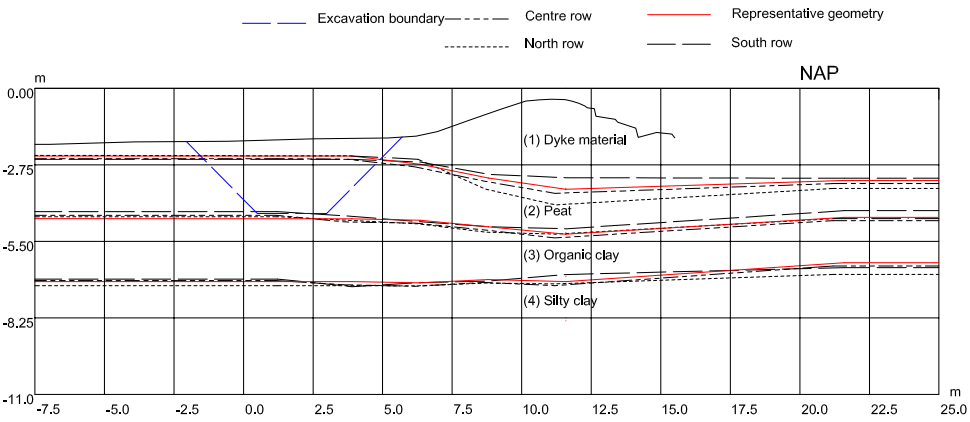

Figure 2.6: Stratigraphy interpretation from the three rows of CPTs.

2.4. LABORATORY DATA

An extensive laboratory test programme was undertaken using samples collected from the semi-continuous borehole sampling at Locations B and C. Isotopically Consolidated Undrained Triaxial tests ($TxCU$), constant rate of strain tests (CRS), K_0 constant rate of strain tests (K_0CRS), Direct Simple Shear (DSS) tests and oedometer tests have been performed. Details of the sample locations are summarised in Figures 2.7 and 2.8. The tests were interpreted and summarised in terms of values for a Mohr-Coulomb (linear-elastic, perfectly-plastic) constitutive model for each material. For the failure surface, the c', ϕ' parameters have been determined at 5% axial strain, derived by drawing a best fit line by eye through the points. The strain level was chosen at a single value to ensure kinematic consistency; the dyke material is close to critical state and has shown hardening behaviour, the peat is in pre-peak strength conditions due to extensive hardening behaviour typically associated with peat, and the organic clay is almost at peak strength after which softening is observed. The stiffness properties were chosen by experience, as the laboratory investigation focused on the shear strength behaviour (and the stiffness is known to have asecond order effect on the slope stability). The interpreted parameters are given in Table 2.1 and the test data, with the 5% points used for interpretation, are shown in Figure 2.9.

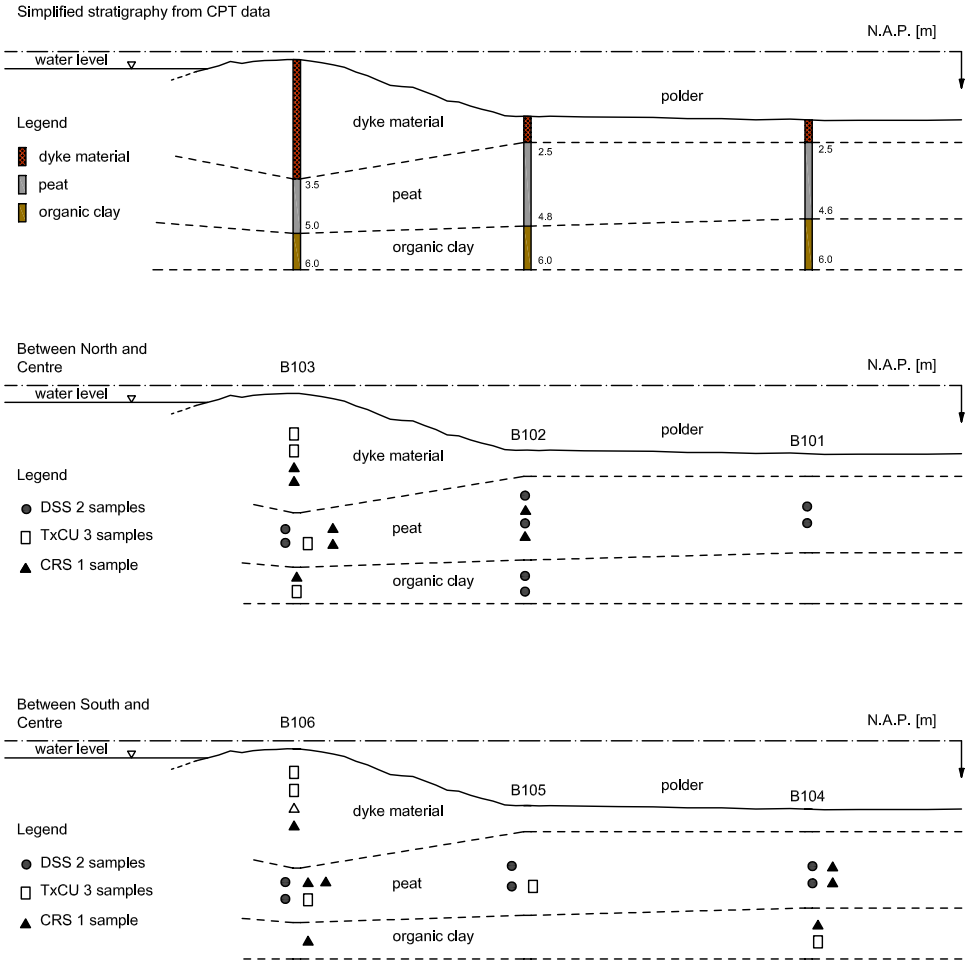

Figure 2.7: Laboratory test plan for Location B (red box in Figure 2.2), cut-off at a depth of NAP -6.0 m. The stratigraphy is indicative.

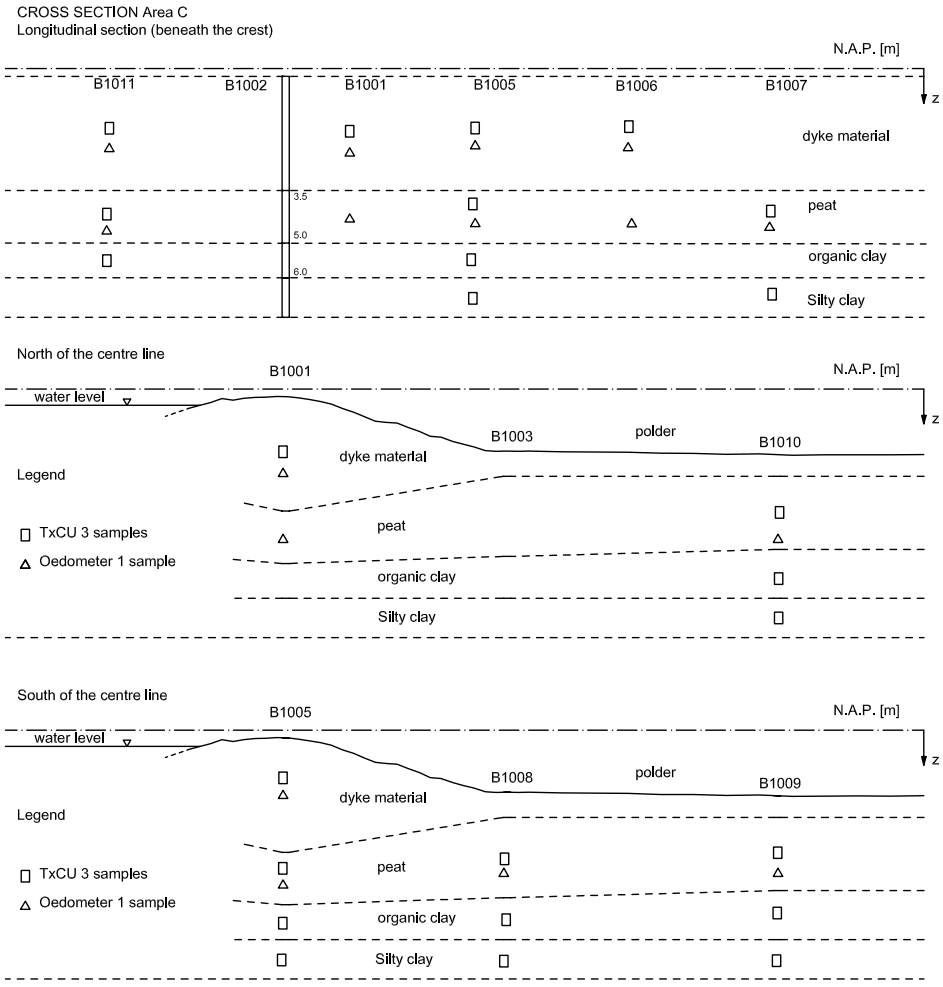

Figure 2.8: Laboratory test plan for Location C (blue box in Figure 2.2).

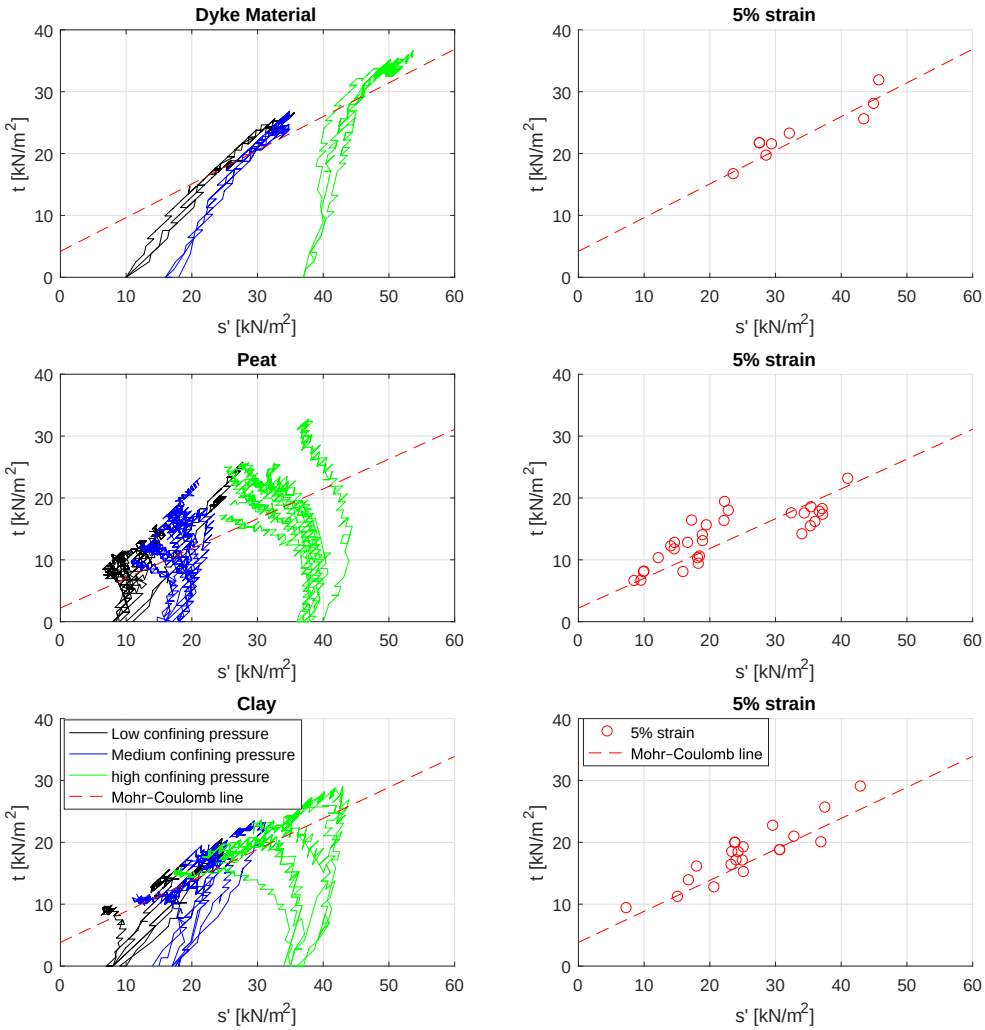

Figure 2.9: Consolidated undrained triaxial data (effective stress paths and stress states at 5% axial strain)

Table 2.1: Soil parameters derived from triaxial laboratory data at 5% axial strain

	$\gamma_{dry}/\gamma_{sat}$ [kN/m^3]	c' [kN/m^2]	ϕ' [°]	E' [kN/m^2]	ν' [-]	$k_{x,y}$ [m/day]
Dyke material	13.0/18.0	5.0	33.0	5600	0.3	3.46×10^{-1}
Peat	9.0/10.0	2.5	28.8	1700	0.3	4.00×10^{-2}
Organic clay	14.5/15.0	4.4	29.5	5200	0.35	7.52×10^{-4}
Silty clay	14.0/17.0	1.9	30.0	5300	0.35	7.52×10^{-4}

γ_{dry}	dry unit weight
γ_{sat}	saturated unit weight
c'	effective cohesion
ϕ'	effective friction angle
E'	effective Young's modulus
ν'	effective Poisson's ratio
$k_{x,y}$	hydraulic conductivity

2.5. FAILURE EXPERIMENT DESIGN

The experiment was designed so that a failure would occur through the peat layer, as this was expected to be the weakest layer and therefore of most interest for real dyke assessment. The embankment was loaded/modified in seven stages, so that the pre-failure behaviour could be monitored and so that the stress/strain conditions of the failure could be more easily back-calculated. For the design of these stages, numerical modelling was used to estimate the deformations and stability of the embankment during the experiment. The numerical analyses are presented in Section 2.8. The stages are summarised in Figure 2.10 and Table 2.2.

Table 2.2: Main steps in failure test

Date	Time (UTC) [$hh:mm$]	Stage	Action
18-09-2015	00:00	I	Start data acquisition
21-09-2015	13:15	I	Start of wetting system
28-09-2015	07:20	II	Start first excavation
30-09-2015	07:30	III	Start pumping
01-10-2015	07:30	III	Stop pumping and start refilling
05-10-2015	06:10	IV	Start second excavation
07-10-2015	07:30	V	Start pumping
08-10-2015	06:00	V	Stop pumping ahead of schedule; start refilling
12-10-2015	09:52	VI	Start third excavation
13-10-2015	22:42	VII	Start pumping
14-10-2015	04:26	VII	Failure

In the first stage, the crest of the embankment was wetted via a wetting system (Figure 2.11). The wetting system was made from PVC tubes with holes drilled at 15 cm spacing, connected to a water reservoir providing a continuous flow of water throughout the test.

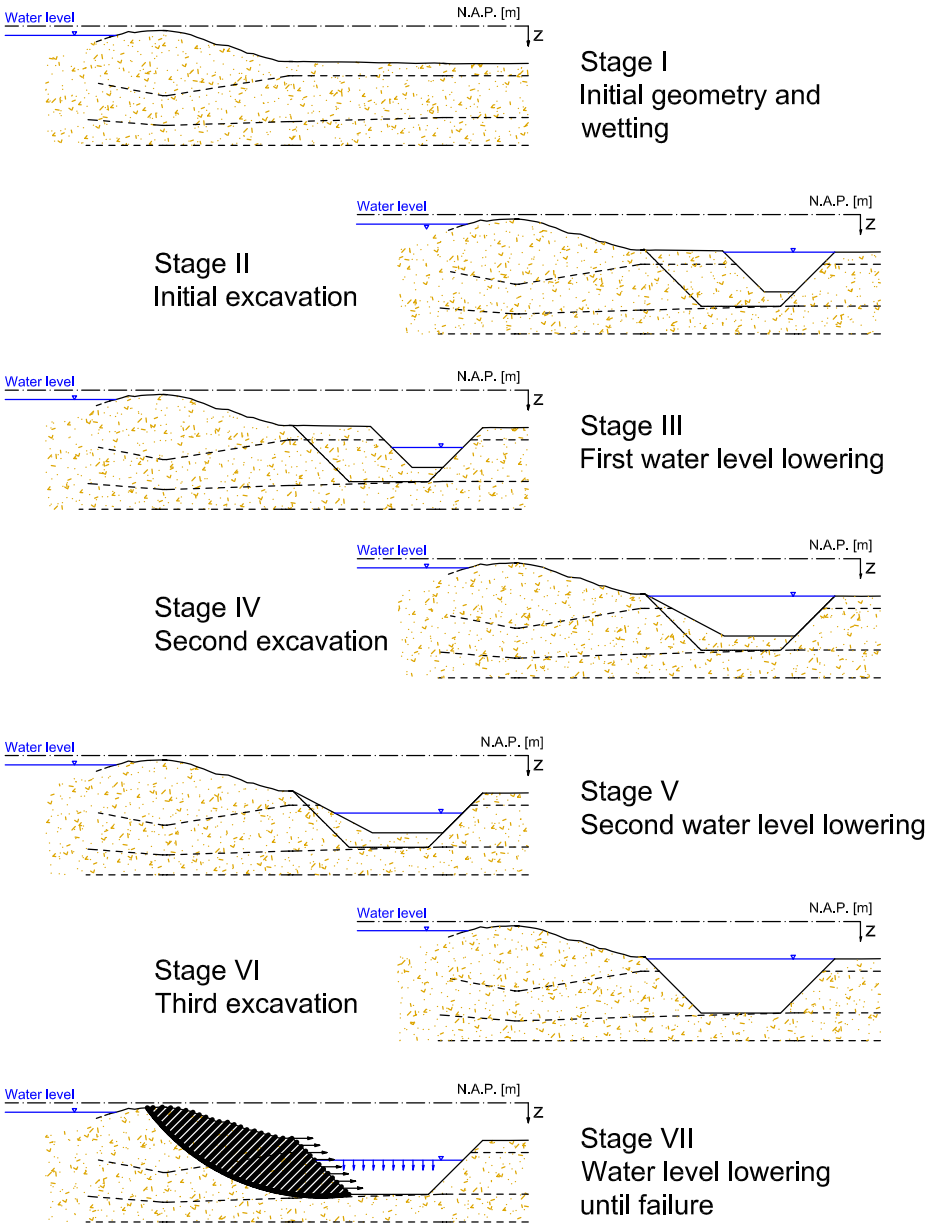

Figure 2.10: Stages in the failure test, (Stage I), initial geometry with artificial rain from the crest, (Stage II), initial excavation with the excavation filled with water, (Stage III), water level lowered by 1.0 m, (Stage IV), second excavation with a 2:1 (h:v) slope from the toe of the dyke and widening of the bottom of the ditch and filled with water, (Stage V), water level lowered by 1.0 m, (Stage VI), third excavation 1:1 slope from the toe of the dyke and deepening of the ditch by 0.5 m, (Stage VII), lowering of the water until failure.

Figure 2.11: Dyke wetting system.

The water was applied relatively slowly to avoid any erosion; this allowed the embankment to become saturated in (equilibrate pore pressures) the course of a week, to reduce uncertainties related to unsaturated behaviour. In Stage II, a relatively small ditch was excavated parallel to the dyke, with a width of 5.5 m perpendicular to the dyke at the top of the excavation, 1:1 side slopes and a depth of 2.0 m. The ditch was filled with water during the excavation, compensating (partially) for the mass loss of the excavated material and to prevent early uncontrolled failure. After excavating the ditch, there was no activity for one day in order to reach hydraulic equilibrium. In Stage III, the water level in the ditch was lowered by 1.0 m for one day and then raised again. After another three days Stage IV was implemented, where the ditch was further excavated underwater to a total width of 9.0 m, with slopes of 2:1 (h:v) near the embankment and 1:1 at the far side of the excavation from the embankment, maintaining the depth of 2.0 m. Again, after waiting for a day to reach equilibrium, the water was lowered by 1 m in Stage V. However, one

and a half hours before the end of the intended 24 hour period, a sudden displacement occurred and it was decided to raise the water level again, preventing a collapse of the dyke. After another three day waiting period Stage VI was implemented, where the slopes of the ditch were steepened to 1:1 and deepened to the bottom of the peat layer at 2.5 m depth. In the last stage, Stage VII, the water was lowered until the failure occurred.

2.6. MONITORING SYSTEM DESIGN

To track the failure of the dyke and capture its behaviour before and during failure, a series of sensors were installed. All sensors were connected to the same data acquisition system that recorded all data at Coordinated Universal Time (UTC). The locations of these sensors are shown in Figures 2.12 and 2.13. Two rows of pore pressure sensors (Geo Point type 21 Y, pushed in place with elongated tubing), each with 7 sensors in individual pockets, were installed at the North and South rows (note that these are slightly different rows than for the CPTs, see Figure 2.12), and one row of pore pressure sensors with 8 sensors in the Centre row was installed. These sensors were concentrated in the peat layer because most of the pore pressure differences were expected there, with additional sensors placed in the dyke material above the peat and organic clay below the peat. At the toe of the dyke, in the north and south rows, the horizontal displacements were measured using inclinometers (Shape Accel Array field measurand model 003) and extensiometers (Sol Experts, modular extensometer) were used to measure the vertical displacements.

The inclinometers were placed in plastic tubing and founded in the sand layer, with the tops of the inclinometers being at the ground surface. If the inclinometer was not able to reach the sand layer, it was elongated by a steel element at the bottom of the inclinometer. The inclinometer (Shape accel arrays) was made from stiff elements of 50 cm length and between each element the rotations were measured. From this, the horizontal displacements can be calculated from bottom to top assuming a fixed base. The extensiometers were anchored at a certain depth, and connected via a glass fibre rod to a sensor at the surface measuring the heave or settlement of the connected rod and thereby the movement of the anchored point relative to the surface.

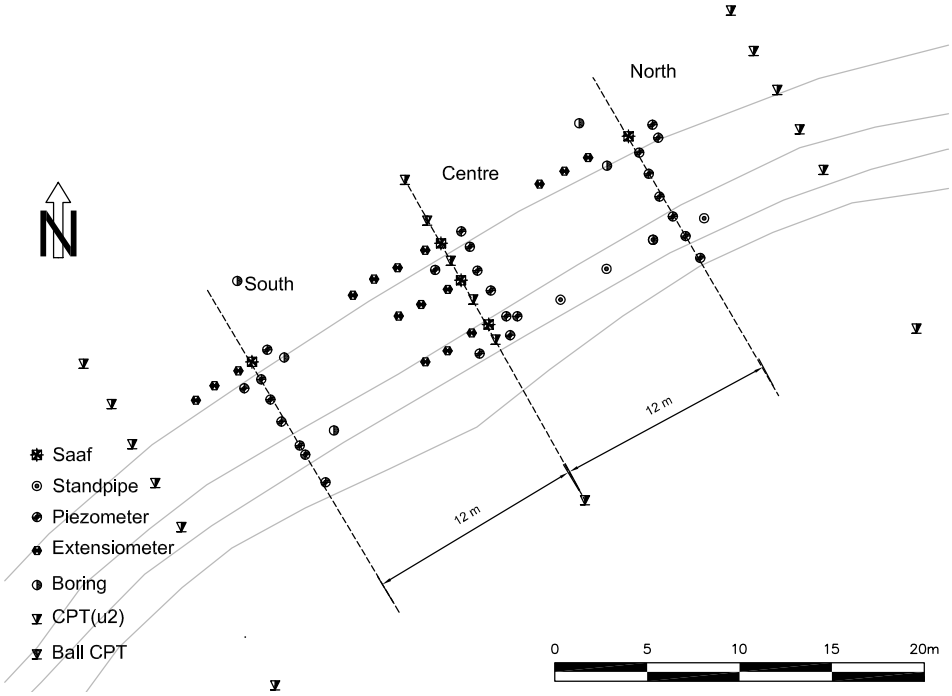

Figure 2.12: Plan of instrumentation and site investigation (red striped box in Figure 2.2): CPTs, borings, individual extensiometers, inclinometers (saaf), piezometers and standpipes.

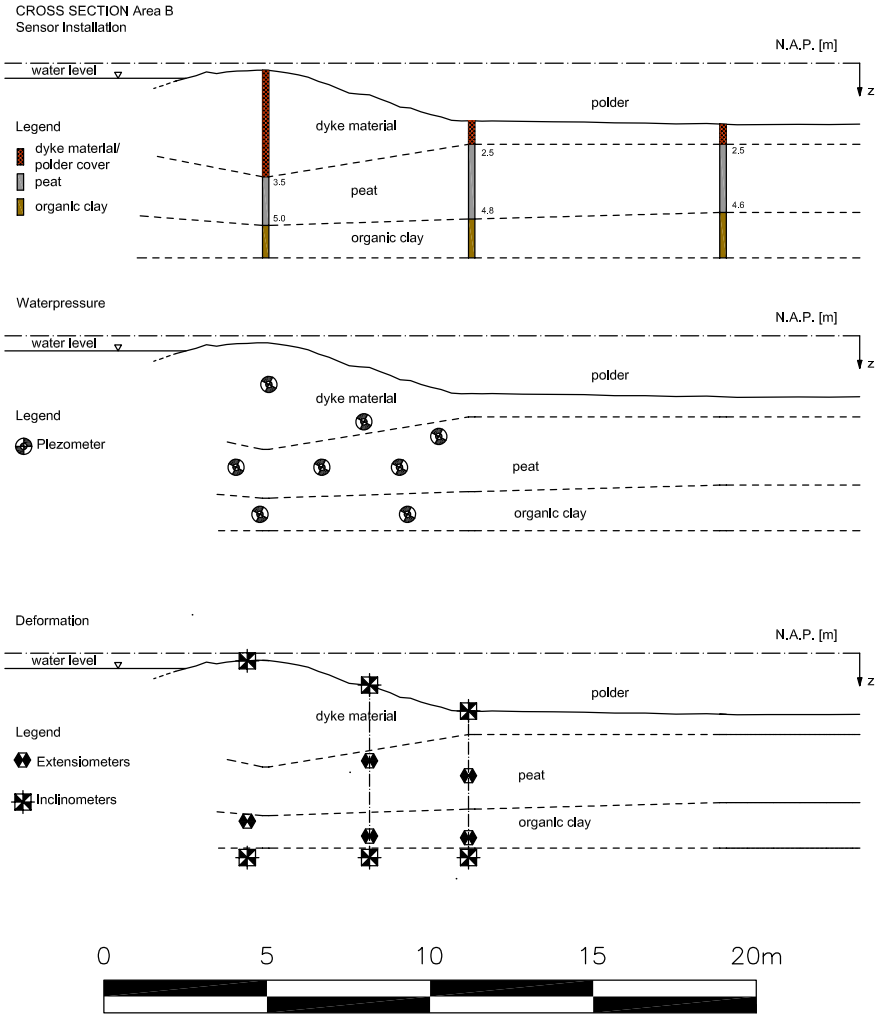

Figure 2.13: Stratigraphy of Leendert de Boerspolder and cross-sectional view of sensor placement.

2.7. OBSERVATIONS

The progression of the test has been evaluated using the extensiometers, inclinometers and pore pressure sensors in the following section. Table 2.2 and Figure 2.10 give a summary of the stages and when the actions in each stage were performed.

2.7.1. STAGE I - WETTING

Figure 2.14 presents three cross-sections, each showing the difference in pore pressures, total displacements (vertical and horizontal displacements combined from the inclinometer and extensiometer data) and horizontal displacement differentials (the difference between two consecutive inclinometer points) over a selected time window. The locations of the pore pressure sensors and extensiometers are indicated, and the locations of the inclinometers coincide with the lines of the extensiometers. The measured vertical displacements were evenly distributed over the domain.

In Figure 2.14, it can be seen that during the wetting phase, before the excavation, the dyke body material increased in volume. This is indicated in the central crest extensiometer graph (over the time interval) and by the direction of the green arrows on the cross-sections. The dyke body moves in the upstream direction (towards the water), indicated by the green displacement arrows in the Centre graph pointing to the left. In all three cross-sections the water pressures increase substantially near the surface at the crest and at the toe. The increase in water pressures at deeper locations was limited. These results indicate the dyke body saturating with water, thereby increasing the total weight of the dyke body and consequently compacting the peat and displacing the dyke body upstream.

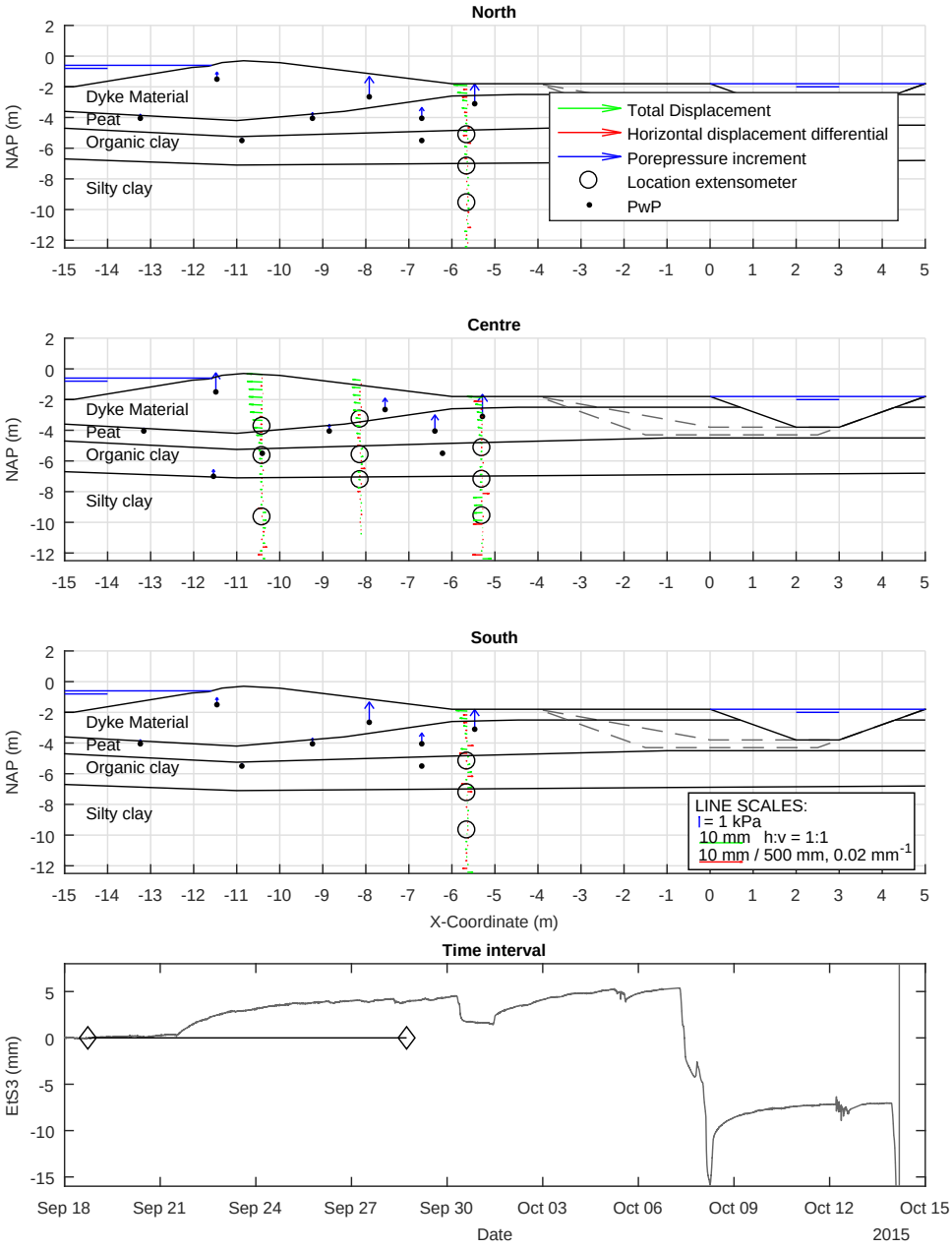

Figure 2.14: Stage I, wetting phase: Displacement vectors, and pore pressure increments at the north, centre and south sections, over the time interval of September 19 to September 29, as well as extensiometer EtS3 over the whole time period with the time period of the subfigures highlighted.

2.7.2. STAGE II - FIRST EXCAVATION

During the underwater excavation of the ditch, changes in the measured displacements and measured pore pressures were limited. This was attributed to directly replacing the excavated volume with water. As most of the excavated material was peat, the changes in total stresses in the system were minimal.

2.7.3. STAGE III - FIRST PUMPING AND REFILLING

In this stage, the water in the ditch was lowered by one metre. In Figure 2.15 the data over the pumping period are shown and in Figure 2.16, adding two hours to the time interval, the end of the stage is shown, i.e. including refilling. In Figure 2.15, in the plot of the displacements against the time interval, a sudden vertical displacement (downwards) can be seen after drawdown. Inspecting the pore pressures in the north row, a decrease in water pressure is shown mainly in the toe (seen in the peat and organic clay). The inclinometer data show that horizontal differential displacements occurred near the peat and organic clay boundary. In the centre row, the pore pressure changes occurred mostly in the toe (peat and organic clay), although changes in pore pressure can also be observed in the peat and organic clay under the dyke body. The displacements in the toe show local differential displacements in the silty clay and in the peat, and differential displacements also occur gradually over depth. The displacements in the slope are also gradually increasing over depth in the organic clay, with no sudden increase in the differential displacements indicating a volumetric change due to effective stress changes, i.e. not a shear failure. In the crest are there no displacements shown in the clay, and at mid level in the peat there is a single differential displacement, after which no big differential displacements occurred, indicating a shear displacement. In the south row, pore pressure changes occurred under the toe and only limited pore pressure changes occurred elsewhere. The displacements gradually increased over depth in the silty and organic clay layer, with larger differential displacements shown at the interface between the peat and organic clay.

After the ditch was filled again with water, displacements and water pressure differences reduced. In Figure 2.16, in the time interval plot, it is shown that the vertical displacements rebound after the ditch is refilled. Comparing the pore pressures before and after the pumping in the north row, no big changes in the water pressures are observed. The horizontal differential displacements near the peat and organic clay boundary remained, suggesting permanent deformation had occurred. In the centre row, the pore pressure differences reduced after refilling and the differential displacements beneath the toe in the silty clay and in the peat are reduced significantly. The displacements in the slope reduced and are still gradually increasing in the organic clay with no sudden increase in the differential displacements. Below the crest, the observed displacements reduced and still no displacements are shown in the clay; in the peat, where there was a sudden differential displacement observed after pumping, no reduction occurred after refilling. In the south row, the pore pressure differences reduced at the toe. The displacements were reduced. However, compared to the start of pumping still displacements were measured in the silty and organic clay layers, suggesting that permanent deformation had occurred as the displacements did not decrease to their original state.

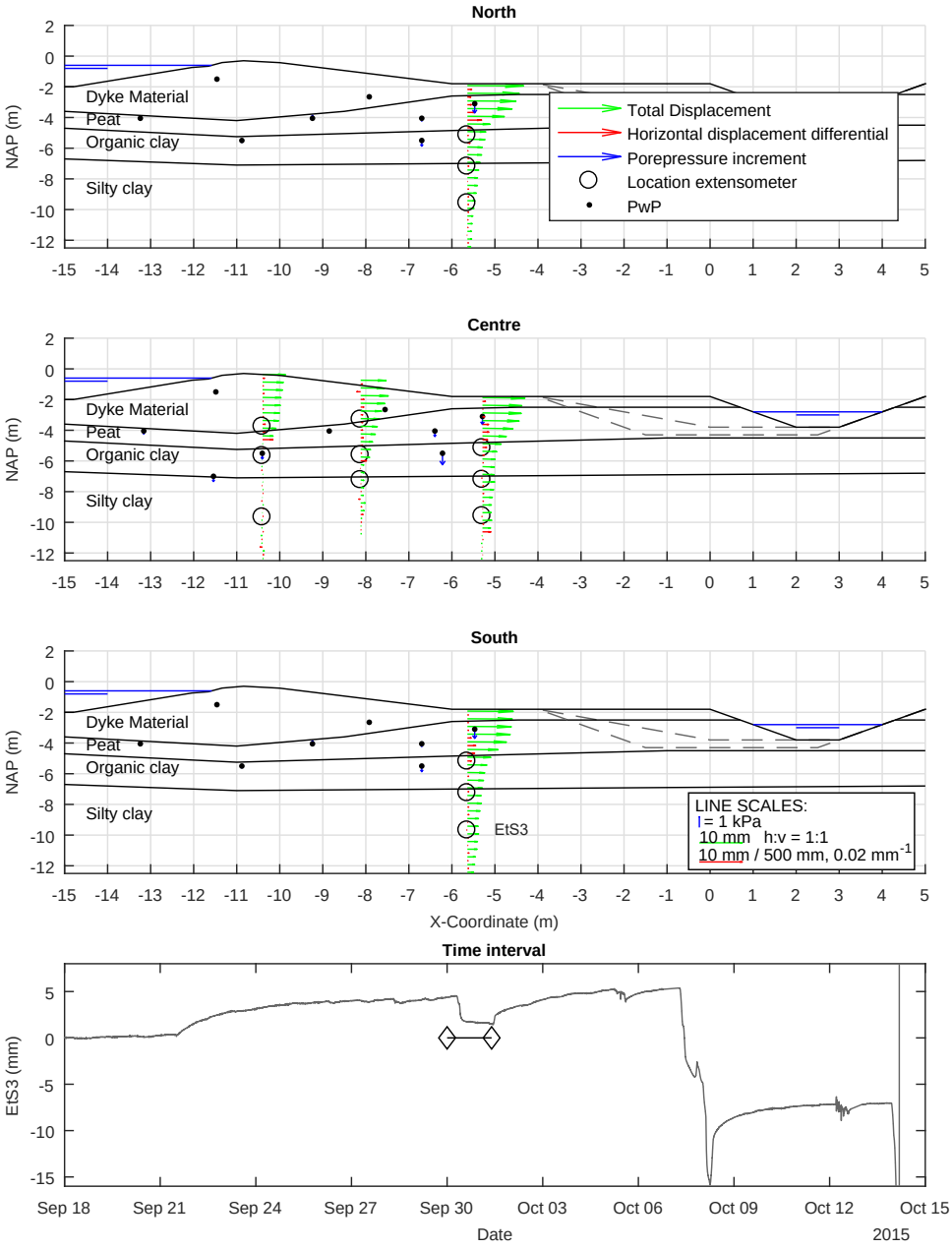

Figure 2.15: Stage III (before refilling), Displacement vectors, and pore pressure increments at the north, centre and south sections, over the time interval of September 19 to September 31, as well as extensiometer EtS3 over the whole time period with the time period of the subfigures highlighted.

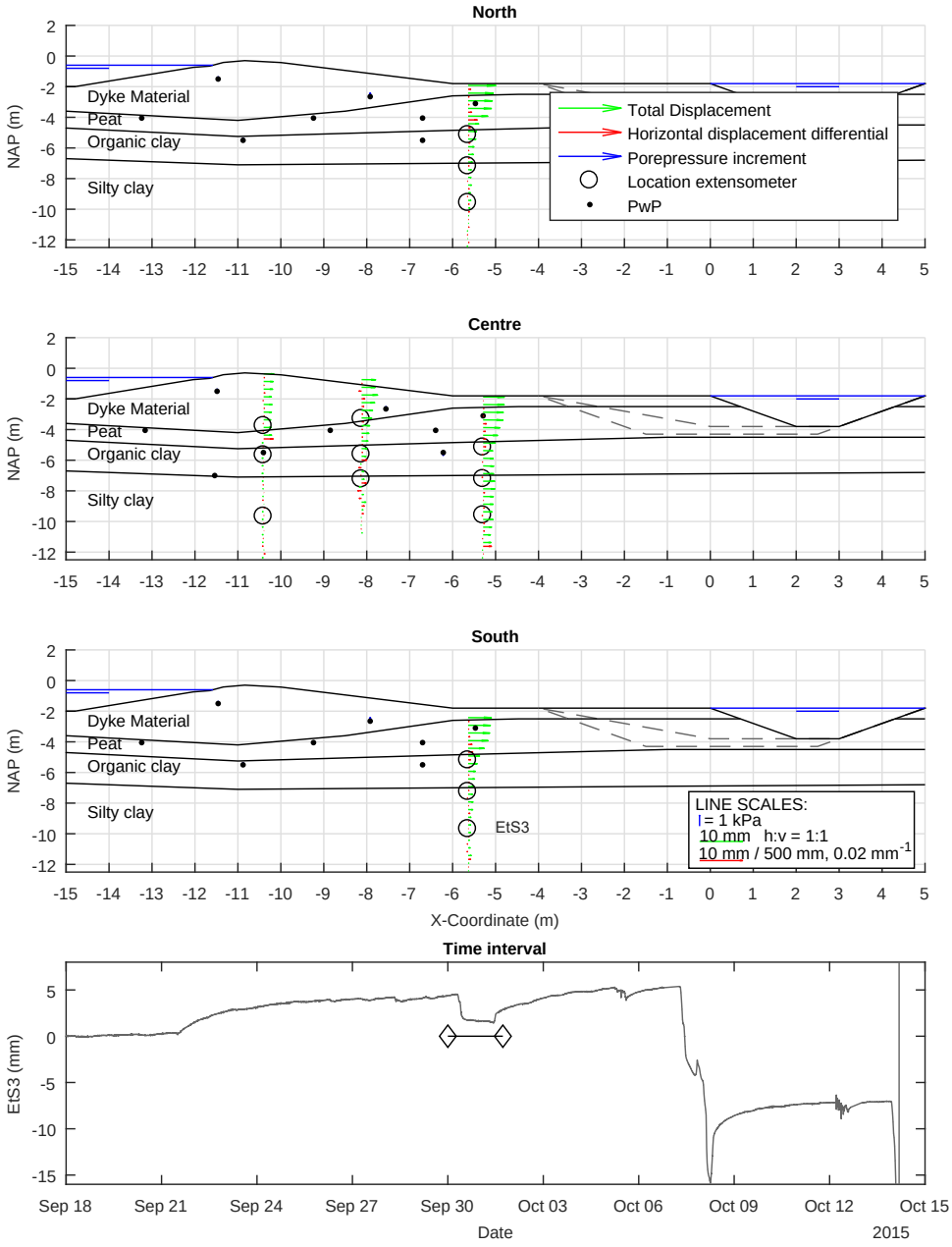

Figure 2.16: Stage III (after refilling), Displacement vectors, and pore pressure increments at the north, centre and south sections, over the time interval of September 19 to September 31, as well as extensiometer EtS3 over the whole time period with the time period of the subfigures highlighted.

2.7.4. STAGE IV - SECOND EXCAVATION

During the second excavation, measured displacements and changes in measured pore pressure did not increase significantly. This was again attributed to directly replacing the excavated volume with water, since again most of the excavated material was peat.

2.7.5. STAGE V - SECOND PUMPING AND REFILLING

After the second excavation, the water was lowered again by one meter. In Figure 2.17 the data from the second pumping period are shown and in Figure 2.18 the end of the stage is included, i.e. including refilling. In Figure 2.17, in the plot of displacements over the time interval, it can be seen that the displacements suddenly increased and, when this was discovered during the test, the water level was raised again. Beneath the toe of the north, centre and south rows, large differential displacements can be seen at the interface between the organic clay and peat layers. In the south row, the displacements are larger than those in the centre and north rows. The pore pressure differences are largest beneath the toe in the north, centre and south rows. In the centre row, the pore pressure differences under the crest and the slope are larger than for the north and south rows. In the centre row, two large displacement differentials can be observed below the slope, one at the organic clay-peat boundary and the other in the dyke material. The differential displacements below the crest are seen to gradually increase.

After the ditch was refilled (Figure 2.18), all the displacements reduced. In contrast to Stage III, the pore pressure differences in the peat remained low compared to the initial pressure.

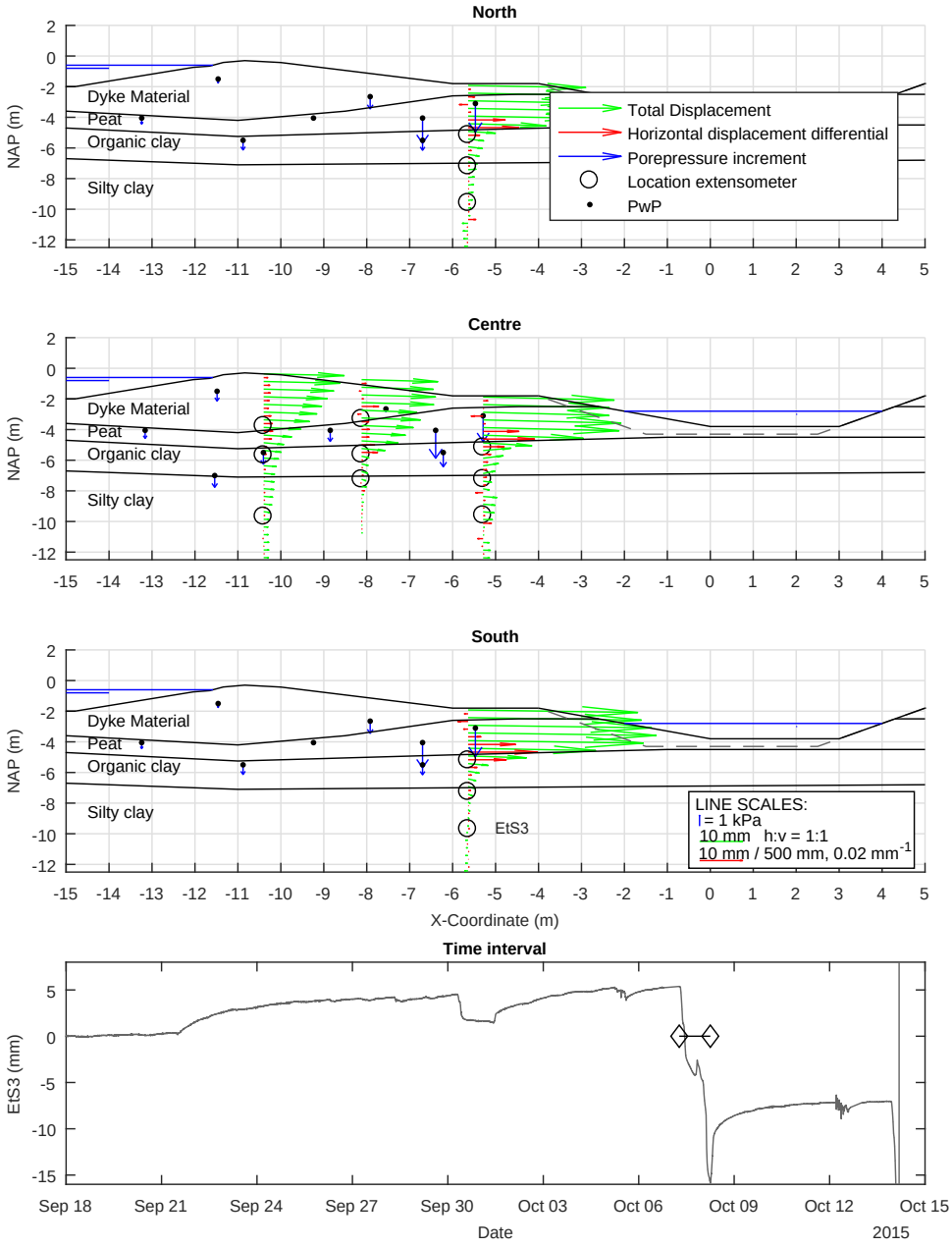

Figure 2.17: Stage V, pumping: Displacement vectors, and pore pressure increments at the north, centre and south sections, over the time interval of October 7 00:00:00 (UTC) to October 8 06:00:00 (UTC), as well as extensiometer EtS3 over the whole time period with the time period of the subfigures highlighted.

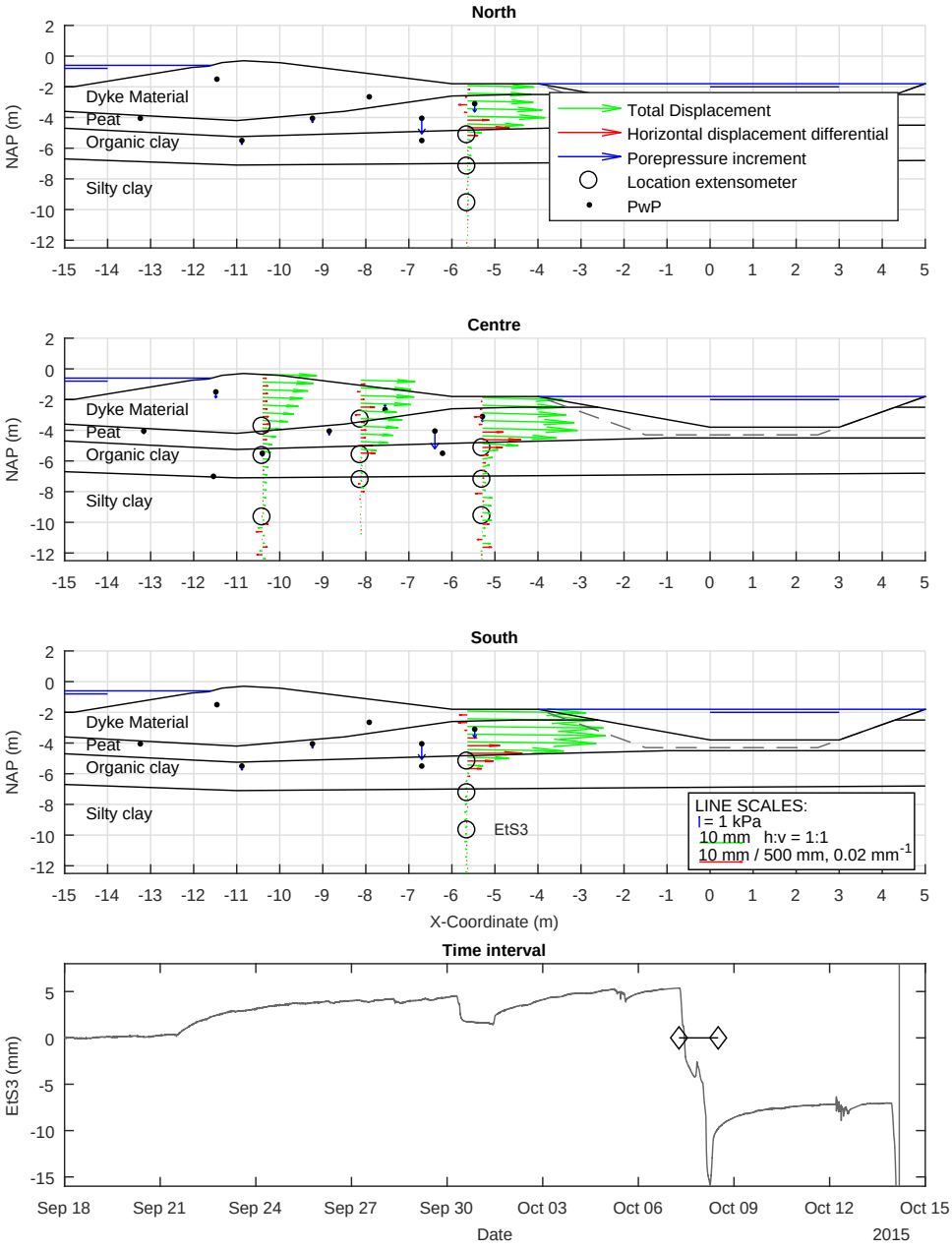

Figure 2.18: Stage V, pumping and refilling: Displacement vectors, and pore pressure increments at the north, centre and south sections, over the time interval of October 7 00:00:00 (UTC) to October 8 12:05:00, as well as extensiometer EtS3 over the whole time period with the time period of the subfigures highlighted.

2.7.6. STAGE VI - THIRD EXCAVATION

During the third excavation, the measured displacements and changes in measured pore pressure did not increase significantly.

2.7.7. STAGE VII - DYKE FAILURE

After the third excavation, the water was pumped until failure. In Figure 2.19 the data from the pumping period until failure are shown. In the north row, the pore pressures decrease in the peat, organic clay and dyke material, except in the peat under the slope. Large differential displacements in the toe of the north row were observed, located at the boundary between the organic clay and peat layer, indicating a shear band. The main failure occurred between the centre and south rows, as can be seen in Figure 2.20 by comparing the smaller displacements in the north row to the larger displacements in the centre and south rows. In the toe, large differential displacements are measured below the peat and organic clay boundary in the organic clay layer. In the centre, large differential displacements were also measured at the boundary of the organic clay layer and the peat. Differential displacements in the crest were distributed near the boundary between the peat and dyke material. In the time frame, failure occurred between a drawdown of 1.5 m and 1.75 m; the precise level of the water at failure could not be determined due to safety concerns, but is estimated at 1.6 m.

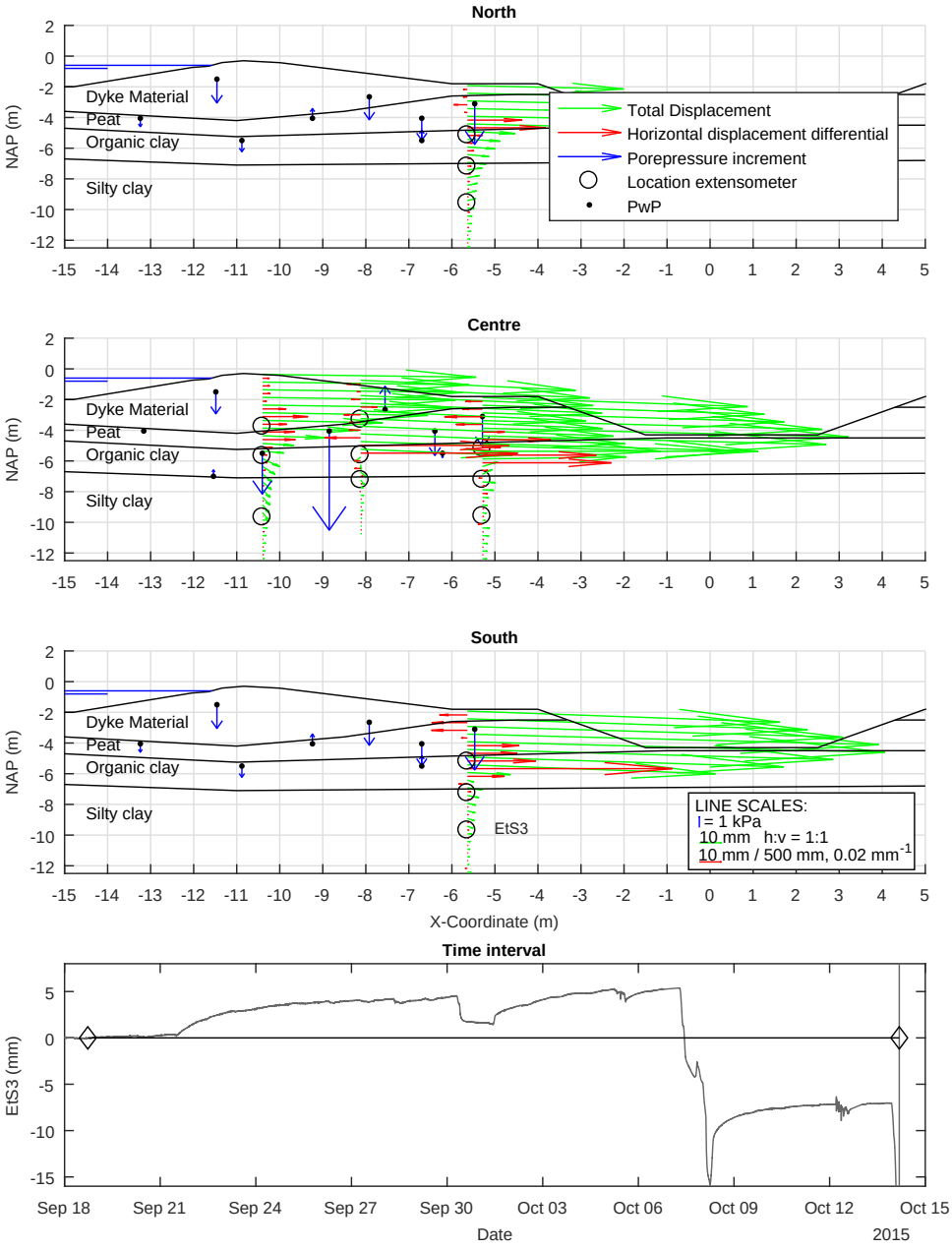

Figure 2.19: Stage VII, failure: Displacement vectors, and pore pressure increments at the north, centre and south sections, over the time interval of September 19 to October 14, as well as extensiometer EtS3 over the whole time period with the time period of the subfigures highlighted.

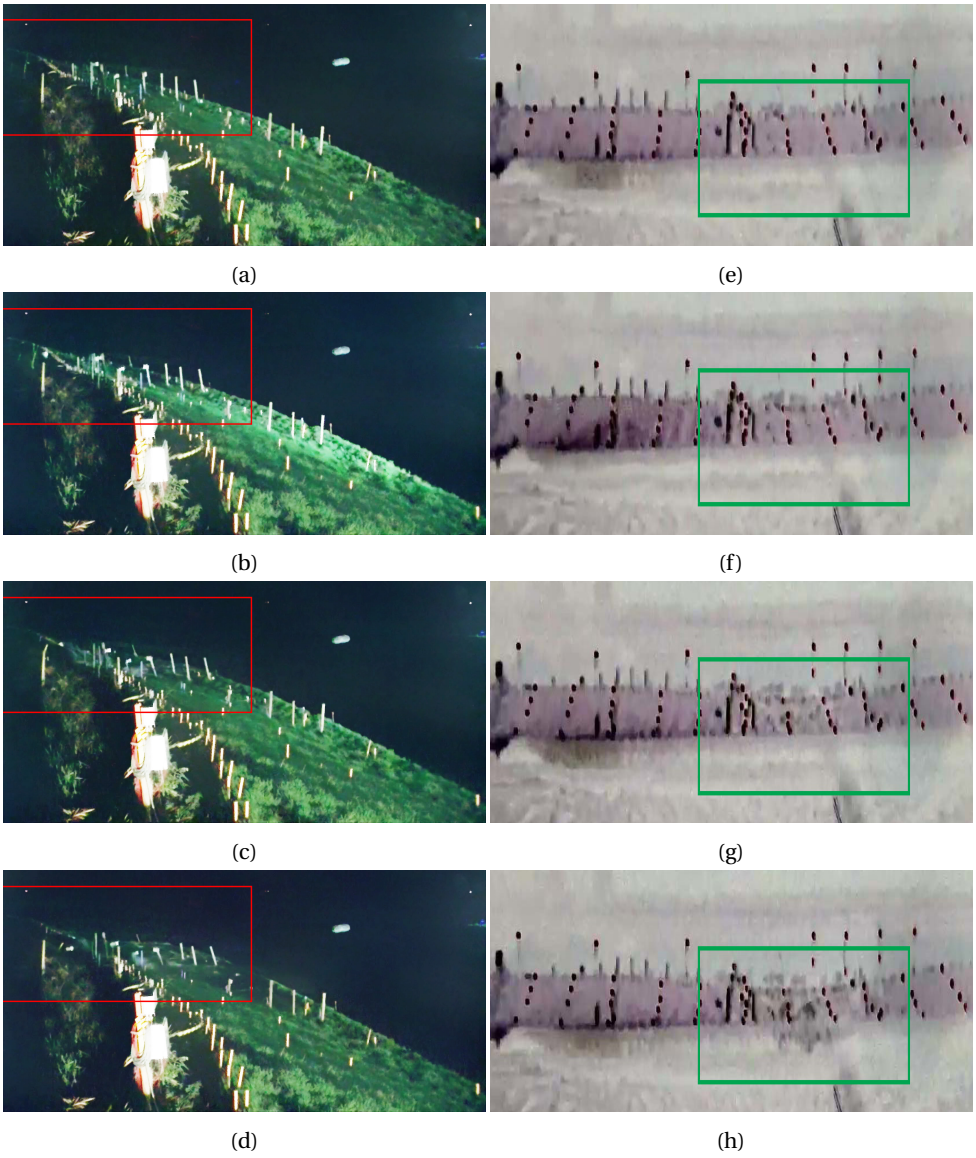

Figure 2.20: Video camera (20 seconds) stills of the failure; the left-hand side shows video stills in true colour, whereas the right-hand side shows inverted colour. The failure location is highlighted by the rectangular box; (a) and (e) show the embankment moments before failure. In (b) and (f) the first signs of failure are seen; in (b) the crest is slightly indented in the top left of the picture, whereas in (f) on the right side it can be seen that displacements occur at the top of the crest. Figures (c) and (g) show the first water coming over the top of the embankment, as well as increased deformation. In (d) and (h) water started flowing in the ditch and, after this image, the breach (observed by the flow of water increasing) starts to expand laterally.

2.8. NUMERICAL AND FIELD TEST COMPARISON

The behaviour of the experiment was predicted using two different types of analyses: (1) a Limit Equilibrium Method (LEM) stability analysis, using the program D-Geo stability (version 15.1), requiring only geometry, input of (static) hydraulic conditions, volumetric weight and shear strength of the soil layers; and (2) a Finite Element Method (FEM) coupled hydro-mechanical analysis, using the program PLAXIS (version 2015), requiring, parameters for a linear elastic, perfectly plastic (Mohr-Coulomb) material model and permeability parameters.

The main advantages of the LEM type calculations are the speed of calculation, and the few material properties required. Therefore, the LEM program was used to calculate different alternatives for the experiment and obtain approximate factors of safety. However, only the analyses relating to the chosen experimental design are presented herein.

For each excavation step, the factor of safety was calculated using LEM. The calculated factors of safety obtained from the LEM calculations have been corrected for 3D effects using a comparison between the 2D FEM calculation and the 3D FEM calculation, from which a site-specific ratio to correct the 2D LEM analysis results was obtained.

More detailed calculations, including hydro-mechanical coupling, were done with FEM. They required more calculation time. The FEM analyses calculated the (changing) hydro-mechanical conditions in time, requiring only (hydraulic) boundary conditions and a converged mesh to do the analysis. In the 2D analysis, the excavation and dewatering steps were introduced, resulting in calculated displacements and changes in pore water pressures that were used to determine the placement of the sensors. In a 3D analysis, the layer boundaries identified at different CPTu locations were entered and interpolated linearly between the locations. This was done to investigate the effect of changes in geometry on the location and size (3D extent) of the expected failure.

2.8.1. LEM ANALYSES

The geometry of the analysis is presented in Figure 2.21. The layers were obtained from the site investigation and estimated based on the three rows of CPTs at this location, see Figure 2.6. The water level in the Hanepoel was fixed at NAP -0.6 m, and the water level in the ditch was changed based on the proposed drawdown in the ditch. Inside the dyke the pore water pressures were adjusted (by hand) to the measured pore pressures of the previous phase (when available) and interpolated linearly between the measured points.

In the LEM program, there are different options to add material properties, and here two approaches were used: (1) Mohr-Coulomb (c', ϕ') parameters were used for drained analyses and these were obtained from laboratory tests, see Section 2.4; (2) undrained shear strength, s_u, was used for undrained analyses and the parameters have been determined from CPT tests using the N_{kt} correlation (Robertson, 2009):

$$s_u = \frac{q_t - \sigma_v}{N_{kt}} \tag{2.1}$$

where q_t is the total cone resistance (kPa), σ_v is the total vertical stress (kPa) and N_{kt} is an empirical correction factor (−). Values for N_{kt} suggested by Robertson (2009) range from 10−20. Figure 2.22 shows the shear strength estimates. The laboratory data (20

Table 2.3: Material properties as used in the LEM analyses

	$\gamma_{dry}/\gamma_{sat}$ [kN/m^3]	c' [kN/m^2]	ϕ' [°]	s_u average* [kN/m^2]
Dyke material	13.0/18.0	5.0	33.0	26.0-10.0
Peat	9.0/10.0	2.5	28.8	13.5-11.5
Organic clay	14.5/15.0	4.4	29.5	13.0-10.0
Silty clay	14.0/17.0	1.9	30.0	20.0-20.0
	γ_d/γ_{sat} [kN/m^3]	s_u crest* [kN/m^2]	s_u slope* [°]	s_u polder* [kN/m^2]
Dyke material	13.0/18.0	35.0-17.0	22.0-17.0	11.0-17.0
Peat	9.0/10.0	13.0-10.5	9.0-13.0	6.0-7.5
Organic clay	14.5/15.0	12.5-11.0	13.0-18.0	5.0-11.0
Silty clay	14.0/17.0	20.0-20.0	20.0-20.0	20.0-20.0

*s_u is presented with two values, top and bottom of the layer a linear interpolation of the strength is assumed

consolidated undrained triaxial tests and four direct simple shear tests) were used to determine the maximum undrained shear strength s_u against depth. Then the N_{kt} values (per layer) were calculated, so that the s_u determined from the CPT data best fitted the laboratory data (see Figure 2.22). The values of N_{kt} for the four materials were determined to be : (1) dyke material, $N_{kt} = 20$; (2) peat, $N_{kt} = 15$; (3) organic clay, $N_{kt} = 10$; and (4) silty clay, $N_{kt} = 10$. The material parameters found for the different layers are given in Table 2.3.

Two different levels of detail were used in defining the undrained material properties: (1) 1 zone per layer, so that only the material boundaries are identified 2.21(a), (2) 3 zones per layer, with the cross-section being divided into three zones due to different loading history 2.21(b). The choice of the boundaries between the different zones was aided by the calculated stress distribution in FEM; the zones are (a) under the crest (b) under the slope and (c) in the polder, as shown in Figure 2.21(b). Figure 2.22(a) shows the shear strength estimation, with an estimate of the range using an $s_u \pm \sigma$ average moving 0.25 m window. Figure 2.22(b) shows a comparison of the shear strength τ based on c' and ϕ', τ based on s_u in a 0.25 m window, and τ based on s_u on the linear approximation over the layer.

Different slip surface assumptions were considered: circular (Bishop), two half circles connected by a horizontal line (Uplift Van) and linear segments connected at different angles (Spencer). Table 2.4 shows the results of the different simulations for the initial situation (after Stage I).

For the drawdown analysis, a series of LEM (c', ϕ') Bishop analyses were performed, as this type of analysis is more robust and computationally effective. For these analyses the soil geometry was kept constant, although the water level in the ditch was changed. As the water level changed in the excavated ditch, the water pressures changed in the dyke as well. The water pressure distribution in the dyke per drawdown level was estimated based on the pressure responses and judgement, see Figure 2.21(a) for the 1.5 m drawdown water level. Table 2.5 presents the factors of safety of the LEM analyses at different drawdowns.

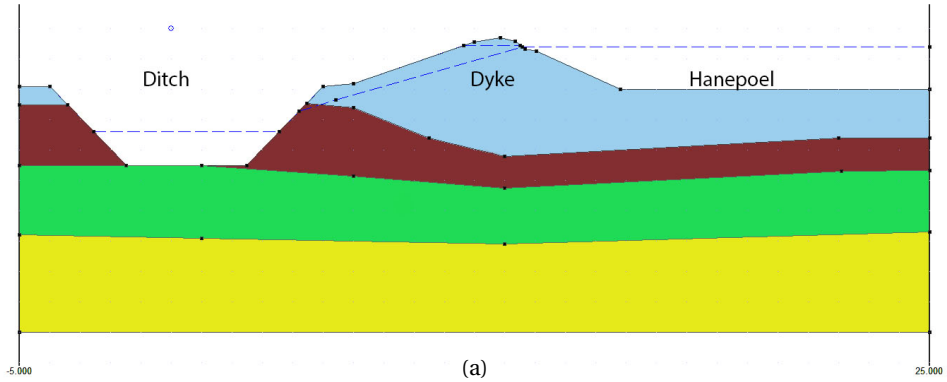

(a)

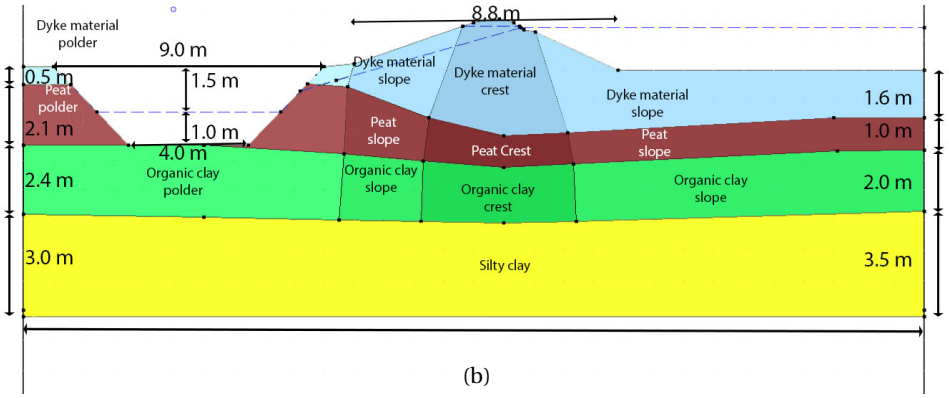

(b)

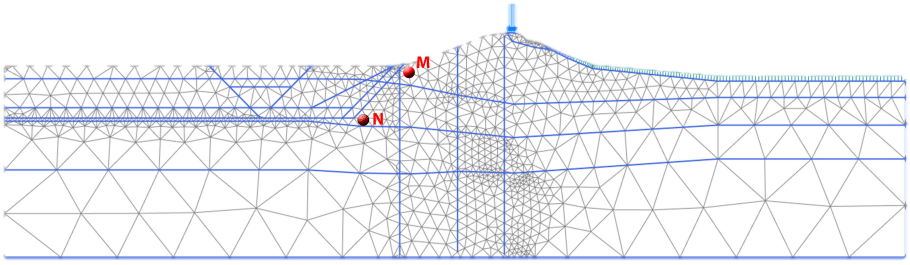

(c)

Figure 2.21: Discretisation of the cross-section, with the dyke material shown in blue, peat in brown, organic clay in green and silty clay in yellow. In (a) the LEM discretisation where each material layer has a single set of parameters, (b) the LEM discretisation where different material parameters have been specified relative to the crest (dark), slope (lighter) and polder (light), and (c) shows the FEM mesh.

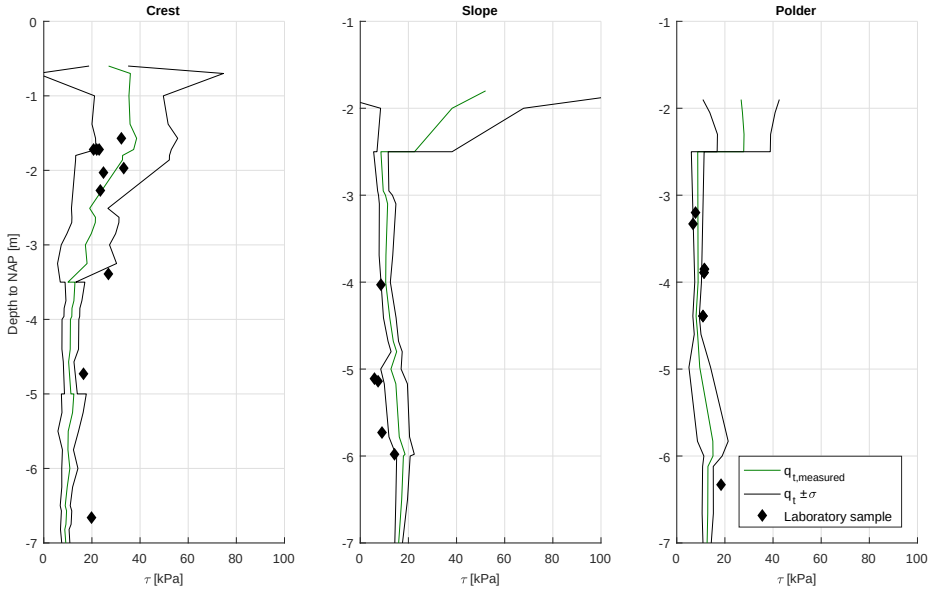

(a)

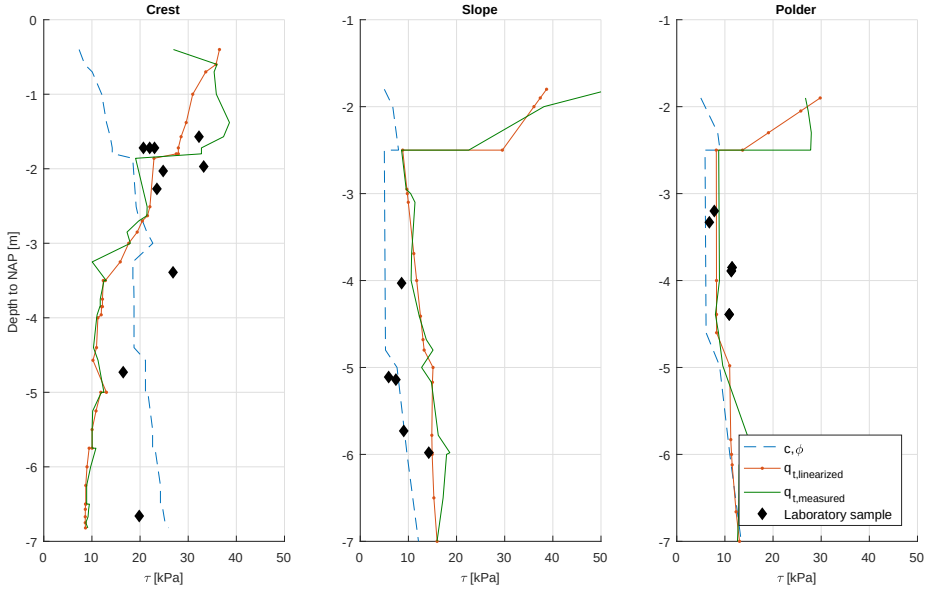

(b)

Figure 2.22: Effect of different strength estimate approaches under the crest, slope and polder compared to laboratory data (20 TXCIU and 4 DSS) (a) s_u based on q_t including the indication of (b) average strength based on different assumptions

Table 2.4: Factors of safety obtained from LEM calculations using different slip surface definitions and parameter sets.

	1 Zone		3 Zones	
	$\tau(c',\phi')$	$s_u(q_t(\mu^+))$	$s_u(q_t(\mu))$	$s_u(q_t(\mu-\sigma))$
Bishop	1.44	1.23	1.28	0.88
Uplift Van	1.63*	1.79	1.14	0.90
Spencer	0.83	1.12*	1.23	0.87

$^+$ μ is the mean *LEM surface reached the boundary of search region

Table 2.5: Factors of safety calculated during final drawdown (Stage VII) calculated using LEM with a Bishop failure surface and c',ϕ' strength paramters

Drawdown [m]	Factor of safety [-]	Corrected factor of safety [-]
0.00	1.16	1.32
0.50	1.09	1.24
0.75	1.01	1.15
1.00	0.93	1.06
1.25	0.84	0.95
1.50	0.79	0.90
2.00	0.73	0.83
2.50	0.70	0.80

A correction for 3D effects is made, with the correction factor of 1.13 determined by taking the ratio between 2D FEM and 3D FEM analyses of the dyke (see Section 2.8.2). The factor of safety from the LEM analysis falls below 1.0 between a drawdown of 1.00 m and 1.25 m. However, it was noted that the calculated stability is very sensitive to the input of the internal water levels.

2.8.2. FEM ANALYSES

The geometry of the layers was the same as those used in Section 2.8.1. The FEM mesh is shown in Figure 2.21(c). The boundary conditions for 2D and 3D analyses are similar. The bottom boundary is beyond the influence of the failure surfaces and therefore the displacements both horizontally and vertically were fixed. At the vertical boundaries, horizontal displacements were fixed and vertical displacements were free. For the 2D analysis, fully coupled hydro-mechanical analysis was performed. For the 3D analysis, c,ϕ'-reduction analysis was performed without the influence of water.

The water level in the Hanepoel was again fixed at NAP -0.6 m, and the water level in the ditch was fixed based on the drawdown imposed. In the 2D FEM analysis, the water level changes in the ditch have been used as an input for a coupled (hydro-mechanical) analysis where the water pressures in the dyke were calculated. In the coupled analysis, the following stages are considered:

- Stage I, saturation of the dyke: by increasing the water level in the dyke to the edge of the geometry (simulating the wetting).
- Stage II, first excavation: the soil is removed instantly in the geometry of the first excavation.
- Stage III, pumping: the water level in the ditch is lowered at the same rate as the field test, kept at 1.0 m drawdown for one day and then raised again at the same rate as the field test.
- Stage IV, the second excavation: after a waiting period, the soil is removed instantly in the geometry of the excavation.
- Stage V, pumping: the water level in the ditch is lowered at the same rate as the field test, kept at 1.0 m drawdown for slightly less than one day, as in the field test, and then raised again at the same rate as in the field test.
- Stage VI: the third excavation, after a waiting period, the soil is removed instantly resulting in the geometry of the final excavation.
- Stage VII: pumping, the water level in the ditch is lowered at the same rate as the field test until failure occurred.

In Figure 2.23, the results of the 2D FEM analysis are compared to measurements. The calculated groundwater head and displacements are taken at Points N and M, respectively, see Figure 2.21(c). The measured displacements were taken from an extensiometer at the south toe, and the ground water head was taken in the peat at the south toe. Figure 2.23 shows the measured and calculated responses. The displacements were set to zero at the start of the experiment, and the groundwater heads were obtained at slightly different locations although the trends are similar. The effect of the drawdown at Stage III, Stage V and Stage VII are clearly visible at days 9, 16 and 22, in both the experimental and numerical results. The excavation step, Stage II, two days before Stage III, is not clearly indicated in the experimental data, but a minor displacement is seen in the numerical analysis, while stage IV and Stage VI show similar (minor) responses in both the numerical analysis and the experimental data.

In the FEM analysis, the failure begins in Stage VII at a drawdown of 0.5 m and shows increasingly large displacements until 1.8 m drawdown when the calculation stops, i.e. the programme can not find a converged solution for the calculated displacements. These displacements match well with those observed (see Figure 2.23), although the observed measurements finish when the sensors are damaged due to the large displacements. These large displacements correspond to the factors of safety found in the LEM analyses where the embankment is stable at a drawdown of 0.75 m (Table 2.5) and the factor of safety is reduced to below 1.0 with a drawdown of 1.0 m. The calculated deviatoric strain, i.e. the failure surface, is shown in Figure 2.24(a). The failure surface is seen to be consistent with Figures 2.17 to 2.19, where the shear band at the toe is observed to be at the interface between the peat and the organic clay.

Because the ditch has a limited extent, the stresses in the dyke are only affected over a finite distance and thereby the extent of the possible failure is limited. Hence, a

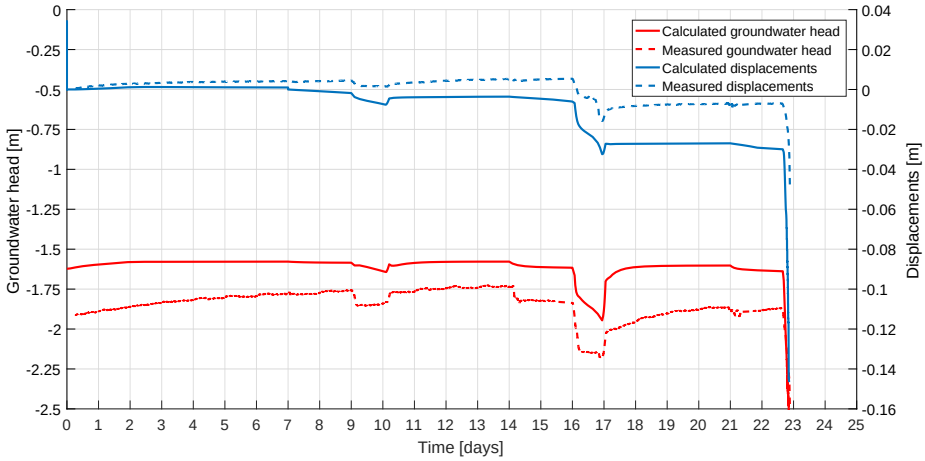

Figure 2.23: Measurements near the excavation and the results of FEM analysis at a point close to the bottom of the ditch. In red the displacements and in blue the groundwater head over the course of the experiment, from wetting the crest of the dyke, during the two excavations and lowerings of the water table, up to the failure.

comparison between 2D and 3D failure analysis was performed. The 3D FEM analysis is different from the 2D FEM analysis in the following ways: (1) the geometries of the layer boundaries are taken from the individual CPTu profiles and linearly interpolated between the points; (2) the excavation is limited to 50 m along the dyke. Figure 2.24(c) shows a contour plot of the displacements at failure concentrated to the right of the centre of the ditch, which is between the centre and south in the experiment. Comparing the factors of safety calculated for 2D (F_{2D} = 1.13) and 3D (F_{3D} = 1.28) leads to a proposed correction factor of 1.14 that was used to correct the factors of safety found in Table 2.5.

For the 2D analysis, the observed failure occurred at a drawdown of 1.60 m. This can be compared to the calculated strains in the FEM analysis shown in Figure 2.25, here indicated for different stages of the drawdown (representing hourly intervals).

It can be seen that, by the start of Stage VII, there is already an initial shear band formed from the bottom of the excavation through the peat and reaching the dyke material. This shear band then extends from the toe to the top of the dyke crest as drawdown takes place. At a drawdown of 0.6 m, a second shear band starts to form with a shorter radius. This is consistent with the observed deformations at failure in Figure 2.19, which shows a large differential deformation from the ditch and in the slope, and a smaller differential displacement from the ditch to the toe above. In the strength reduction analyses, at a drawdown in the ditch of 1.4 m the failure surface (localised shear) changes location. Before the 1.4 m drawdown, the calculated failure surface goes from the bottom of ditch to the crest, and after the 1.4 m drawdown the shape of the calculated failure surface changes and goes from the bottom of the ditch to halfway the slope of the dyke. This indicates that a significant change is made in the stresses, indicating instability.

In the 2D FEM analysis, at a drawdown of 1.6 m the rate of calculated strain increases significantly, and can be interpreted as an indication of failure. However, in the coupled

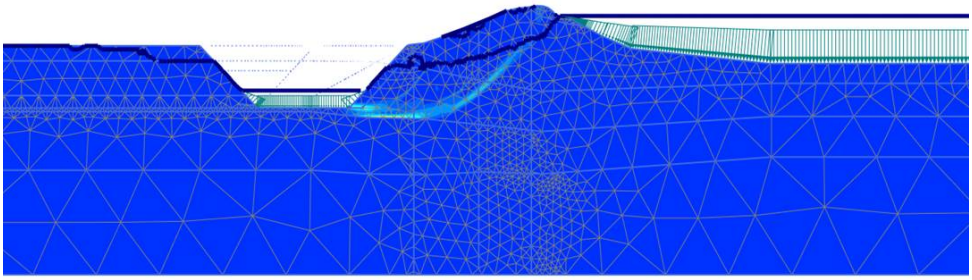

(a)

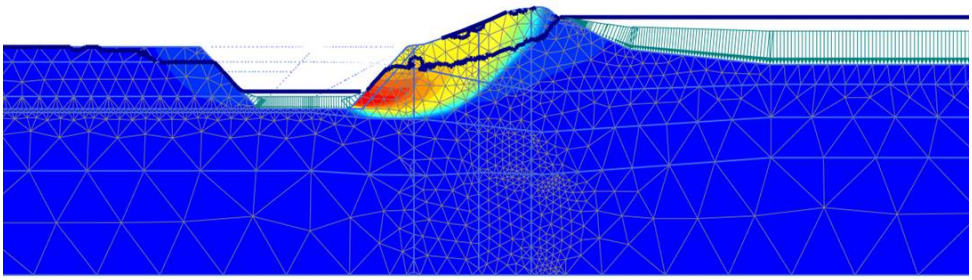

(b)

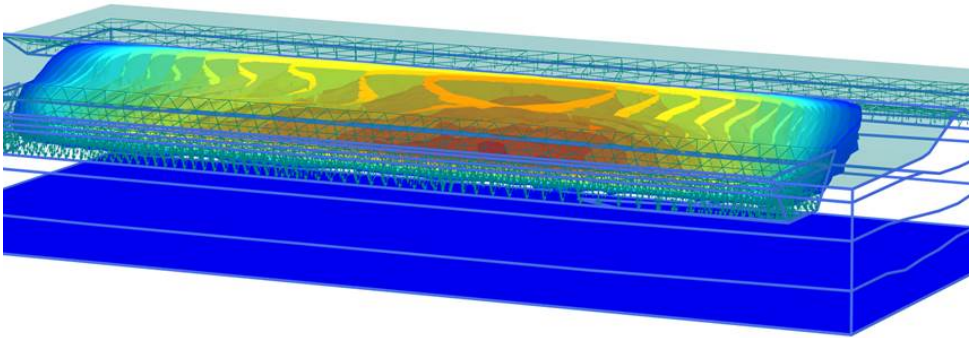

(c)

Figure 2.24: Results of the numerical analysis at failure (note that the dark blue line is the calculated phreatic head): (a) deviatoric strain, showing that the strain is localised at the toe and forks to the slope and crest of the dyke, (b) the resultant displacements, (c) three dimensional resultant displacements at failure, in which the maximum displacements (indicated in red) are to the right of the centre.

analysis time plays an important role. An analysis of what would have happened if, after Stage VI, the water levels in the ditch and Hanepoel were to remain at a level of NAP -1.8 m and NAP -0.6 m, respectively, indicates that the dyke would have failed over a period of 100 days as the water in the dyke equilibrated.

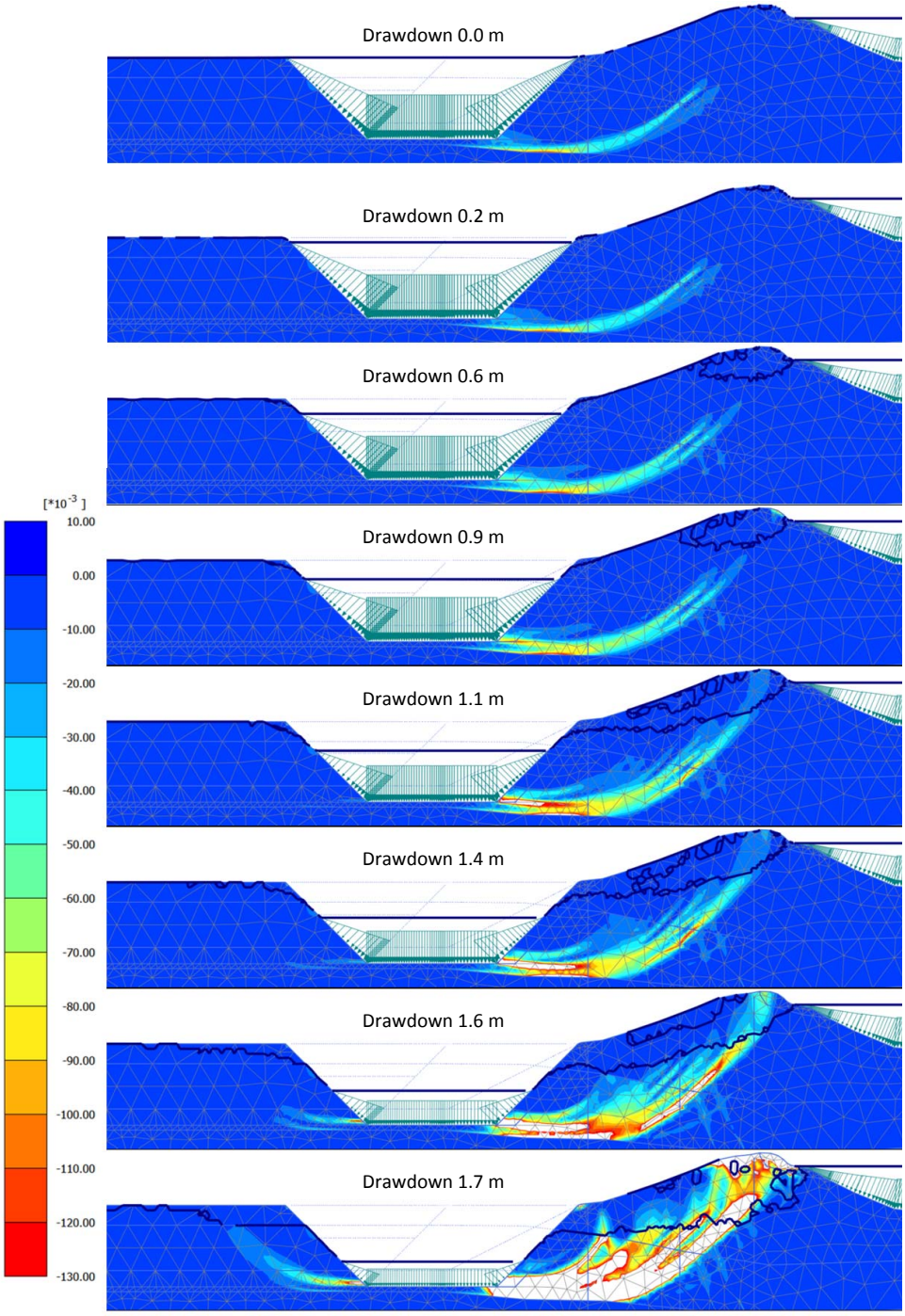

Figure 2.25: 2D FEM results of deviatoric strain evolution with drawdown level in hourly intervals (i.e. each plot is 1 hour after previous plot, note that the dark blue line is the calculated phreatic head). In this overview, a white contour signifies extreme strain

2.9. DISCUSSION

This field test that adds to the body of data of avaiable field tests, has led to a clear failure on a dyke that has in contrary to existing field tests existed for several centuries. The failure was observed with sensors leading to a large amount of data that have been used to compare with numerical analyses. In these analyses, 3D effects and temporal effects had to be taken into account as the dyke was dynamically loaded (by removing the water over the course of several hours) and the failure occurred at a discrete location and not over the entire dyke section.

When comparing the measurements and numerical analysis, it can be seen that the physics governing both the behaviour leading up to the failure and during the failure itself are well understood.

The geometry and boundary conditions leading to failure have been designed so that the failure would occur on the desired day, as indicated by the calculated factors of safety in LEM analyses (Table 2.5) that reduce from (1.16/1.32) with a full ditch and drop to (0.70/0.80) when the ditch would have been depleted. The consequence of this is that the detailed constitutive behaviour is of less importance to the failure than under normal conditions.

The linear elastic, perfectly plastic parameters based on a Mohr-Coulumb failure surface have been determined at a 5% strain level. For the dyke material and clay this strain level is close to the ultimate strength found in the consolidated undrained triaxial data, as indicated in Figure 2.9. For the peat, however, the 5% strain level is not near the ultimate strength and with further axial strain the peat shows hardening behaviour.

Were the full constitutive behaviour to be taken into account, it is expected that the global shape and moment of the analysed failure would not change. However, details of the failure would change, especially for the behaviour through the peat. The constitutive behaviour of the peat has been studied in the Reliable Dykes research project by (Muraro, 2019).

From the field and laboratory data, it can be seen that the layer properties vary, although the analyses performed in this chapter have used mean values. In this thesis special attention is given to the effect of variation in the strength properties, including their effect on the calculated stability of the dyke and confidence in the calculated stability. In Chapter 4 the effect of variation of material properties is studied.

2.10. SUMMARY

In this chapter, an experiment was presented where an existing dyke was brought to failure by excavating a ditch in front of the dyke. To prepare for the test, an extensive site investigation was performed consisting of CPTu tests and borings to collect material used in laboratory testing. Based on the site investigation, sensors were installed to track the behaviour of the dyke during the experiment. Sensors included horizontal and vertical deformation measurements and pore water pressure sensors.

At the start of the experiment, a wetting system on top of the dyke was used. A ditch was created in front of a 50 m stretch of dyke and filled with water. To induce failure of the dyke, the ditch was incrementally increased in size and the water level in the ditch was lowered.

The size and location of the excavated ditch were designed using LEM analyses, and the displacements and pore pressures during the test have been modelled using FEM. In the numerical analyses, detailed 3D effects and variation in material properties have not been taken in account. The results of the numerical analyses and results of the failure experiment have similar qualitative behaviour.

REFERENCES

Andriessen, H.-P. (2015). Requiem voor een poldertje, algemeen dagblad, 09-10-2015.

Balthasar, F. (1611). Nationaal archief, den haag, verzameling binnenlandse kaarten hingman, nummer toegang 4.vth, inventarisnummer f.

Lehtonen, V., Meehan, C., Länsivaara, T. & Mansikkamäki, J. (2015). Full-scale embankment failure test under simulated train loading. *Géotechnique* **65**, No. 12, 961–974.

Lindenberg, J., Van, M., Koelewijn, A., Zwanenburg, C., Lambert, J., Van der Meer, M. & Teunissen, P. (2002). Bergambacht field test evaluation. *Technical report*, Delft Cluster.

Muraro, S. (2019). *The deviatoric behaviour of peat: a route between past empiricism and future perspectives*. Ph.D. thesis, Delft University of Technology.

Robertson, P. K. (2009). Interpretation of cone penetration tests — a unified approach. *Canadian Geotechnical Journal* **46**, No. 11, 1337–1355.

Zwanenburg, C., Den Haan, E. J., Kruse, G. A. M. & Koelewijn, A. R. (2012). Failure of a trial embankment on peat in booneschans, the netherlands. *Géotechnique* **62**, No. 6, 479–490.

3

MEASURING VERTICAL AND HORIZONTAL VARIABILITY IN SOILS

Although the impact of soil variability on geotechnical behaviour has been widely researched, the measurement of the variability is significantly less often attempted. Soils typically exhibit different distances over which their properties are significantly correlated, often referred to as scales of fluctuation. Due to deposition and other processes, these are generally anisotropic and often have their principal axes in the vertical direction and horizontal plane. However, obtaining these scales of fluctuation is not trivial, particularly in the horizontal plane due to the limited amount of data available when using traditional measurement methods, e.g. the Cone Penetration Test (CPT). In this chapter two methods to obtain geotechnical scales of fluctuation are compared. The limitations and robustness of each method are identified, in terms of the amount and spacing of data required for practical use, as well as the use of non-uniform data which can be common in practice. The methods are first tested with synthetic data and then real, newly-collected, field data. The real set, a field of 100 CPTs, is presented and can form part of a body of work to more comprehensively understand both vertical and horizontal scales of fluctuation.

Elaborations of the field-data collected in this chapter are presented and published in de Gast *et al.* (2017, 2019), the theoretical elaboration is partly presented in de Gast *et al.* (2018) and has been submitted as an article to Géotechnique.

3.1. INTRODUCTION

Variation in soil properties is one of the main challenges in geotechnical engineering (Honjo, 2011), and has been shown to be important in many types of geotechnical analyses, including: the geotechnical behaviour of shallow, strip, and pile foundations (Jaksa *et al.*, 2005; Suchomel & Mašín, 2010; Naghibi *et al.*, 2016); retaining walls (Sert *et al.*, 2016); liquefaction of hydraulic sand fills (Wong, 2004; Hicks & Onisiphorou, 2005; Popescu *et al.*, 2005); and slope stability (Griffiths & Fenton, 1997; Hicks & Samy, 2002; Spencer & Hicks, 2007; Hicks & Spencer, 2010; Hicks *et al.*, 2014; Li *et al.*, 2016; Varkey *et al.*, 2018, 2019). It has been shown, especially for embankments (Spencer & Hicks, 2007; Hicks *et al.*, 2014), that the the spatial variation of material properties in combination with the problem geometry plays an important role in the slope stability and failure mode.

Comprehensive theoretical overviews on how to quantify the spatial variation in soils are given by Vanmarcke (1977); Campanella *et al.* (1987) and Wickremesinghe & Campanella (1993) and later discussed by Fenton (1999a,b) and Griffiths & Fenton (2007). It has been suggested that the scale of fluctuation (SoF), generally described as the distance over which data are significantly correlated, can be estimated using a range of techniques; in particular, by using an auto-correlation function, Fourier analysis or a variogram function. These techniques require a substantial amount of data, such as obtained by cone penetration tests (CPTs). While CPTs do not directly measure soil properties, their measurements are known to be correlated to them. Therefore, by utilising the spatial variability of the CPT measurements, an estimate of the spatial variability of the soil properties can be made without having to transform the measurement data. However, little experimental evidence that considers the scale of fluctuation, especially in the horizontal plane, is available, although some attempts have been made to quantify the horizontal scale of fluctuation, see Table 3.1.

Table 3.1: Chronoligical summary of reported scales of fluctuation using CPT data (after Nie *et al.*, 2015; Arnold, 2016)

Material	θ_v	θ_h	Source
Offshore soils	-	30.0	Hoeg & Tang (1977)
Sand	0.1-0.7	-	Campanella *et al.* (1987)
Offshore sand	-	14.0-38.0	Keaveny *et al.* (1989)
Deltaic soil	0.2-0.4	-	Wickremesinghe & Campanella (1993)
Clay stiff	0.1-0.2	0.1-2.0	Jaksa (1995)
Silty clay	1.0	5.0–12.0	Lacasse & de Lamballerie (1995)
Clay sensitive	2.0	-	Chiasson *et al.* (1995)
Clay stiff	-	0.1-4.4	Jaksa *et al.* (1999)
Clay stiff	0.2–0.5	23.0–66.0	Phoon & Kulhawy (1999)
Clay	0.3-0.5	-	Cafaro & Cherubini (2002)
Sandy soils	0.1-1.2	-	Uzielli *et al.* (2005)
Sand (infill)	0.4-0.9	7.0	Lloret-Cabot *et al.* (2012)
Sand	0.1 -0.3	1.2-2.0	Firouzianbandpey *et al.* (2014)
Clay silty	0.1 -0.3	-	Pieczyńska-Kozłowska (2015)
Fluvial deposits	0.1 -1.0	-	Pieczyńska-Kozłowska *et al.* (2017)
Sand	0.25 - 0.6	0.5 - 2.6	Ching *et al.* (2018)

It has been previously observed that, by taking account of spatial variation and the location of measurement data, uncertainty in the response of a structure is reduced (e.g. Jaksa *et al.*, 2005; Lloret-Cabot *et al.*, 2012; Li *et al.*, 2016), and given more available information, i.e. more CPTs, the better the estimation of the SoF (Lloret-Cabot *et al.*, 2014). However, the decrease in uncertainty in the estimated SoF as the number of CPTs increases has not yet been quantified. A challenge in the calculation of reliable horizontal scales of fluctuation is that, unlike using CPTs in the vertical direction, there are no standard methods of geotechnical investigation giving high spatial resolution in the horizontal plane. Clearly, the required spacing of collected data is important and it strongly influences the cost of a site investigation.

The origin of spatial variability is often attributed to geological processes occurring in the deposition of soil layers (Phoon & Kulhawy, 1999). Given that there may be many processes involved in the transport and deposition of sediments, it may be hypothesised that there may be multiple, separate, scales of fluctuation (e.g. Vanmarcke, 1983). For example, a large-scale variation may occur due to seasonal changes in the deposition, whereas a small-scale variation may be due to local hydrodynamic processes, e.g. eddy currents.

In this chapter, two existing methods to calculate the auto-correlation function are reviewed and compared for their effectiveness in analysing synthetic data for a range of CPT spacings. Computer generated data, with a known SoF, have been used to investigate the impact of having differing amounts of site investigation data, and the uncertainty in the back-figured SoF has been quantified. A design chart and underlying equation have then been proposed to estimate the uncertainty arising from different testing schemes. A row of 29 closely-spaced CPTs, from within a larger field test of 100 CPTs, from a regional dyke in the Netherlands, has been analysed and the resulting data used to validate the proposed approach. This field test has been used to demonstrate the consequences of collecting different amounts of data during site investigations. A simplified dyke analysis has been undertaken using the detected variability from the field test to demonstrate the impact of the uncertainty on the predicted dyke response.

3.2. THEORETICAL BACKGROUND

Soil properties are variable, although they are generally related to the properties of the material in close proximity. A convenient measure of the spatial variability is the auto-correlation length θ, referred to as the scale of fluctuation. Loosely speaking, it is the distance within which material properties are significantly correlated. Conversely, the properties at two points separated by a distance greater than θ will be largely uncorrelated (Griffiths & Fenton, 1997). The scale of fluctuation has been defined by Vanmarcke *et al.* (1986) as

$$\theta = 2\int_0^\infty \rho(\tau)d\tau \tag{3.1}$$

where $\rho(\tau)$ is the auto-correlation function describing the spatial auto-correlation structure and τ is the lag distance, i.e. the distance separating two points. Hence, θ is the area under the auto-correlation function over the range $-\infty \leq \tau \leq \infty$, and, while it

can be different in any direction, for soils it is commonly considered to be unique in the vertical and horizontal directions due to deposition processes.

Note that other techniques can also be used to describe the spatial auto-correlation of data. For example, in the mining industry spatial auto-correlations are commonly described by semi-variograms, which are constructed using the squared difference in the property of interest at different lag lengths. According to Baecher & Christian (2003), the semi-variogram requires a less restrictive statistical assumption on stationarity (i.e. the requirement of a constant mean and standard deviation) than the auto-correlation function. However, its use in spatial interpolation and engineering can be more difficult, as the range, sill and nugget need to be identified. Therefore the auto-correlation approach is used and further used in this chapter.

3.2.1. EXPERIMENTAL AUTO-CORRELATION FUNCTION

The method used to determine the experimental scale of fluctuation (e.g. Lloret-Cabot *et al.*, 2014) compares a theoretical auto-correlation function $\rho(\tau)$ with an experimentally determined auto-correlation function $\hat{\rho}(\tau)$ The error in approximating the experimental auto-correlation function by a theoretical function is given by

$$Er(\rho) = \sum(\rho(\tau) - \hat{\rho}(\tau))^2 \tag{3.2}$$

where $Er(\rho)$ is the error in the approximation and is defined as the sum of the squared differences between the values of the two functions at the lag distances considered. The experimental θ is the value of θ that minimises $Er(\rho)$.

Two approaches have been proposed for estimating the auto-correlation function from data. The first compares pairs of data and is the most commonly used, whereas the second uses the frequency data determined via a Fourier transform. These two approaches are presented below.

The experimental auto-correlation function is the auto-correlation function derived from discrete (e.g. measurement) data, and can be obtained from the experimental covariance function $\hat{\gamma}(\tau)$ as

$$\hat{\rho}(\tau) = \frac{\hat{\gamma}(\tau)}{\hat{\gamma}(0)} \tag{3.3}$$

The experimental covariance function was presented by Vanmarcke (1983) for equally spaced data as

$$\hat{\gamma}(\tau) = \frac{1}{k-l}\sum_{j=1}^{k-l}(y_j - \hat{\mu})(y_{j+l} - \hat{\mu}) \tag{3.4}$$

which can be, as in variance estimation, adapted as an unbiased estimator,

$$\hat{\gamma}(\tau) = \frac{1}{k-l+1}\sum_{j=1}^{k-l}(y_j - \hat{\mu})(y_{j+l} - \hat{\mu}) \tag{3.5}$$

or adapted for unequally spaced data as

$$\hat{\gamma}(\tau) = \frac{1}{t-1} \sum_{j=1}^{t} (y_j - \hat{\mu})(y_{j+\Delta j} - \hat{\mu}) \tag{3.6}$$

where $\hat{\mu}$ is the estimated mean (or trend) of the dataset, j is a counter representing the index of the first of a pair at lag distance τ, $l = 1, 2, \ldots, k$ is a counter representing the index spacing of pairs of data with k being the total number of observations, Δj represents the index spacing of a specific pair of observations for a non-uniformly distributed dataset, and t is the number of pairs at lag distance τ. Note that, for the estimator given by Equation (3.3), it is desirable that the data are equally spaced (Fenton & Griffiths, 2008) at any spacing τ, to ensure higher quality results. However, this may reduce the number of lag distances considered, and may be unrealistic with measured data as it is not common to have equally (closely) spaced data. Therefore, Equation (3.6) is suggested to account for non-equidistant spacing. It is also possible to group data into 'bins' to increase the number of pairs, although the resolution will then be affected. Vanmarcke (1983) showed that the scale of fluctuation can also be found by investigating the frequency domain of the data, i.e. the spectral density function. The spectral density function $G(\omega_k)$ can be generated via a Fourier transform and, in the case of discrete and unevenly spaced data, a non-uniform discrete Fourier transform (NDFT):

$$\begin{aligned} G(\omega_k) &= \sum_{n=0}^{n_t} \frac{y_j - \hat{\mu}}{\hat{\sigma}} e^{i x_j \omega_k} \\ \omega_k &= \frac{2\pi k}{D} \\ k &= \frac{nD}{n_t} \end{aligned} \tag{3.7}$$

where $\hat{\sigma}$ is the estimated standard deviation of the dataset, D is the domain size, i is the imaginary number, ω_k is the domain frequency, n is a counter from 0 to n_t in which n_t is the number of frequencies considered, x_j is the location of data point y_j, and j is a counter from 1 to the number of data points. The original data can be reconstructed from the inverse of the NDFT,

$$y(x) = \sum_{k=1}^{k} G(\omega_k) e^{+iy\omega_k} \tag{3.8}$$

and an experimental auto-correlation function can be estimated via a Fourier transform of the power spectrum, which is the square of the spectral density function $|G(\omega_k)|^2$ (Vanmarcke, 1983):

$$\hat{\rho}(\tau) = \sum_{k=1}^{k} |G(\omega_k)|^2 e^{+i\tau\omega_k} \tag{3.9}$$

Figure 3.1 summarises the relationships between a dataset, its Fourier transform, its auto-correlation function, and its power spectrum.

It has been found by the author that, to get a best estimate of the experimental auto-correlation function from CPTs in both methods, all of the available data strings should

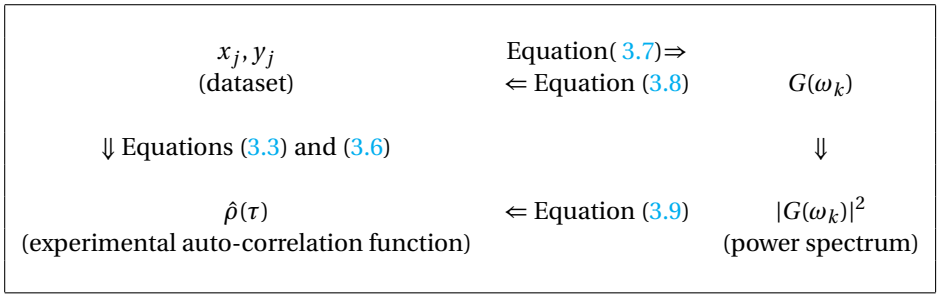

Figure 3.1: Relationships between functions used to calculate the experimental auto-correlation function

be analysed together, e.g. multiple CPT profiles, and for each lag distance the mean of all of the experimental auto-correlation functions used.

3.2.2. UNBIASED ESTIMATOR

In Equation (3.6), the sum of the pairs is normalised by the number of pairs considered at the chosen lag distance minus one, making it an unbiased estimator, in the same way as for an unbiased estimation of the variance. The auto-correlation function obtained by the Fourier transform is equal to the biased estimator, although it does not have such a simple corrector. A correction is here proposed using a known auto-correlation. When performing an analysis using Equations (3.7) and (3.9), where $y_j = 1$ for all x_j, the resulting auto-correlation function should also be equal to 1 for every τ. However, due to the bias, this is not the case and, for each lag distance, a coefficient has been computed to correct to an unbiased estimator. Figure 3.2 compares the calculated bias to the theoretical solution and shows the derived correction factor.

3.2.3. THEORETICAL AUTO-CORRELATION MODEL

The theoretical auto-correlation function (or correlation structure) can take various forms, as illustrated by Table 3.2 which lists some common auto-correlation models. The model which best fits the data should be selected.

Table 3.2: Common theoretical auto-correlation models (Fenton, 1999b)

Correlation model	Formula
Gaussian	$\rho(\tau) = e^{-\pi\left(\frac{\lvert\tau\rvert}{\theta}\right)^2}$
Triangular	$\rho(\tau) = \begin{cases} 1-\frac{\lvert\tau\rvert}{\theta} & \text{if} \quad \lvert\tau\rvert \le \theta \\ 0 & \text{if} \quad \lvert\tau\rvert > \theta \end{cases}$
Spherical	$\rho(\tau) = \begin{cases} 1-1.5\left\lvert\frac{\tau}{\theta}\right\rvert + \left\lvert\frac{\tau}{\theta}\right\rvert^3 & \text{if} \quad \lvert\tau\rvert \le \theta \\ 0 & \text{if} \quad \lvert\tau\rvert > \theta \end{cases}$
Markov	$\rho(\tau) = e^{\frac{-2\lvert\tau\rvert}{\theta}}$

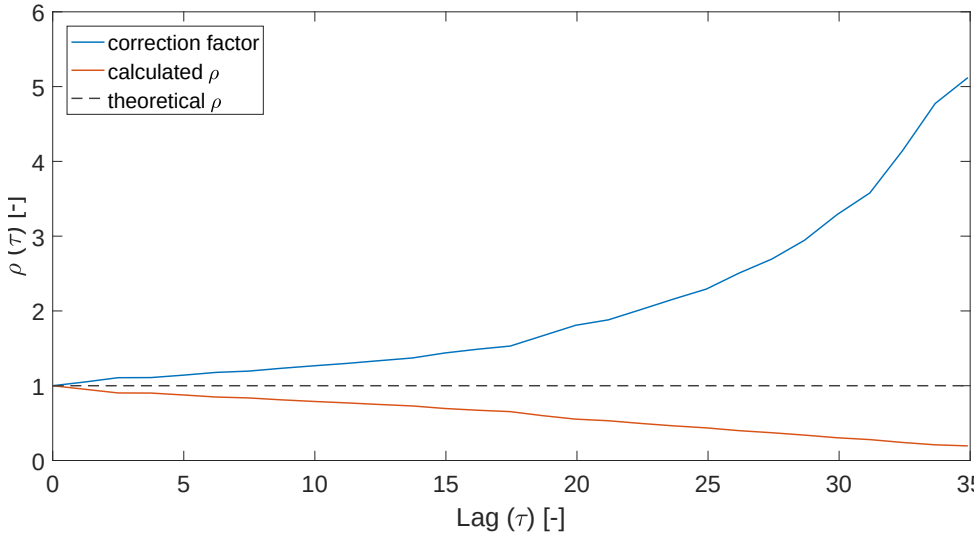

Figure 3.2: Example of obtaining a correction factor for the correction of NDFT from a biased to an unbiased estimate. The known theoretical ρ divided by the calculated $\hat{\rho}$ (Equations (3.7, 3.9)) results in the correction factor

3.2.4. CORRELATION STRUCTURES

Theoretical auto-correlation functions can be combined to better estimate the experimental auto-correlation. For example, a single composite auto-correlation function can be constructed using different scales of fluctuation, as in Figure 3.3 (Vanmarcke, 1983), and even by combining different auto-correlation models, although no elaboration on the approach or how to determine multiple scales was given. In this section, such an elaboration is proposed. In Vanmarcke's approach, an equivalent equation to Equation (3.1) can be used to determine an average scale of fluctuation, θ_{avg}, i.e.

$$\theta_{avg} = 2\int_0^\infty \rho_{com}(\tau)d\tau \tag{3.10}$$

where ρ_{com} is the composite auto-correlation function constructed as the weighted average of the component correlation functions (ρ_{θ_i}),

$$\rho_{com}(\tau) = c_1\rho_{\theta_1}(\tau) + c_2\rho_{\theta_2}(\tau) + \cdots + c_i\rho_{\theta_i}(\tau) \tag{3.11}$$

where

$$0 \le c_i \le 1 \quad \text{and} \quad \sum_i c_i = 1 \tag{3.12}$$

Integration of Equation (3.11) leads to

$$\int_0^\infty \rho_{com}(\tau)d\tau = c_1\int_0^\infty \rho_{\theta_1}(\tau)d\tau + c_2\int_0^\infty \rho_{\theta_2}(\tau)d\tau + \cdots + c_i\int_0^\infty \rho_{\theta_i}(\tau)d\tau \tag{3.13}$$

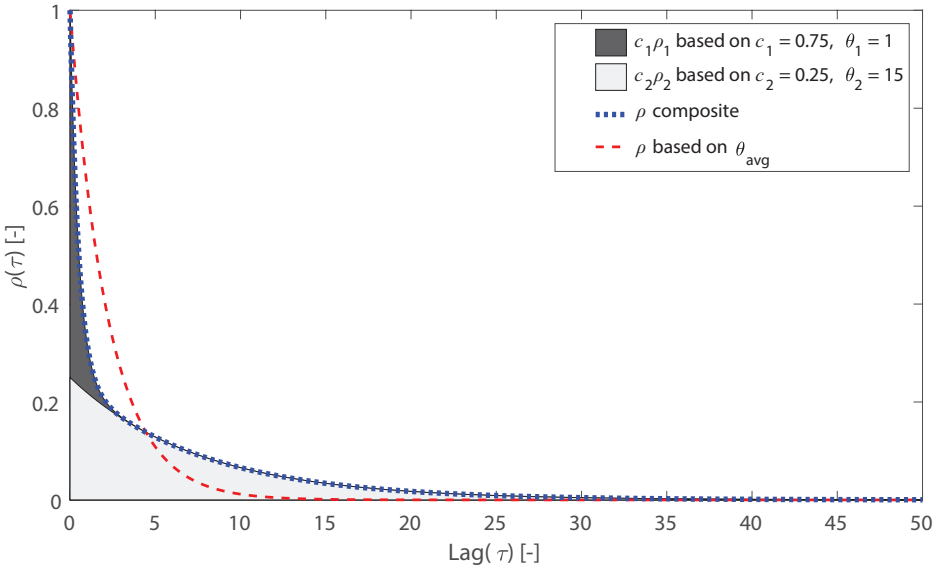

Figure 3.3: Combination of two theoretical scales of fluctuation and corresponding single scale of fluctuation (after Vanmarcke, 1983)

and substitution of Equation (3.10) gives

$$\theta_{avg} = c_1\theta_1 + c_2\theta_2 + \cdots + c_i\theta_i \tag{3.14}$$

The combined correlation function that most closely fits the experimental auto-correlation function is found by minimising the error

$$Er(\rho_{com}) = \sum(\rho_{com}(\tau) - \hat{\rho}(\tau))^2 \tag{3.15}$$

In theory any number of components can be used in a composite auto-correlation function, although the number of unknowns which need to be determined is twice the number of components and the computational effort increases significantly with each additional component. Therefore, the examples here are limited to a maximum of a two-component model.

The algorithm proposed to determine two scales of fluctuation from CPT data (e.g. cone tip resistance)is as follows:

1. Detrend the data with respect to depth;
2. Calculate the experimental auto-correlation function using Equations (3.3, 3.6);
3. Calculate c_1, c_2, θ_1 and θ_2 using the following algorithm:

- Loop through $0 < c_1 \leq 1$ in small steps

- Using Equation (3.12), $c_2 = 1 - c_1$
- Loop through $0 < \theta_1 \leq \theta_{max}$ in small steps (θ_{max} is the maximum θ investigated)
  - Loop through $0 < \theta_2 \leq \infty$ in small steps (note a practical approach to approximate ∞, e.g. $\infty \approx 5D$, is needed)
    - Calculate the composite auto-correlation function using Equation (3.11)
    - Calculate the error using Equation (3.15)
  - End loop
- End loop

- End loop

4. Select the combination of c_1, c_2, θ_1, θ_2 with the smallest error.

The step size for the algorithm can be selected based on computational effort and the required resolution of the resulting composite θ. It is reasonable for the maximum θ_1 investigated, i.e. θ_{max}, to be selected as the domain length D. A zero correlation length means that the data points are spatially uncorrelated and an infinite correlation length means that they are fully correlated, i.e. constant.

Figure 3.3 shows an example of combining two auto-correlation functions with different weights and different θ, as well as the auto-correlation function with a single average θ determined via Equation (3.14).

3.2.5. FOOTNOTE ON USING REAL DATA

If real CPT data are used, the following should be considered: (1) typical data are non-negative, requiring a careful estimation and removal of the mean trend; (2) properties can change due to underlying physical processes and non-statistical uncertainty. For the analysis of the scale of fluctuation, the underlying physical properties of the data should be normalised, which involves 2 steps: (1) de-trending and (2) normalising the variance. Errors in normalising will influence the calculated experimental auto-correlation function. When de-trending, one should be careful not to over de-trend the data; that is, the removal of a trend should be explained by a physical process, e.g. changing material, gradual change of the material, increasing effective stress (if the material response is stress dependent), history of loading of the material. The data are, after de-trending, assumed to be stationary. A method to test for stationarity of soil layers was used by Phoon *et al.* (2004), i.e. the modified Barlett test, where groups of data are separated and the calculated variances are compared for stationarity.

3.3. INVESTIGATION USING SYNTHETIC DATA

The effectiveness of the two proposed methods (i.e. experimental auto-correlation function and spectral density function) to obtain the experimental auto-correlation function for a set of data was first investigated using computer generated data, i.e. data where the scale of fluctuation and auto-correlation were known a priori. 1D strings of data

analogous to CPT profiles were generated using Cholosky decomposition (Alabert, 1987; Davis, 1987; van den Eijnden & Hicks, 2017). Figure 3.4(a) shows an example generated dataset, and illustrates how these data were processed using each method. The data were generated using a mean of 0, a standard deviation of 1 and a Markov auto-correlation structure with a scale of fluctuation of 5 (units of length). In Figure 3.4(a), x_j is the distance (unit of length) and the generated parameter (or measurement) value is represented by y_j. Figure 3.4(b) shows the spectral density function computed using Equation (3.7), whereas Figures 3.4(c) and 3.4(d) show the auto-correlation functions determined using Equations (3.3) and (3.6), and Equations (3.7) and (3.8), respectively. In these figures, the auto-correlation functions are compared with the true correlation function (from which the data were generated) shown in red.

Figures 3.4(c) and 3.4(d) show that, as the lag length increases, the experimental auto-correlation function, obtained either directly or via NDFT, oscillates, due to less available data, i.e. fewer pairs. In order to improve the estimate of the auto-correlation function over the whole lag length range, it is helpful to average multiple experimental auto-correlation functions, e.g. multiple CPT measurements. Figure 3.5 shows that, as more synthetic CPT strings are used in the approximation, the computed auto-correlation structure improves. The error Er, calculated using Equation (3.2), reduces from around 8.0 (1 CPT) to 2.0 (5 CPTs) to 0.1 (100 CPTs). Importantly, oscillations are delayed until larger lag lengths, implying that more data are needed for larger scales of fluctuation.

The same process was undertaken for data generated using two scales of fluctuation. Once again, the data strings (synthetic CPT profiles) were generated based a mean of 0 and a standard deviation of 1, but now with an auto-correlation function built from two Markov auto-correlation models with scales of fluctuation of θ_1=1 and θ_2 = 15 and two respective weighting coefficients of c_1 = 0.75 and c_2 = 0.25, giving θ_{avg} = 4.5. 100 data sets were generated using these input parameters and the 100 resulting experimental auto-correlation functions were averaged. Figure 3.3 shows the theoretical combination of the scales of fluctuation, while Figure 3.6 shows the result of analysing 100 data sets using Equations (3.10-3.11, 3.13-3.15) and compares it to the result based on a single auto correlation function. The double scale of fluctuation model has a much better fit to the experimental auto-correlation function than the single scale of fluctuation model, as confirmed by respective errors of Er = 0.07 and Er = 0.23.

It is noted that using 100 sets of data may not be possible in practice, and that, while using multiple scales of fluctuation the solution is more flexible, it is likely that more data would be needed than for identifying a single scale of fluctuation. However, it is also reasonable to assume that, for larger scales of fluctuation, more data are needed anyway to calculate both large and small scales of fluctuation accurately. These questions are investigated in the following section.

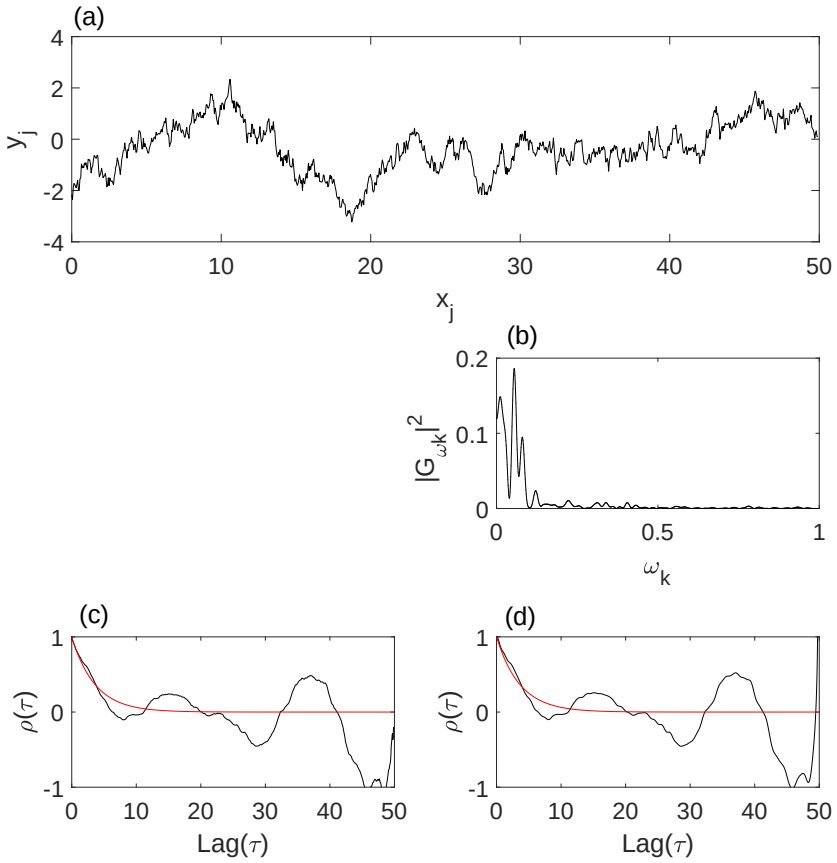

Figure 3.4: Example auto-correlation functions derived from generated data. (a) generated data based on Markov auto correlation with $\theta = 5$, (b) power spectrum density function $|G(\omega_k)|^2|$, (c) auto-correlation function using Equations (3.3, 3.6), and (d) auto-correlation function using Equations (3.7, 3.8).

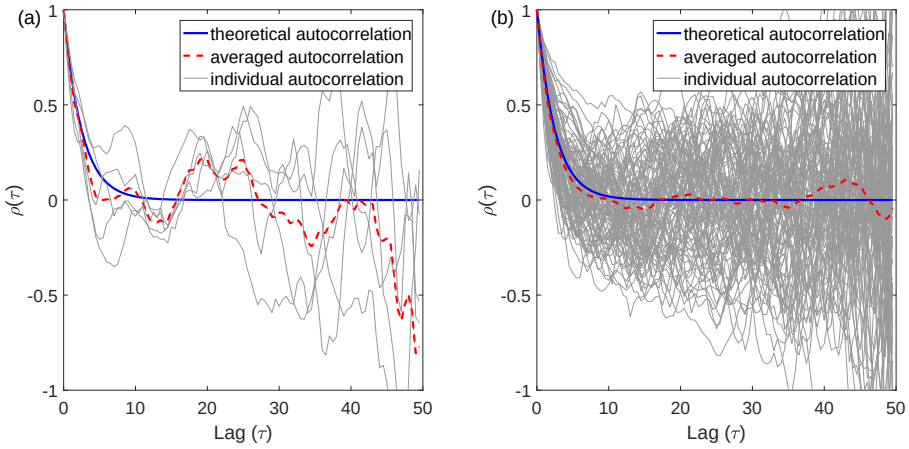

Figure 3.5: Individual (in grey) and averaged (in red) experimental auto-correlation functions. (a) based on 5 individual functions, and (b) based on 100 individual functions.

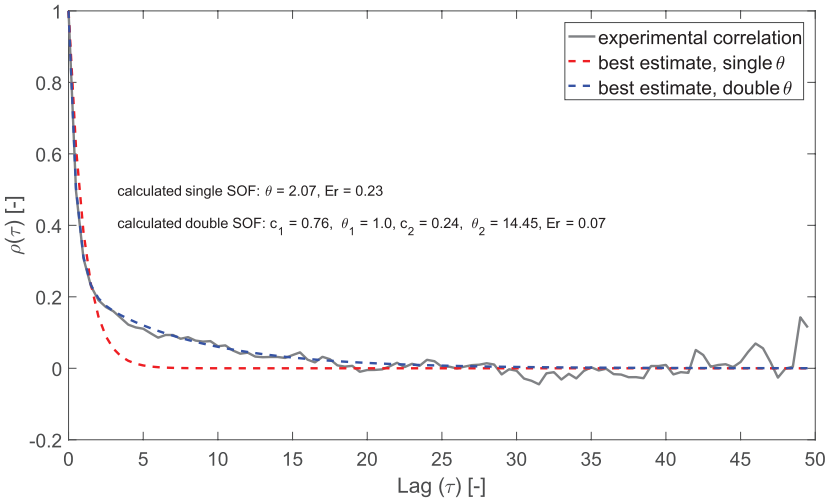

Figure 3.6: The experimental auto-correlation function generated by averaging data from 100 realisations generated using two scales of fluctuation, 1 and 15, with respective weighting coefficients of 0.75 and 0.25.

3.3.1. USE OF MULTIPLE DATA SETS

In order to test the effectiveness of both suggested auto-correlation function methods, different variables were investigated: (1) number of data sets combined – which is analogous with the number the number of CPT locations; (2) total number of data points used – which is analogous with the total number of data points of all CPTs in a layer; (3) value of θ.

To investigate the number of data sets, a numerically generated series of data sets with a mean of 0, standard deviation of 1 and a Markov auto-correlation structure with a single $\theta = 5$ was used. The length of the data sets was 50 (length) units, and the distance between the points in each dataset was 0.5. The number of data sets combined ranged from 1 to 100. Figure 3.7 shows how the estimation of the scale of fluctuation is affected by the number of data sets used.

In Figure 3.7, each black point is an estimate of the SoF (relative to the input SoF) as a function of the number of data sets (e.g. CPT profiles) used in the estimation, where, for each number of data sets considered, 100 estimates of the SoF have been made. Hence, in a site investigation a single black dot would be the result calculated, based on, for example, combining the data from all available CPT profiles. The horizontal blue line is the normalised input SoF and is the theoretical solution, whereas the red line is the average of the 100 estimations, and the green line is the CoV (σ/μ i.e. mean / standard deviation) of the estimations of the SoF; hence, as the CoV reduces the likelihood of achieving a good result increases. While there are some minor differences between individual estimates (the black dots in Figure 3.7) obtained using the NDFT and direct experimental auto-correlation functions, the two approaches behave similarly, with the NDFT performing slightly better. In both cases, as expected, if more data sets are used for the estimation of the scale of fluctuation, the result is more likely to be accurate. In this example, when considering only 1 dataset there is a 9.6% chance of being within 20% of the real scale of fluctuation, whereas there is a 33.1% chance of being within 20% when 5 data sets are used, rising to 70.0% with 100 data sets. This increase in accuracy is offset by an increase in computational effort for the analysis and in additional expense in collecting the extra data. Figure 3.7 also shows that using a limited amount of data is more likely to result in an overestimate of θ; this is because, as the theoretical auto-correlation is always positive, positive values of the experimental auto-correlation function have a larger influence on the error estimation than negative values.

The number of data points per dataset has also been investigated. This was done by again using a distance of 0.5 between data points, and considering overall domain lengths to change with the number of data points. The generated data, once again, had a mean of 0, a standard deviation of 1, and a Markov auto-correlation structure with $\theta = 5$. For each number of data points considered, 100 estimates of the SoF, each using 40 data sets have been produced. Again, as expected, by increasing the number of points the estimation of the SoF improved (see Figure 3.8). Also, there is once again little difference between the two methods. Considering only 5 data points per dataset there is a 27.9% chance of being within 20% of the real scale of fluctuation, whereas with 10 data points there is a 33.5% chance of being within 20%, rising to 71.9% with 100 data points.

Using a fixed domain size (length) of 50 and the same number of data points, the ability to detect different values of SoF was then investigated. This was based on 100

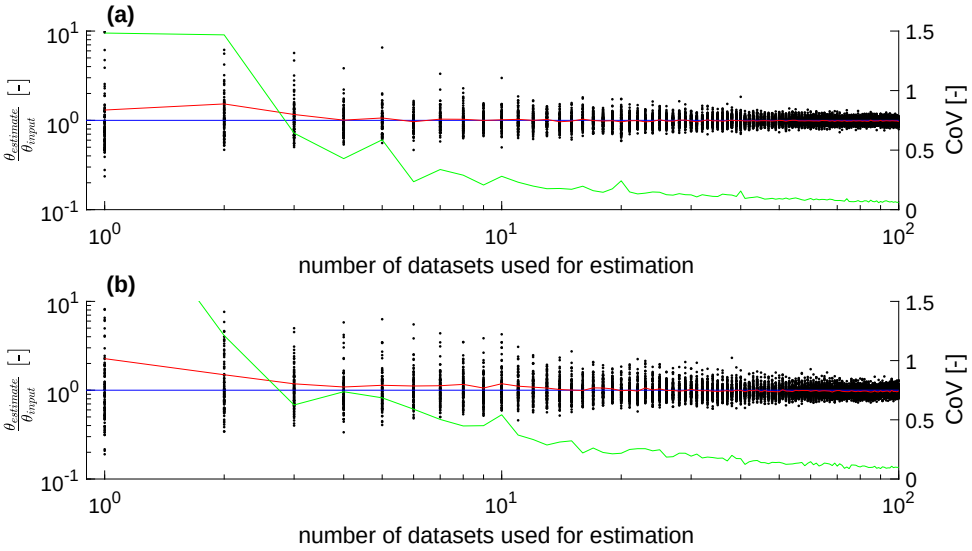

Figure 3.7: Accuracy of SoF estimation as a function of the number of data sets. (a) θ via NDFT, and (b) θ directly from the auto-correlation function. Each black dot is a single example, the blue line is the true result, the red line is the average result from the investigation undertaken and used to estimate the auto-correlation function, the green line is the CoV of the SoF estimates.

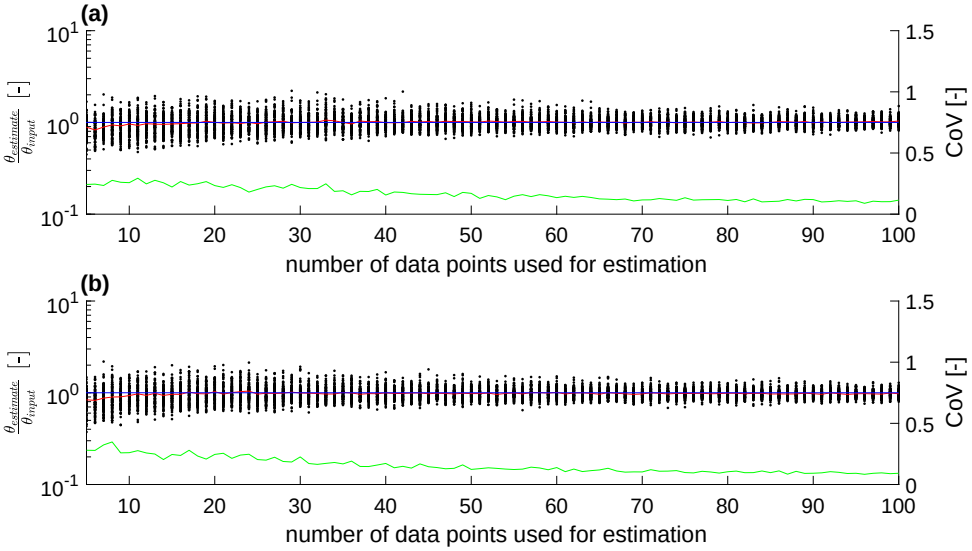

Figure 3.8: Accuracy of SoF estimation as a function of the number of points in the dataset. (a) θ via NDFT, and (b) θ directly from the auto-correlation function. The separation distance of the points is constant, i.e. the domain increases as more points are considered. Each black dot is a single example, the blue line is the true result, the red line is the average result, and the green line is the CoV of the SoF estimates.

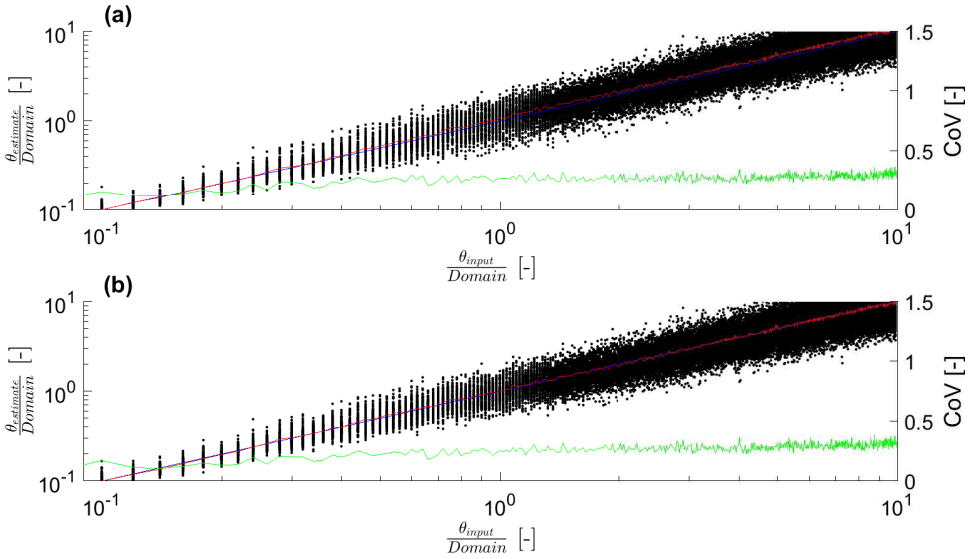

Figure 3.9: Accuracy of SoF estimation as a function of actual SoF relative to domain size, based on 40 data sets. (a) θ via NDFT, and (b) θ directly from the auto-correlation function. Each black dot is a single example, the blue line is the true result, the red line is the average result and the green line is the CoV of the SoF estimates.

estimates of the SoF, each using 100 points per dataset and 40 data sets. The generated data, once again, had a mean of 0, a standard deviation of 1, and a Markov auto-correlation structure, but now with the input SoF varying between $\theta = 5$ and $\theta = 500$. Figure 3.9 shows how the estimated scale of fluctuation changes, when the input SoF is varied between 0.1 times the domain length ($\theta = 5$) to 10 times the domain length ($\theta = 500$). Considering an input SoF of only 0.1 times the domain length there is a 44.2% chance of the estimated SoF being within 20% of the real scale of fluctuation, whereas for an input SoF equal to the domain length there is a 33.3% chance of being within 20%, decreasing to 26.04% when it is 10 times the domain length. However, Figure 3.9 shows that estimating scales of fluctuation is possible, even when the real SoF is five times larger than the domain length.

As the scale of fluctuation increases relative to the domain size, the coefficient of variation of the estimated SoF also increases, although the CoV increases at a much lower rate when the SoF is larger than the domain size. In Figure 3.9, the CoV increases from 0.05 to 0.2 when θ is smaller than the domain size, whereas, for θ larger than the domain size, the CoV varies in the range 0.2 – 0.35.

3.3.2. UNEQUALLY SPACED DATA

In reality, it may be difficult to obtain equally spaced data, especially for estimating the horizontal SoF. By using Equation (3.6) rather than Equation (3.5) the direct auto-correlation function can be obtained. The NDFT, Equations (3.7-3.9), can be used with uneven data provided the correction from a biased to an unbiased estimate is made. Figure 3.10 illustrates the estimation of θ obtained from non-uniform sampling. In this

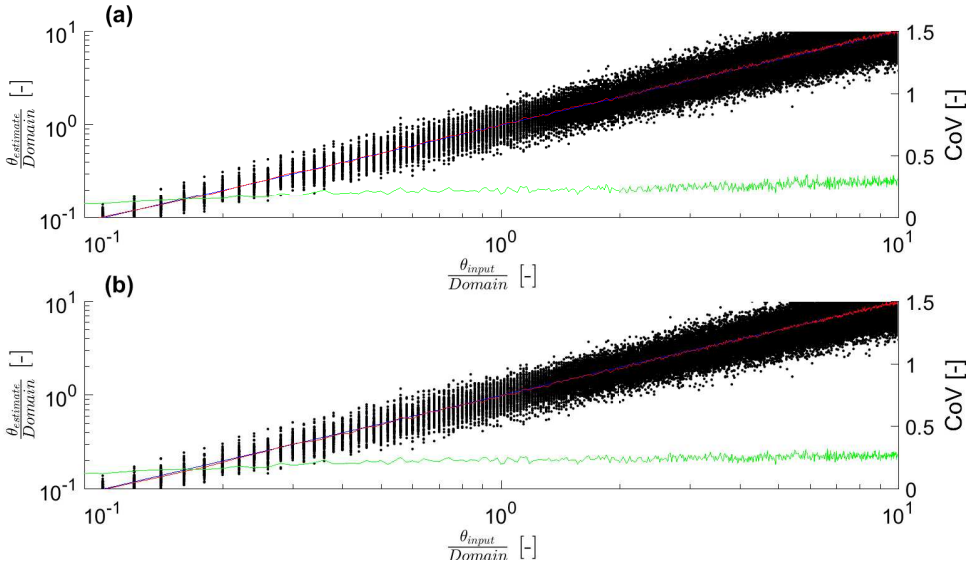

Figure 3.10: Accuracy of SoF estimation as a function of increasing SoF based on 40 data sets, a fixed domain length of 50, and uneven spacing: 6 x 2.5 intervals, followed by 16 x 1.25 intervals and then 6 x 2.5 intervals. (a) θ via NDFT, and (b) θ directly from auto correlation function. Each black dot is a single example, the blue line is the true result, the red line is the average result, and the green line is the CoV of the SoF estimates.

case, the non-uniform sampling regime is based on the site investigation reported later in the chapter (Figure 3.19); that is, data points at 6 intervals of 2.5, followed by sixteen intervals of 1.25, and ending with 6 intervals of 2.5, totalling 29 points generated at non uniform spacings over a total distance of 50.

Comparing Figures 3.9 and 3.10, there is little difference between the results based on uniformly distributed points and those based on unequally spaced data.

Hence, from the results obtained for the three different scenarios (Figures 3.7 to 3.9) it is apparent that the CoV, and thereby the reliability of the estimate, is mainly dependent on the number of data sets and the number of points per dataset. In order to estimate the reliability of a calculated SoF, several values of SoF relative to domain size (0.1, 0.5, 1.0, 5.0, 10.0) and of SoF relative to distance between data points (10, 50, 100, 200), for different numbers of data sets and points per dataset, have been investigated. By using a minimum error approach on the obtained CoV values, a theoretical estimate for the CoV of SoF is proposed in this thesis and found to describe the CoV of SoF well, i.e.

$$CoV = 1.1 \times W \times X \times Y + Z \tag{3.16}$$

where W is a factor which changes fastest when θ is smaller than the domain size (D), given by

$$W = tan^{-1}\left(\frac{5\theta}{D}\right) \tag{3.17}$$

X is a factor that considers the number of independent datastets,

$$X = \frac{1}{\sqrt{nf}} \tag{3.18}$$

where the number of independent data sets that can be estimated using

$$nf = \begin{cases} \frac{D_p}{\theta_p} & ; D_p > \theta_p \\ 1 & ; D_p \leq \theta_p \end{cases} \tag{3.19}$$

whereas Y is a factor that accounts for spacing between the data points,

$$Y = \left(1 + \frac{in}{\theta}\right) \tag{3.20}$$

and Z a factor that dominates when θ is larger than D,

$$Z = \frac{\theta}{5nfD} \tag{3.21}$$

where θ is the scale of fluctuation, D is the domain length, nf is the number of data sets (with a minimum of 1) , and in is the interval between the data points.

Hence, Equation (3.16) identifies four factors that affect the estimate of CoV: (1) a factor for $\theta < D$, if the domain length is large compared to the SoF, CoV is reduced; (2) a factor for the number of (independent) data sets, as the number of data sets increases, CoV decreases. The number of independent data sets can be estimated based on the size of the perpendicular scale of fluctuation (θ_p) compared to the perpendicular domain (D_p), e.g. a $\theta_p = 0.25$ with $D_p = 4$ leads to $nf = 16$; (3) a factor for the spacing of data, if the interval between points is large compared to SoF, CoV increases; (4) factor for $\theta > D$, if the domain is short compared to SoF, CoV increases. Note that, in all cases the CoV decreases with an increase in number of data sets.

Figure 3.11(a-f) shows the expected (i.e. calculated from generated data) and theoretical (i.e. calculated using Equation (3.16)) CoVs of θ, as functions of the number of data points, size of domain, spacing of data points, and number of data sets (e.g. CPTs). Two groups of analyses have been examined: (1) the number of data points is varied between 2 and 101, for a fixed spacing of 0.5 (hence, the domain size varies between 0.5 and 50); (2) the domain is kept constant at 50 and, by varying the number of data points, the sampling spacing changes. By inspecting the results for the different SoFs (5, 25 and 250), shown in Figure 3.11(a-d) for approach (1) and in Figure 3.11(e-f) for approach (2), it is seen that the estimated CoV from Equation (3.16) captures the different aspects of the calculated CoV using generated data.

To estimate the CoV for either the vertical or horizontal scale of fluctuation using CPT data, Equation (3.16) can be used. It should be noted that, for estimating the vertical scale of fluctuation, there are generally many points per CPT, though often relatively few CPTs, so the estimations in the top left corners of the graphs in Figure 3.11 are representative. For estimating the horizontal scale of fluctuation there are fewer data points, although each depth interval for the group of CPTs can be considered as a different dataset. Hence, there can be a large number of data sets comprising relatively few data points, so that the estimation in the bottom right corner of the graphs is applicable.

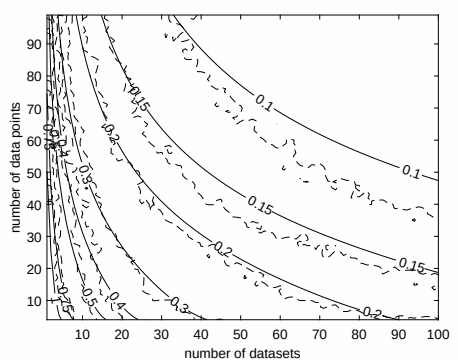

(a) θ = 5 in = 0.5, D varies

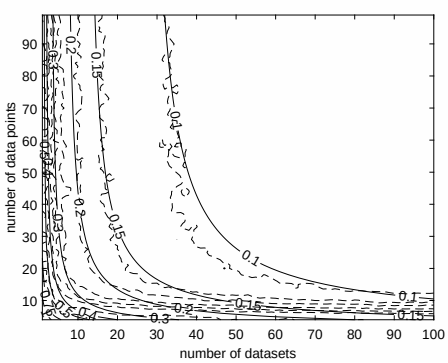

(d) θ = 5, in varies, D = 50

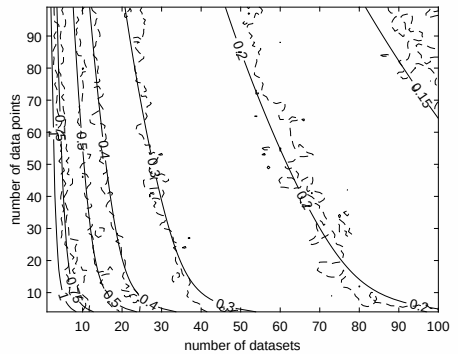

(b) θ = 25, in = 0.5, D varies

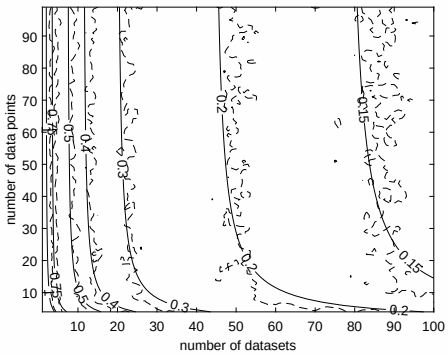

(e) θ = 25, in varies, D = 50

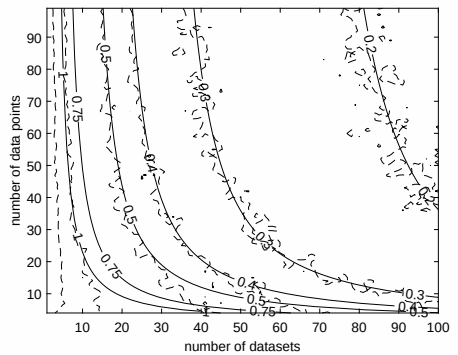

(c) θ = 250, in = 0.5, D varies

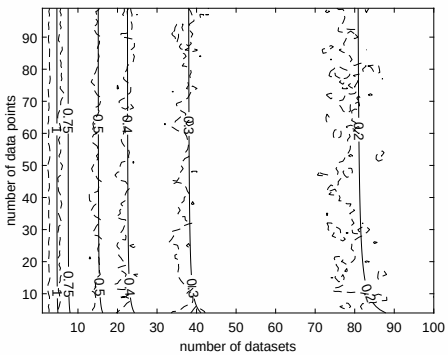

(f) θ = 250, in varies, D = 50

Figure 3.11: Calculated and theoretical isochrones of CoV of θ, as a function domain size, interval size, θ and number of CPTs (fields). For graphs (a-c) the interval between the points is fixed (0.5) and, as the number of points increases, the domain size also increases. For graphs (d-f) the domain size is fixed at 50 and, as the number of points increases, the interval between the points decreases.

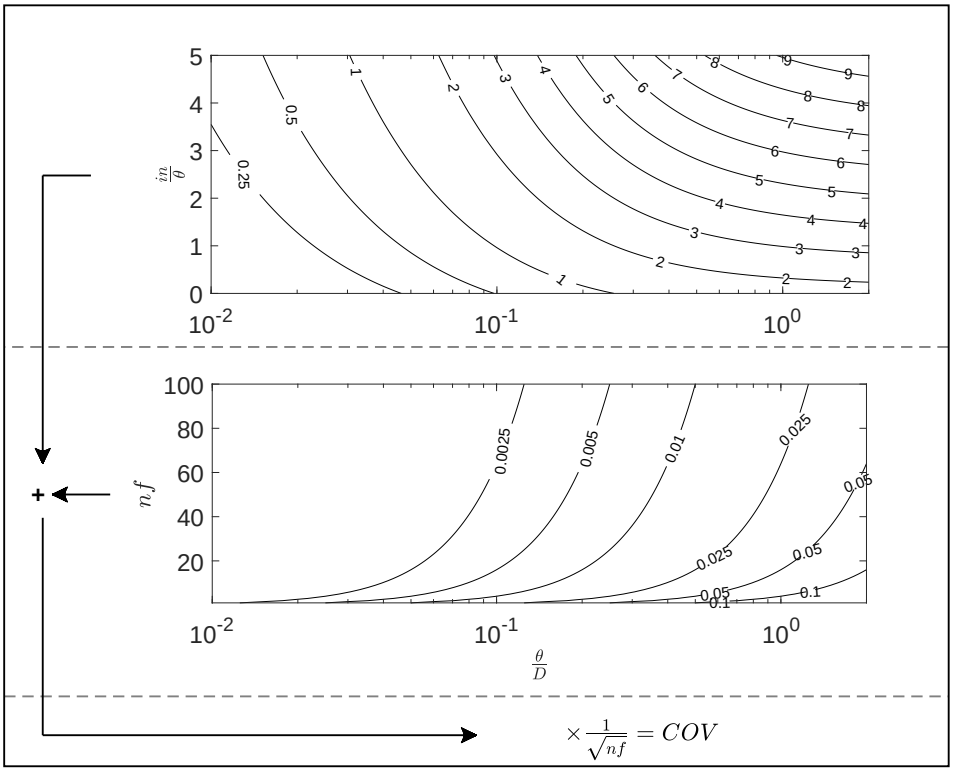

θ = Scale of fluctuation; D = Domain size; nf = Number of independent data sets; in = Interval between data points

Figure 3.12: Estimating CoV for equally spaced vertical and horizontal data, based on the interval between data points, scale of fluctuation, domain size and number of data sets.

The CoV estimation from Equation (3.16) has been summarised in the design chart shown in Figure 3.12. This chart can be used in practice to estimate the uncertainty in calculated values of θ. θ must first be calculated (or estimated, if used prior to a site investigation), and then information on the size of the dataset is used. As an example, a series of 10 vertical CPTs (with a vertical data interval of 0.01 m) and a vertical domain of 5 m is considered. They are arranged in a single line and horizontally spaced at 2.5 m, making a horizontal domain length of 22.5 m; the estimate of θ_v is 0.25 m and θ_h is estimated to be 5 m. Considering the CoV of θ_v, the first part of the figure gives a value of 0.29 and the second part of the figure gives a value below 0.005; adding these numbers together gives 0.295. The nf here is defined by nf_{max} as 22.5/5 = 4.5 and the estimated CoV of θ_v is then 0.14 m. Considering θ_h, the first part of the figure gives a value of 1.4 and the second part gives a value below 0.02; adding these numbers together gives 1.42. Once again nf is defined by nf_{max}, which is equal to 5/0.25 = 20, and gives an estimated CoV of θ_h of 0.32.

As mentioned above, to estimate the horizontal SoF it is unlikely that a large amount of data per dataset are available. Moreover, the horizontal SoF may range from 0-5 m to 100 m. It is therefore important to investigate the estimation with different sampling techniques. For this purpose, eight data points per dataset have been used, equivalent to eight CPTs arranged in a single line. In this test, the 8 data points (or CPTs) have been arranged in different groups with a 0.5 horizontal spacing within any group. The interval between each group has been increased in steps, and the CoV of the estimated scale of fluctuation has been computed as a function of the number of data sets of 8 points (with the number of data sets being proportioned to the depth of a layer). An investigation into the effect of different group sizes has also been undertaken.

Figures 3.13 to 3.15 present the CoV for three sampling strategies to calculate the spatial auto-correlation with eight points (e.g. eight CPTs to determine the horizontal SoF) arranged into groups. The interval between the groups is increased in steps, starting from 0.5 (equal to the spacing within each group). The three strategies are: (1) four groups of two points separated by three intervals; (2) two groups of three points and one group of two points with two intervals; (3) two groups of four points with one interval. For each strategy, three values of θ have been considered (θ = 5, 25 and 50). In Figures 3.13 to 3.15 (a-c) the calculated CoV based on the generated data is shown, and at the top of each figure the sampling strategy is shown schematically.

Figure 3.13 analyses the CoV of four pairs of CPTs separated by three intervals, with the intervals ranging from 0.5 to 12. The trends in the calculated CoV change with the value of SoF. For θ= 5, the CoV increases as the interval increases when the interval is greater than 7 and the data points are too far apart to improve the estimation. For θ= 25 and 50, when using a small interval (and thus small domain) the CoV only increases when only a few data sets are considered, suggesting that both small and large θ can be reasonably estimated using pairs of closely spaced CPTs. Figure 3.14 shows that the CoV based on three groups, with two up to 21.5 units in length, with similar behaviour being observed as with four groups of two data points (Figure 3.13). Figure 3.15 shows that, for two groups and one interval up to 43.5 units in length, for θ= 5, 25 and 50 the calculated CoV increases as the interval approaches and exceeds θ. In order to account for estimating the CoV of SoF when considering groups of data points, Equation (3.16) proposed in this thesis, has been updated to give

$$CoV = 1.1 \times W \times X \times Y + Z \tag{3.22}$$

where W is the factor when θ is smaller than the size of a group (D_g)

$$W = tan^{-1}\left(\frac{5\theta}{D_g}\right) \tag{3.23}$$

X considers the number of independent datastets

$$X = \frac{1}{\sqrt{nf}} \tag{3.24}$$

Y accounts for the spacing between the data sets

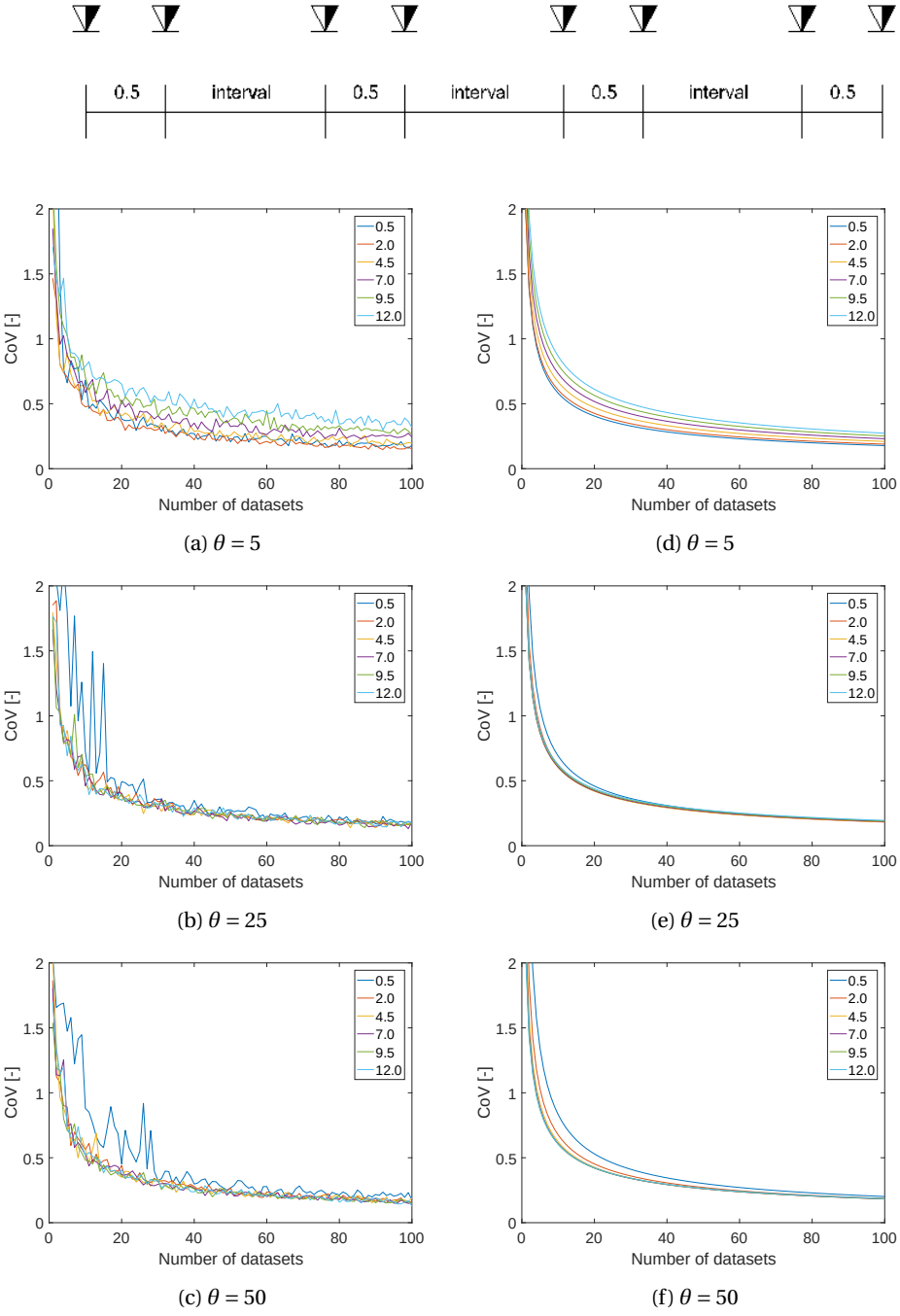

(a) $\theta = 5$ (d) $\theta = 5$

(b) $\theta = 25$ (e) $\theta = 25$

(c) $\theta = 50$ (f) $\theta = 50$

Figure 3.13: Analysis of CoV results for eight data points grouped as 4 groups of two. Within the groups the spacing of the points is 0.5. (a-c) shows results for the three scales of fluctuation considered (5, 25 and 50). In each graph the interval between the groups is increased in steps. (d-f) shows the equivalent theoretical CoV curves according to Equation (3.22).

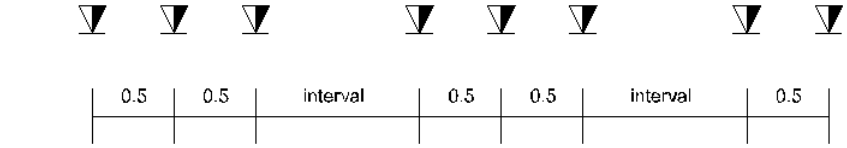

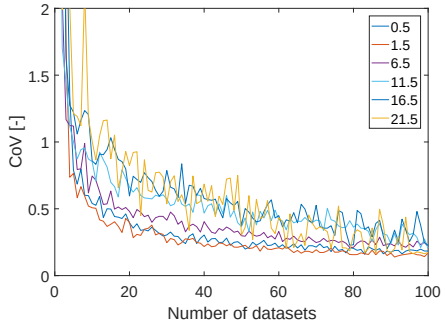

(a) $\theta = 5$

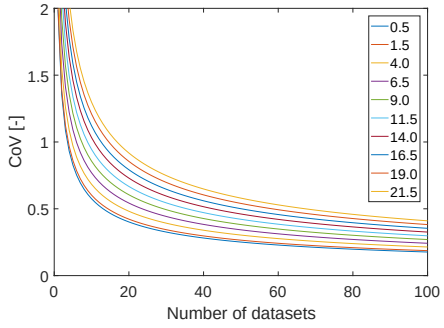

(d) $\theta = 5$

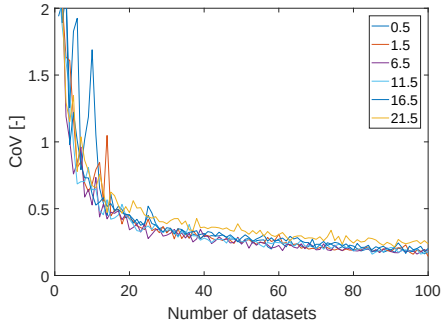

(b) $\theta = 25$

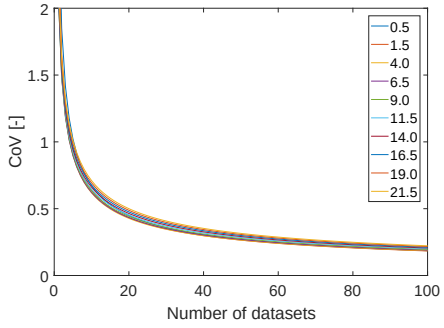

(e) $\theta = 25$

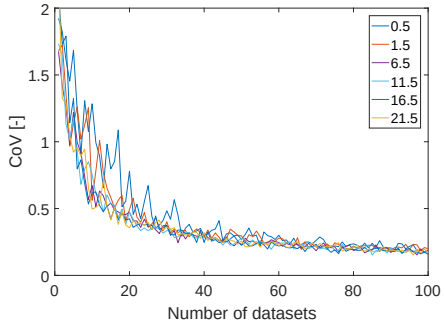

(c) $\theta = 50$

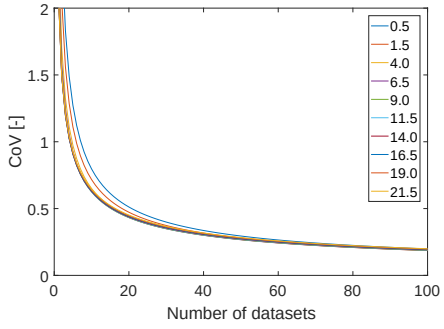

(f) $\theta = 50$

Figure 3.14: Analysis of CoV results for eight data points grouped as two groups of three and one group of two. Within the groups the spacing of the points is 0.5. (a-c) shows results for the three scales of fluctuation considered (5, 25 and 50). In each graph the interval between the groups is increased in steps. (d-f) shows the equivalent theoretical CoV curves according to Equation (3.22).

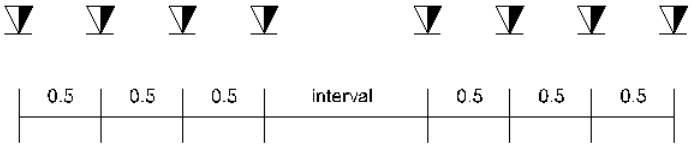

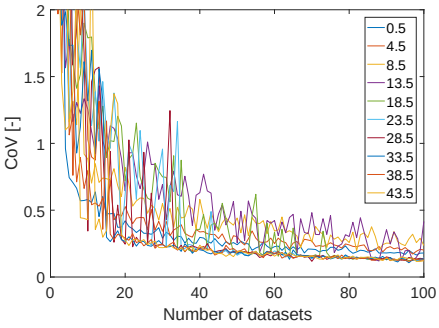

(a) $\theta = 5$

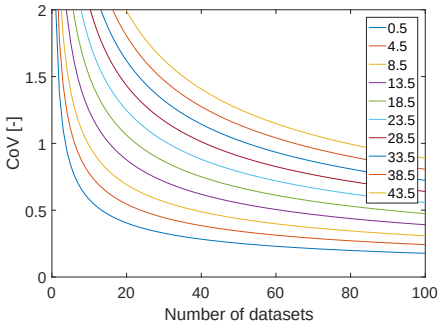

(d) $\theta = 5$

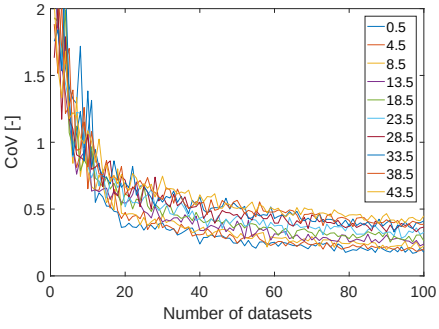

(b) $\theta = 25$

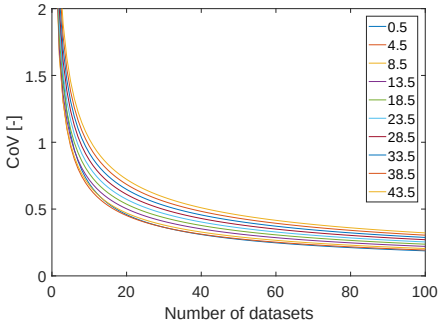

(e) $\theta = 25$

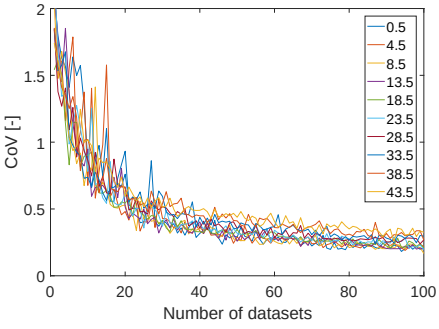

(c) $\theta = 50$

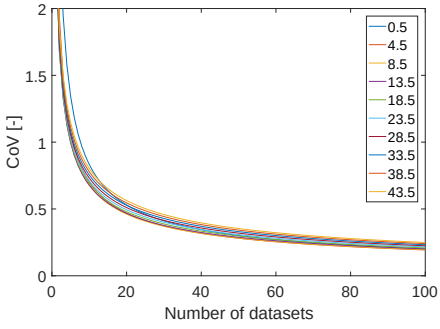

(f) $\theta = 50$

Figure 3.15: Analysis of CoV results for eight data points grouped as two groups of four. Within the groups the spacing of the points is 0.5. (a-c) shows results for the three scales of fluctuation considered (5, 25 and 50). In each graph the interval between the groups is increased in steps. (d-f) shows the equivalent theoretical CoV curves according to Equation (3.22).

$$Y = \left(1 + \frac{in}{ng \times \theta}\right) \tag{3.25}$$

and Z is the factor when θ is larger than the total domain (D_t)

$$Z = \frac{\theta}{5nf \times D_t} \tag{3.26}$$

where the number of independent data sets can be estimate using

$$nf = \begin{cases} \frac{D_p}{\theta_p} & ; D_p > \theta_p \\ 1 & ; D_p \leq \theta_p \end{cases} \tag{3.27}$$

in which ng is the number of groups (if the data have different intervals), D_t is the total domain length over which the data points are obtained and D_g is the domain length of the individual groups.

In this example, the CoV was estimated using an auto-correlation function based on eight data points. Figures 3.13(d-f) to 3.15 (d-f) show the theoretical approximation based on Equation (3.22), revealing that Equation (3.22) captures well the CoV variation with different intervals between groups. For θ = 25 and 50, an interval of only 0.5 causes a high CoV because the domain length (D_t) is short compared to θ in all figures; however, as the number of independent data sets increases the calculated CoV reduces. For three groups of data and two intervals (Figure 3.14), the calculated CoV for θ = 5 and 25 increases as the interval increases, although this is not the case for an SoF of 50. With only one interval (Figure 3.15) and θ= 5, the estimated CoV of θ is greatly influenced by the interval size, whereas for θ= 25 and 50 they are similar. The increase in CoV when considering a large interval compared to θ is caused by the shape of the experimental auto-correlation function and minimising of the error. Over the interval there are no data to compare, which causes a gap in the experimental auto-correlation function. In estimating the scale of fluctuation with an interval gap in the experimental auto-correlation function, the first point after the interval has a disproportionate influence on the estimated SoF.

Figure 3.16 presents an investigation of how the estimate of a double scale of fluctuation behaves with an interval shorter than the larger scale of fluctuation and longer than the smaller scale of fluctuation. A double SoF based on θ_1= 5, c_1 = 0.75 and θ_2= 25, c_2 = 0.25 was generated and analysed. In this case, the interval of 14.5 is larger than the smaller scale of fluctuation (θ_1=5) and shorter than the larger scale of fluctuation (θ_2=25). Figure 3.16(b) shows that the results for the individual scales of fluctuation are relatively poorly calculated (high CoV), whereas the estimate for the combined (averaged) scale of fluctuation is better (low CoV). Figure 3.16(a) shows that the mean of θ_1 is underestimated and that the mean of θ_2 has a large fluctuation around the correct solution. Whereas the calculated CoVs for θ_1 and θ_2 do not match Equation (3.22), the calculated CoV for θ_{avg} is similar to Equation (3.22).

The CoV estimation from Equation (3.22) can be done graphically using Figure 3.17, once the scale of fluctuation has been calculated. The interval is known, the domain size is known and the number of fields (or CPTs) is known. For example, using Figure 3.17 and considering, as an example, 10 CPTs grouped in 5 groups of 2, separated by 2.5 m within each group and with an interval between the groups of 25 m, the total domain

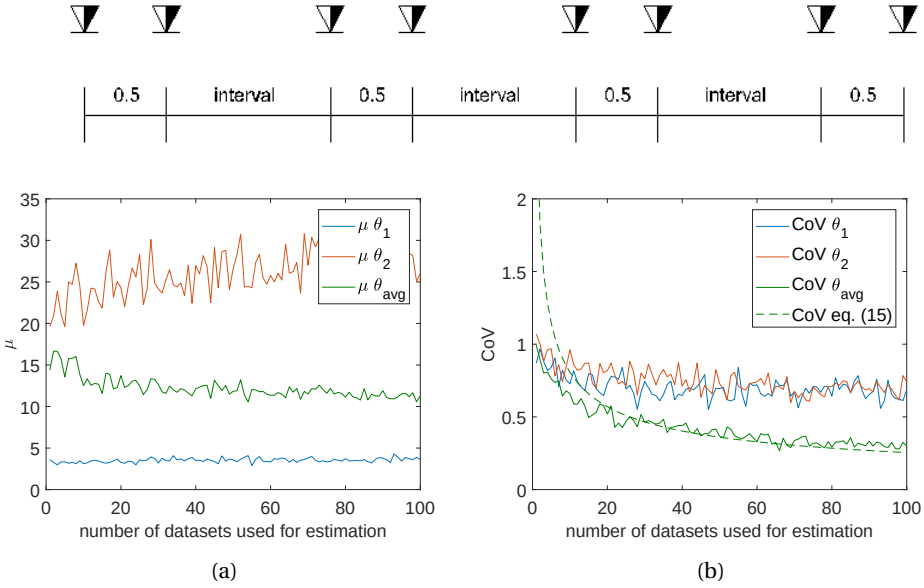

(a) (b)

Figure 3.16: Investigation using 4 groups of data points, three 14.5 intervals and a double SoF given by $\theta_1 = 5$, $c_1 = 0.75$ and $\theta_2 = 25$, $c_2 = 0.25$. (a) the mean of the two different SoFs and their weighted average are shown, (b) the CoV of the weighted average and the two different SoFs are shown, along with the prediction using Equation (3.22).

size is 112.5 m. If the horizontal scale of fluctuation is estimated to be 5 m, the first part of the figure gives a value of 3.2 and the second part of the figure gives a value below 0.005; adding these values together gives 3.205, and dividing by the square root of 500 (the number of data intervals) yields an estimated CoV of 0.14.

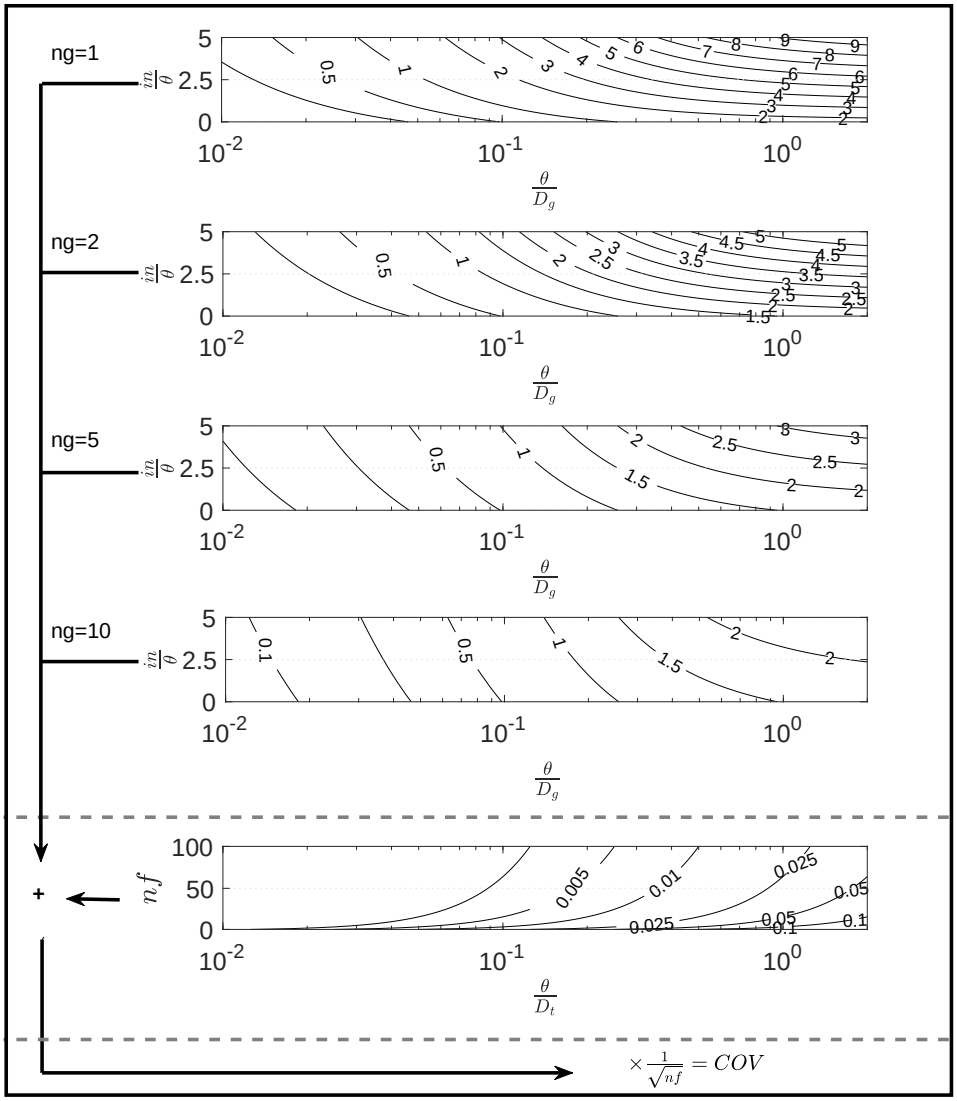

θ = Scale of fluctuation; D_g = Size of a group; nf = Number of data sets;
in = Interval between groups; D_t = Total domain size

Figure 3.17: Estimating CoV of θ for horizontally grouped data, based on interval between groups, scale of fluctuation, size of a group, size of the total domain and number of data sets.

3.4. INVESTIGATION USING REAL DATA

Both the direct auto-correlation function and NDFT methods have been shown able to estimate scales of fluctuation and are now tested in a real situation. Specifically, the performance of the methodology is demonstrated for limited data, that is irregularly sampled, from a 2D cross-section at Leendert de Boerspolder.

The dataset was collected to investigate the vertical and horizontal heterogeneity. It was taken over an area of 50x15 m in the immediate vicinity of a small dyke (see Chapter 2), and comprised 100 CPTs that were obtained over a two week period by two different CPT-cones (calibrated before testing), CPT-rig and CPT opperator. Figure 3.18 shows that the grid of CPTs was constructed in such a way that the spatial variation could be obtained in different directions for a range of sampling densities.

Figure 3.19 shows the CPT data corresponding to the crest in Figure 3.18, this being the line with the smallest CPT spacing. Along this line, a total of 29 CPTs were recorded along the crest of the dyke over a 50 m reach; specifically, 6 CPTs were taken at 2.5 m intervals, followed by 16 at 1.25 m intervals, and then another 6 at 2.5 m intervals. The subsurface consists of a man-made and subsequently maintained dyke body, composed of silts, clays, sands and some rubble. This lies on top of a peat layer underlain by a clay layer consisting of two clay types, an organic clay and a silty clay, followed by another peat layer (not found at the location of the induced failure) underlain by a sand layer. In the following analysis the first three layers have been analysed (dyke material, peat and clay).

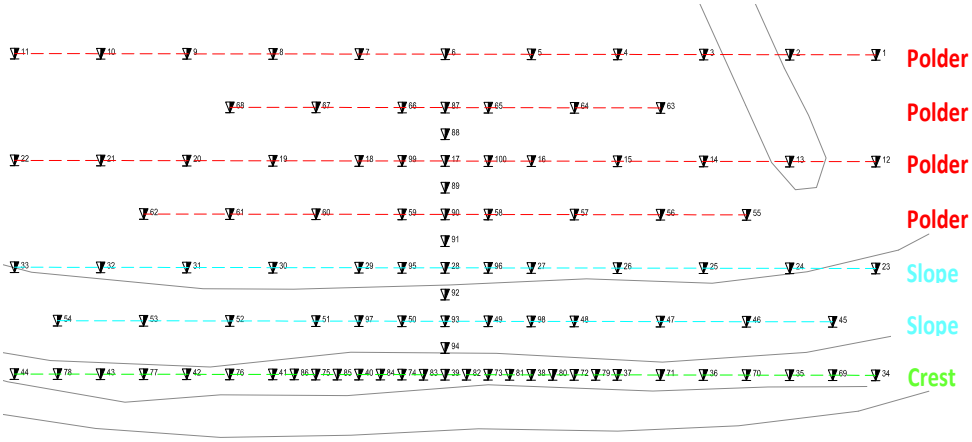

Figure 3.18: 100 CPTs over an irregular grid, over the dyke, to capture the spatial variation in both the horizontal and vertical directions.

Both the vertical and horizontal scales of fluctuation have been determined. Due to deposition history, it is generally assumed that the horizontal scale of fluctuation is larger than the vertical scale of fluctuation, so the larger spacing of data in the horizontal plane was anticipated to be acceptable.

Figure 3.20 shows the different steps in analysing the CPT data for the dyke material, specifically: (a) removing the linear trend if present, obtaining a mean of zero and then normalising the standard deviation to 1; (b) and (e) the vertical and horizontal

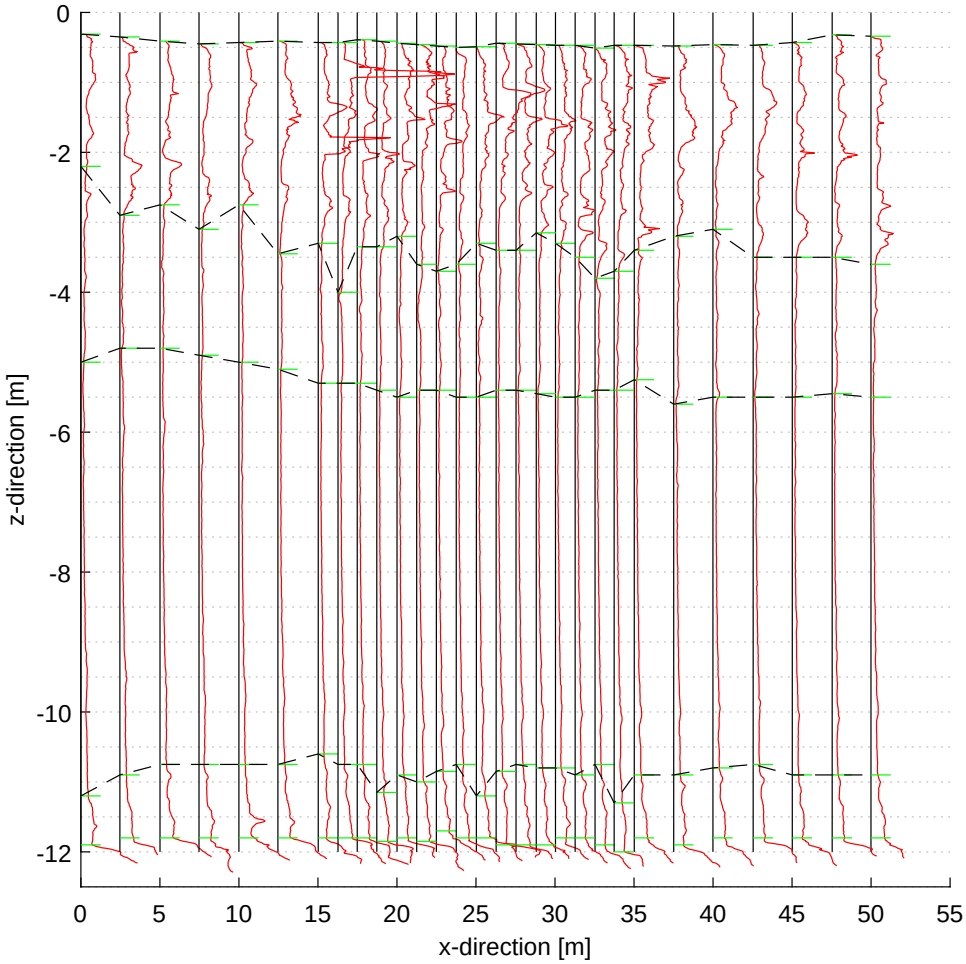

Figure 3.19: 29 non-uniformly spaced CPT profiles along the dyke crest. The solid vertical black lines indicate the locations of the CPTs, the red lines are the normalised tip resistance, q_t, the horizontal green markers indicate the identified layer boundaries in each CPT, and the broken black lines indicate the layer boundaries over the cross-section. note that the scales are unequal in different directions.

experimental auto-correlations are shown, including the theoretical auto-correlation functions; (c) indicates the type of distribution before and after detrending; (d) shows the numeric values of the analysis.

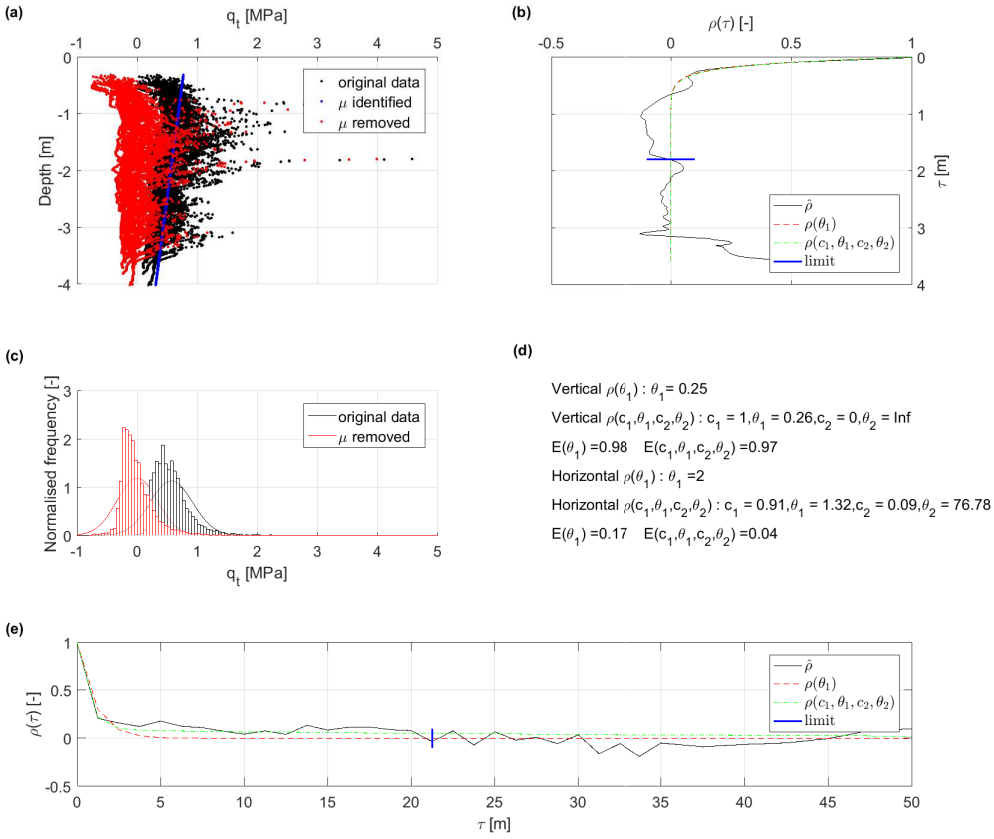

Figure 3.20: Analysis of CPT data for the dyke material, (a): raw and de-trended data from which the spatial auto-correlation is estimated, (b): two estimates of the vertical spatial auto-correlation, (c): histogram and probability density function of original data and data with mean trend removed, (d): theoretical estimates of scales of fluctuation and their corresponding errors, (e): horizontal spatial auto-correlation.

Table 3.3 presents a summary of the data analysis, comprising the functions of the mean trend, the standard deviation of the de-trended data, the estimate of a single scale of fluctuation, the estimate of the scale of fluctuation assuming a double scale of fluctuation, the amount of data used in the error calculation, the amount of data used in the estimate of CoV using Equation (3.16) and the resulting estimate of CoV.

The dyke material and peat exhibit linear mean trends that have been removed before analysing the data. In contrast, the clay exhibits a quadratic trend, probably due to the change in the composition of the clay material with depth. In two of the three calculated vertical scales of fluctuation (i.e. those for the dyke material and peat layer),

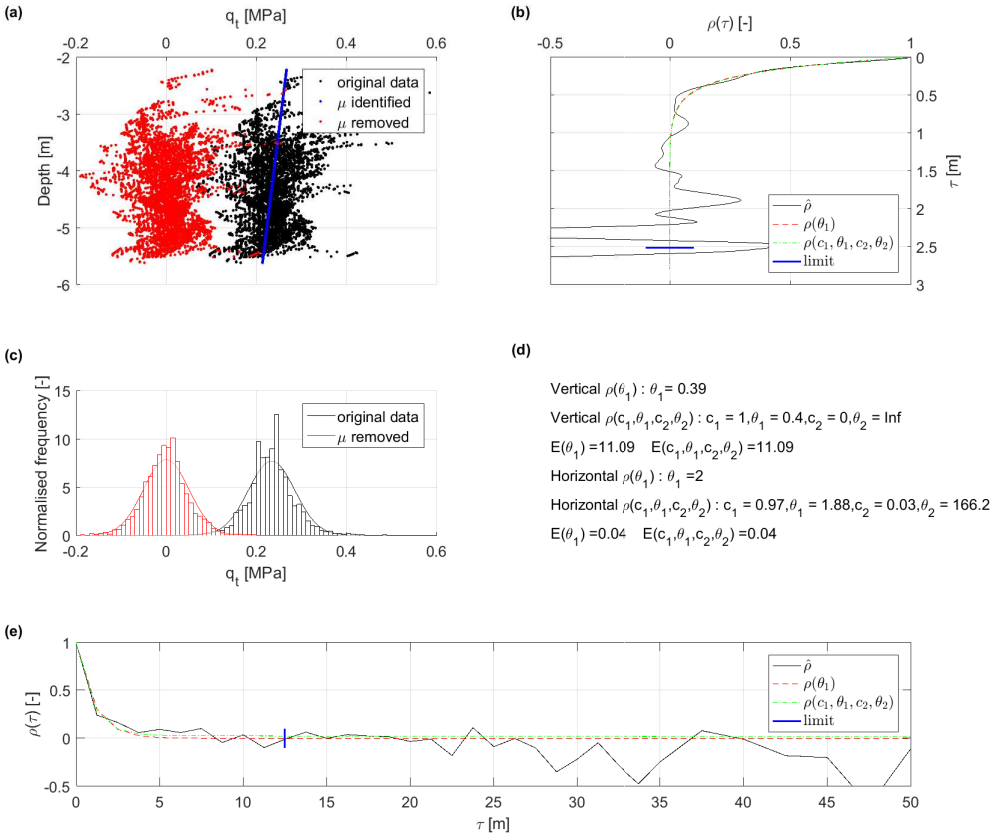

Figure 3.21: Analysis of CPT data for the peat layer, (a): raw and de-trended data from which the spatial auto-correlation is estimated, (b): two estimates of the vertical spatial auto-correlation, (c): histogram and probability density function of original data and data with mean trend removed, (d): theoretical estimates of scales of fluctuation and their corresponding errors, (e): horizontal spatial auto-correlation.

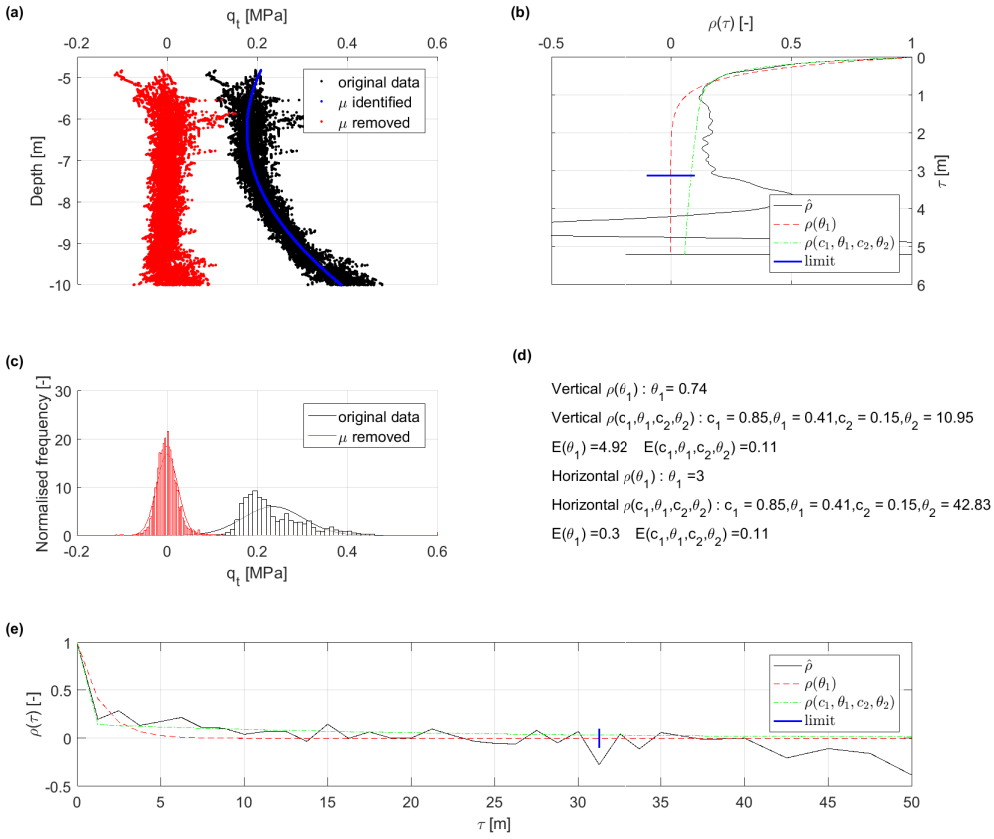

Figure 3.22: Analysis of CPT data, for the clay layer, (a): raw and de-trended data from which the spatial auto-correlation is estimated, (b): two estimates of the vertical spatial auto-correlation, (c): histogram and probability density function of original data and data with mean trend removed, (d): theoretical estimates of scales of fluctuation and their corresponding errors, (e): horizontal spatial auto-correlation.

Table 3.3: Summary of analysis real data

Linear trend and standard deviation		
	μ [MPa]	σ [MPa]
Dyke material	$0.8081 + 0.1244z$	0.3346
Peat	$0.3018 + 0.0157z$	0.0505
Clay	$0.7592 + 0.1863z + 0.0149z^2$	0.0234

Vertical estimates						
	θ_{avg} [m]	c_1, θ_1 c_2, θ_2 [-], [m]	Percentage of data used [%]	Error for 1θ Error for 2θ [-]	no. of points no. of data sets [-]	CoV single CoV double* [-]
Dyke material	0.25	1, 0.25	50	0.98	291	0.13
		0, ∞	50	0.98	29	0.13
Peat	0.39	1.0, 0.39	90	11.09	200	0.15
		0, ∞	90	11.09	29	0.15
Clay	0.74	0.85, 0.41	50	4.92	467	0.20
		0.15, 10.95	50	0.11	29	0.28

Horizontal estimates						
	θ_{avg} [m]	c_1, θ_1 c_2, θ_2 [-], [m]	Percentage of data used [%]	Error for 1θ Error for 2θ [-]	no. of points no. of data sets [-]	CoV single CoV double* [-]
Dyke material	2.0	0.91, 1.32	50	0.17	29	0.04
		0.09, 76.78	50	0.04	291	0.07
Peat	2.0	0.97, 1.88	30	0.04	29	0.06
		0.03, 166.2	30	0.04	200	0.09
Clay	0.74	0.85, 0.41	50	4.92	467	0.20
		0.15, 10.95	50	0.11	29	0.28

only a negligible difference is observed when a second scale of fluctuation is introduced, as indicated by the identical error. However, when looking at the horizontal scale of fluctuation, in two cases a second scale of fluctuation reduces the error significantly. In all cases, the main component of the horizontal scale of fluctuation is the smaller of the two scales.

The percentages of data used to calculate the error are influenced by the erratic behaviour of the experimental auto-correlation function. When determining the extent of the auto-correlation function to be considered, a visual inspection is used, bearing in mind that when the auto-correlation function is built at larger lag lengths, fewer pairs of data are included and the function becomes less reliable. The percentage of data used are reported in Table 3.3. In Figures 3.20(e)-3.22(e),the extent of the data used is indicated by the blue vertical line.

The expected CoV of θ in Table 3.3 is obtained from Equation (3.16). For the estimation of the CoV for the vertical scale of fluctuation, the number of data sets is equal to the number of CPTs and the number of points is the average number of data points per CPT. For the horizontal plane, the number of data sets is the number of depth intervals considered, whereas the number of data points is the number of CPTs. For the CoV of θ in the horizontal plane, based on two SoFs, θ_{avg} is used in Equation (3.16). In all cases, the CoVs for the double SoF cases are equal to or greater than those for the single SoF cases, although the error is in most cases significantly lower.

In the analysis of this site it can be concluded that the SoF is larger in the horizontal plane than in the vertical direction for all layers, and is therefore in agreement with the view that geological processes (in sediments) cause a horizontal auto-correlation that is larger than the vertical auto-correlation. There has been mention of the possibility of a double SoF by Vanmarcke *et al.* (1986), although neither the identification nor use of a double SoF is evident in literature. A double SoF can have different explanations: (1) it is caused by geological processes that operate on different scales; (2) it is caused by a weak spatial auto-correlation of the material properties and/or a large amount of noise; or (3) it is the product of the removal of a wrong trend. Introducing a double SoF into an analysis may change the computed response of some geotechnical structures, although the extent to which the response is influenced by a double SoF depends on the type of structure involved.

Comparing Table 3.1 and Table 3.3 the values of the vertical scales of fluctuation have a similar range. however, the range for the horizontal scale of fluctuation is at the low end of the scales of fluctuation found by other authors. The relatively small horizontal scales of fluctuation are likely to be due to the maintenance of the dyke that historically was done in small sections. de Gast *et al.* (2019) shows a significant shift to larger scales of fluctuation (up to 20 m) as the scales of fluctuation further away from the dyke body were being observed, which is in line with the larger ranges of horizontal scales of fluctuation described in Table 3.1.

3.5. DISCUSSION

Both horizontal and vertical scales of fluctuation can be measured from a series of vertical CPT soundings. However, many datapoints are seen to be required for a reliable analysis of both the horizontal and vertical scales of fluctuation. This can be from few CPT soundings

in thick layers (e.g. Ching *et al.*, 2018) or from many CPT soundings in thinner layers.

The method presented in this chapter, along with other methods used to determine the scales of fluctutation rely upon weak statistical stationarity. This however is not guaranteed in the whole dataset, especially in soft soils where compression due to the building of structures has occurred. It may be possible to utilise knowledge of the site history to account for this.

The reliability of the scale of fluctaution is related to the spacing of datapoints in relation to the scale of fluctuation itself. In the vertical direction this is not a problem as typically CPTs are vertical and mesure every ~2cm, but for the horizontal direction this poses a challenge as the spacing of horizontal CPT soundings is typically more than the scale of fluctuation. It has been previsouly suggested (Ching *et al.*, 2018), that using two CPTs within the horizontal scale of fluctuation in a thick layer would enable this measurement. However, this requires prior knowledge of either the critical scales of fluctuation of the structure considered (Hicks *et al.*, 2019) or the scale(s) of fluctation present. Moreover, as shown in this chapter, double scales of fluctation may be present, and these cannot be measured by only two CPT soundings. A practical approach to tackle these unknowns is to design site investigations using grouped CPTs as shown here.

The equations and charts proposed in this chapter to predict the uncertainty in the measured scales of fluctuation are emperical in form, but have been informed by comprehensive analysis of synthetic data. The form of the equations and the origin of the uncertainty from each of the parameters considered could be an anvenue for further research. In particular, the effect of datapoints spaced within the measured scale of fluctuation in the opposite (perpendicular) direction, i.e. the independence of the datapoints, should be further researched. Here, they have been considered fully dependent, which results in fewer datasets, and therefore a higher uncertainty.

Errors in other parts of geotechnical analysis may exist, e.g. in the material model, the geometry, the stress dependency and the calculation model. In particular, in this chapter it is assumed that direct measurements can be obtained from which the scale of fluctuation can be calculated. In practical situations however, measurements of soil properties used are obtained from indirect measurements, e.g. CPT soundings, where for example the CPT tip resistance is correlated to the undrained shear strength. Therefore transformation errors will also be present (Ching *et al.*, 2016). In a comprehensive probabilistic analysis these should also be taken into account.

3.6. CONCLUSION

The reliability of detecting sales of fluctuation in both the vertical and horizontal directions using CPT data has been robustly tested. Two methods to generate the auto-correlation function have been compared by using either an auto-correlation function directly or an NDFT has been shown to give equally accurate results, and can therefore be seen as viable alternative methods.

From the theoretical analysis using synthetically generated data, it has been shown that it is important to have enough information to make a reliable estimate of the SoF. A method has been proposed for estimating the CoV of the calculated SoF. Considering that multiple points need to be correlated, it is required to use a data interval that is sufficiently small to prevent aliasing. The estimation of the horizontal SoF using CPT

within a budget is a difficult task, given the large range of values that may be expected for θ_h. However, grouping CPTs can yield an improved estimate of the SoF, given limited CPTs and no prior knowledge of the SoF, as large and small scales of fluctuation can be detected.

The field data considered show a distinct difference between the vertical and horizontal scales of fluctuation, as expected. Based on these data, the horizontal spatial correlation may be better represented by a scale of fluctuation made up of two component scales of fluctuation, whereas the vertical spatial correlation is usually adequately described by a single scale of fluctuation.

REFERENCES

Alabert, F. (1987). The practice of fast conditional simulations through the LU decomposition of the covariance-matrix. *Mathematical Geology* **19**, No. 5, 369–386.

Arnold, P. (2016). *Probabilistic modelling of unsaturated slope stability accounting for heterogeneity*. Ph.D. thesis, University of Manchester.

Baecher, G. B. & Christian, J. T. (2003). *Reliability and statistics in geotechnical engineering*. Chichester, West Sussex, England: J. Wiley.

Cafaro, F. & Cherubini, C. (2002). Large sample spacing in evaluation of vertical strength variability of clayey soil. *Journal of Geotechnical and Geoenvironmental Engineering* **128**, No. 7, 558–568.

Campanella, R. G., Wickremesinghe, D. S. & Robertson, P. K. (1987). Statistical treatment of cone penetrometer test data. In *Proceedings of the 5th International Conference on Applications of Statistics and Probability in Soil and Structural Engineering*, vol. 2, pp. 1011–1019.

Chiasson, P., Lafleur, J., Soulié, M. & Law, K. T. (1995). Characterizing spatial variability of a clay by geostatistics. *Canadian Geotechnical Journal* **32**, No. 1, 1–10.

Ching, J., Phoon, K.-K. & Wu, T.-J. (2016). Spatial correlation for transformation uncertainty and its applications. *Georisk: Assessment and Management of Risk for Engineered Systems and Geohazards* , 1–18.

Ching, J., Wu, T.-J., Stuedlein, A. W. & Bong, T. (2018). Estimating horizontal scale of fluctuation with limited CPT soundings. *Geoscience Frontiers* **9**, No. 6, 1597 – 1608.

Davis, M. W. (1987). Production of conditional simulations via the LU triangular decomposition of the covariance matrix. *Mathematical Geology* **19**, No. 2, 91–98.

de Gast, T., Vardon, P. J. & Hicks, M. A. (2017). Estimating spatial correlations under man-made structures on soft soils. *Geo-risk 2017* **GSP 284**, 382–389.

de Gast, T., Vardon, P. J. & Hicks, M. A. (2018). Detection of soil variability using CPTs. *CPT18* , 289–294.

de Gast, T., Vardon, P. J. & Hicks, M. A. (2019). Observations and considerations regarding estimating horizontal scales of fluctuation around linear infrastructure. *ISGSR 2019* , 340–345.

Fenton, G. A. (1999a). Estimation for stochastic soil models. *Journal of Geotechnical and Geoenvironmental Engineering* **125**, No. 6, 470–485.

Fenton, G. A. (1999b). Random field modeling of CPT data. *Journal of Geotechnical and Geoenvironmental Engineering* **125**, No. 6, 486–498.

Fenton, G. A. & Griffiths, D. V. (2008). *Risk assessment in geotechnical engineering*. John Wiley and Sons, Inc.

Firouzianbandpey, S., Griffiths, D., Ibsen, L. & Andersen, L. (2014). Spatial correlation length of normalized cone data in sand: case study in the north of denmark. *Canadian Geotechnical Journal* **51**, No. 8, 844–857.

Griffiths, D. & Fenton, G. A. (2007). *The random finite element method (RFEM) in slope stability analysis*. Vienna: Springer Vienna, pp. 317–346.

Griffiths, D. V. & Fenton, G. A. (1997). Three-dimensional seepage through spatially random soil. *Journal of Geotechnical and Geoenvironmental Engineering* **123**, No. 2, 153–160.

Hicks, M. A., Nuttall, J. D. & Chen, J. (2014). Influence of heterogeneity on 3D slope reliability and failure consequence. *Computers and Geotechnics* **61**, 198–208.

Hicks, M. A. & Onisiphorou, C. (2005). Stochastic evaluation of static liquefaction in a predominantly dilative sand fill. *Géotechnique* **55**, No. 2, 123–133.

Hicks, M. A. & Samy, K. (2002). Influence of heterogeneity on undrained clay slope stability. *Quarterly Journal of Engineering Geology and Hydrogeology* **35**, No. 1, 41–49.

Hicks, M. A. & Spencer, W. A. (2010). Influence of heterogeneity on the reliability and failure of a long 3D slope. *Computers and Geotechnics* **37**, No. 7-8, 948–955.

Hicks, M. A., Varkey, D., van den Eijnden, A. P., de Gast, T. & Vardon, P. J. (2019). On characteristic values and the reliability-based assessment of dykes. *Georisk: Assessment and Management of Risk for Engineered Systems and Geohazards* **Ahead of print**.

Hoeg, K. & Tang, W. H. (1977). Probabilistic considerations in the foundation engineering for offshore structures. In *In: Proc. 2 nd Int. Conf. Structural Safety and Reliability*.

Honjo, Y. (2011). Challenges in geotechnical reliability based design. *Proceedings of the 3rd International Symposium on Geotechnical Safety and Risk, ISGSR (2011)* , 11–28.

Jaksa, M. (1995). *The influence of spatial variability on the geotechnical design properties of a stiff, overconsolidated clay*. Ph.D. thesis, The University of Adelaide.

Jaksa, M. B., Goldsworthy, J. S., Fenton, G. A., Kaggwa, W. S., Griffiths, D. V., Kuo, Y. L. & Poulos, H. G. (2005). Towards reliable and effective site investigations. *Géotechnique* **55**, No. 2, 109–121.

Jaksa, M. B., Kaggwa, G. W. S. & Brooker, P. I. (1999). Experimental evaluation of the scale of fluctuation of a stiff clay. In *Proceedings of International conference on applications of statistics and probability; Applications of statistics and probability civil engineering reliability and risk analysis*, pp. 415–422.

Keaveny, J. M., Nadim, F. & Lacasse, S. (1989). Autocorrelation functions for offshore geotechnical data. In *International Conference of Structural Safety and Reliability*, pp. 263–270.

Lacasse, S. & de Lamballerie, J. Y. (1995). Autocorrelation functions for offshore geotechnical data. In *Proceedings of the International Symposium on Cone Penetration Testing*, pp. 4–5.

Li, Y. J., Hicks, M. A. & Vardon, P. J. (2016). Uncertainty reduction and sampling efficiency in slope designs using 3D conditional random fields. *Computers and Geotechnics* **79**, 159–172.

Lloret-Cabot, M., Fenton, G. A. & Hicks, M. A. (2014). On the estimation of scale of fluctuation in geostatistics. *Georisk: Assessment and Management of Risk for Engineered Systems and Geohazards* **8**, No. 2, 129–140.

Lloret-Cabot, M., Hicks, M. A. & van den Eijnden, A. P. (2012). Investigation of the reduction in uncertainty due to soil variability when conditioning a random field using kriging. *Géotechnique Letters* **2**, No. July-September, 123–127.

Naghibi, F., Fenton, G. A. & Griffiths, D. V. (2016). Probabilistic considerations for the design of deep foundations against excessive differential settlement. *Canadian Geotechnical Journal* **53**, No. 7, 1167–1175.

Nie, X., Zhang, J., Huang, H., Liu, Z. & Lacasse, S. (2015). Scale of fluctuation for geotechnical probabilistic analysis. In *Proc. 2 nd Int. Conf. Structural Safety and Reliability*, pp. 834–840.

Phoon, K.-K. & Kulhawy, F. H. (1999). Characterization of geotechnical variability. *Canadian Geotechnical Journal* **36**, No. 4, 612–624.

Phoon, K. K., Quek, S. T. & An, P. (2004). Geostatistical analysis of cone penetration test (CPT) sounding using the modified Bartlett test. *Canadian Geotechnical Journal* **41**, No. 2, 356–365.

Pieczyńska-Kozłowska, J., Puła, W. & Vessia, G. (2017). A collection of fluctuation scale values and autocorrelation functions of fine deposits in Emilia Romagna Palin. *Italy, Geo-Risk* , 290–299.

Pieczyńska-Kozłowska, J. M. (2015). Comparison between two methods for estimating the vertical scale of fluctuation for modeling random geotechnical problems. *Studia Geotechnica et Mechanica* **37**, No. 4, 95–103.

Popescu, R., Deodatis, G. & Nobahar, A. (2005). Effects of random heterogeneity of soil properties on bearing capacity. *Probabilistic Engineering Mechanics* **20**, No. 4, 324–341.

Sert, S., Luo, Z., Xiao, J. H., Gong, W. P. & Juang, C. H. (2016). Probabilistic analysis of responses of cantilever wall-supported excavations in sands considering vertical spatial variability. *Computers and Geotechnics* **75**, 182–191.

Spencer, W. A. & Hicks, M. A. (2007). A 3D finite element study of slope reliability. In *Numerical Models in Geomechanics: Numog X*, CRC Press, pp. 539–543.

Suchomel, R. & Mašín, D. (2010). Comparison of different probabilistic methods for predicting stability of a slope in spatially variable c–ϕ soil. *Computers and Geotechnics* **37**, No. 1-2, 132–140.

Uzielli, M., Vannucchi, G. & Phoon, K. (2005). Random field characterisation of stress-normalised cone penetration testing parameters. *Géotechnique* **55**, No. 1, 3–20.

van den Eijnden, A. P. & Hicks, M. A. (2017). Efficient subset simulation for evaluating the modes of improbable slope failure. *Computers and Geotechnics* **88**, No. Supplement C, 267–280.

Vanmarcke, E. (1977). Reliability of earth slopes. *Journal of the Geotechnical Engineering Division-ASCE* **103**, No. 11, 1247–1265.

Vanmarcke, E. (1983). *Random fields, analysis and synthesis*. Cambridge, Mass.: MIT Press.

Vanmarcke, E., Shinozuka, M., Nakagiri, S., Schueller, G. I. & Grigoriu, M. (1986). Random-fields and stochastic finite-elements. *Structural Safety* **3**, No. 3-4, 143–166.

Varkey, D., Hicks, M. A. & Vardon, P. J. (2018). 3D slope stability analysis with spatially variable and cross-correlated shear strength parameters. In *Proceedings of the 9th European Conference on Numerical Methods in Geotechnical Engineering (NUMGE 2018)*, pp. 543–549.

Varkey, D., Hicks, M. A. & Vardon, P. J. (2019). An improved semi-analytical method for 3D slope reliability assessments. *Computers and Geotechnics* **111**, 180–190.

Wickremesinghe, D. & Campanella, R. G. (1993). Scale of fluctuation as a descriptor of soil variability. In *Proceedings of the Conference of Probabilistic Methods in Geotechnical Engineering*, pp. 233–239.

Wong, S. Y. (2004). *Stochastic characterisation and reliability of saturated soils*. Ph.D. thesis, University of Manchester.

4

APPLYING RFEM TO THE FAILURE EXPERIMENT

A reliability-based analysis framework, accounting for uncertainty arising from the spatial variability of soil properties, has been validated for the controlled, well-instrumented slope failure of an historic dyke in the Netherlands. Using soil property statistics derived from the results of laboratory and CPT data for the different soil layers at the site, the dyke was analysed for the initial (i.e., operating) conditions, as well as for the later stage of the test leading up to failure. The computed probabilities of failure and back-figured factors of safety were consistent with the point at which failure occurred in the test, as was the range of possible failure mechanisms. The uncertainty in the stability assessment was reduced by considering the spatial nature of the soil variability, and by conditioning analyses to CPT measurement data. It is shown that the reliability-based approach enables more informed stability assessments that could make the difference between a dyke being assessed as safe or requiring costly improvement.

This chapter has been submitted as an article to Géotechnique and is an improvement on de Gast *et al.* (2018).

4.1. INTRODUCTION

The spatial variability of soils at different scales influences material behaviour and the response of geotechnical structures, as well as causing uncertainty in stability assessments and geotechnical design (Hicks, 2005). There has therefore been much research into the measurement and quantification of spatial variability (e.g., Vanmarcke, 1977; Campanella *et al.*, 1987; Wickremesinghe & Campanella, 1993; Phoon & Kulhawy, 1999; Lloret-Cabot *et al.*, 2014; Fenton *et al.*, 2018; de Gast *et al.*, 2019a), and into probabilistic methods of analysis for propagating the effects of uncertainty from the material level to the geotechnical structure level. These methods have included semi-analytical methods such as the point estimate method (Rosenblueth, 1972), first order reliability method (Ang & Tang, 1984) and first order second moment method, as well as computational methods, such as those linking random fields with various limit equilibrium methods (Cho, 2007; Jiang *et al.*, 2014; Javankhoshdel *et al.*, 2017), sometimes referred to as the random limit equilibrium method (RLEM), and the random finite element method (RFEM) (Griffiths & Fenton, 1993; Fenton & Griffiths, 2008). There now exists a wide body of literature investigating the influence of spatial variability (in so-called uniform layers of soil) on the performance of geotechnical structures, although the practical application of probabilistic methods remains low, especially for those methods that are computationally intensive.

Examples of the use of probabilistic methods in geotechnical slope stability case histories involving the influence of spatial variability include Alonso (1976), who used the method of slices to study the Green Creek slide in sensitive clay, (El-Ramly *et al.*, 2002, 2003, 2005), who used limit equilibrium methods to analyse a series of case histories, and Cho (2007) and Cami *et al.* (2018), who used RLEM to analyse the stability of the Sugar Creek Embankment using 1D and 2D random fields, respectively. Hicks & Onisiphorou (2005) used RFEM to investigate the influence of spatial variability of state parameter (Been & Jefferies, 1985) on the liquefaction potential of the Nerlerk underwater berm (Hicks & Boughrarou, 1998), demonstrating that it was possible for a predominantly dilative fill to liquefy due to failure through deposition-induced, semi-continuous weak zones. Recently, Hicks *et al.* (2019) used RFEM to assess the stability of an existing dyke in Starnmeer, North Holland, that was not meeting design safety requirements according to existing assessment methods. It was demonstrated that a consideration of the spatial nature of the variability not only led to a more realistic and less pessimistic safety assessment of a dyke that had remained stable for hundreds of years, but also to more economical and environmentally less intrusive mitigation measures.

This chapter reports a unique opportunity to validate advanced probabilistic techniques by analysing the controlled failure (Chapter 2), the evaluation of material property statistics including spatial correlation scales (Chapter 3), and presents RFEM analyses of the dyke before the test and in the final stage of the test leading up to failure. The results of the analyses are consistent with the field observations and recorded measurements. It is demonstrated that the quantification of uncertainty associated with spatial variability is beneficial to an objective approach to slope stability assessment and design. Other sources of uncertainty (e.g. measurement, statistical, model) have not been studied in this chapter, but may be included in a more general framework characterising total uncertainty (van den Eijnden & Hicks, 2019).

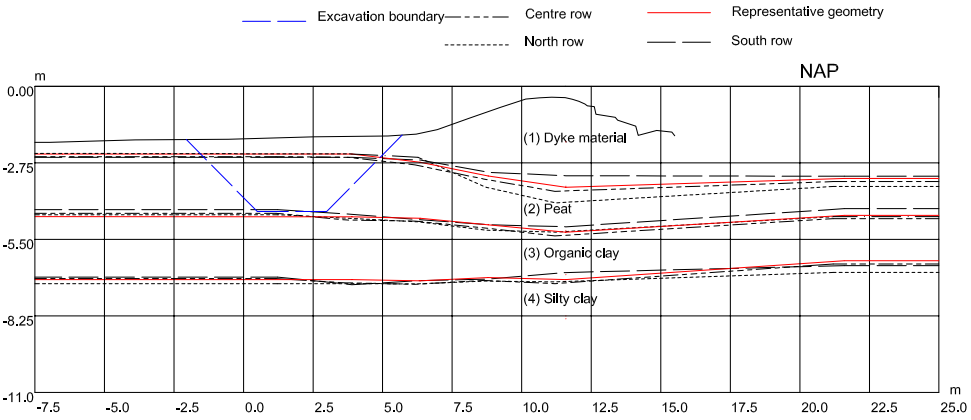

Figure 4.1: Stratigraphy interpretation from the three rows of CPTs (repeated from Figure 2.6)

4.2. LEENDERT DE BOERSPOLDER FIELD TEST

As stated in Chapter 2, Leendert de Boerspolder was a small polder in South Holland, located south of one of the more economically important polders of the Netherlands, the Haarlemmermeerpolder, where Schiphol airport is situated. The design, implementation and evaluation of the failure test is described by Chapter 2.

Figure 4.1 shows a cross-section through the dyke at the location of the failure test. The crest of the embankment was at NAP –0.4 m and the depth of the polder varied between NAP –1.9 m and NAP –2.1 m, in which NAP is the Dutch national reference level. The body of water south of the polder (the Hanepoel) has a fixed level of NAP –0.6 m, and over the course of the year this level varies ±0.05 m. In the polder, the water level was maintained at NAP –2.45 m in a series of ditches (not present at the failure test location).

Two site investigations were conducted at Leendeert de Boerspolder as part of the Reliable Dykes project: at one location, 100 CPTu soundings and 6 borings were undertaken as part of a detailed study on soil heterogeneity (Chapter 3); the second series of tests were conducted prior to, and at the location of, the failure test and were used in the analyses presented herein. Figure 4.2 shows a plan view of the second site investigation, which included 17 CPTu meeting the specifications of NEN-ISO 22476-1 (Class 1), and one ball CPT. These penetrated as far as a deep underlying sand layer at NAP –16 m (not included in any of the analysed cross-sections) and, to enable both deterministic analyses and RFEM analyses and not to significantly affect the test, they were arranged in three rows of 6 CPTs aligned to get three perpendicular cross sections to the dyke at 20 m intervals, and are denoted as the North, Centre and South rows in the figure. In each row, from the polder to the dyke crest the spacing between the CPTs was (in general) 2.5 m, and a 6th CPT was located in the canal and undertaken from a pontoon 10 m from the crest. Equidistant between the rows of CPTs were two rows of three borings, made using a 100 mm diameter piston sampler and providing semi-continuous samples in 70 cm sections. Inclinometers were installed to measure the horizontal displacement in line with the Centre row CPTs and close to the borings equidistant between the rows of CPTs.

Based on the CPT measurement data (i.e., cone tip resistance, sleeve friction, and

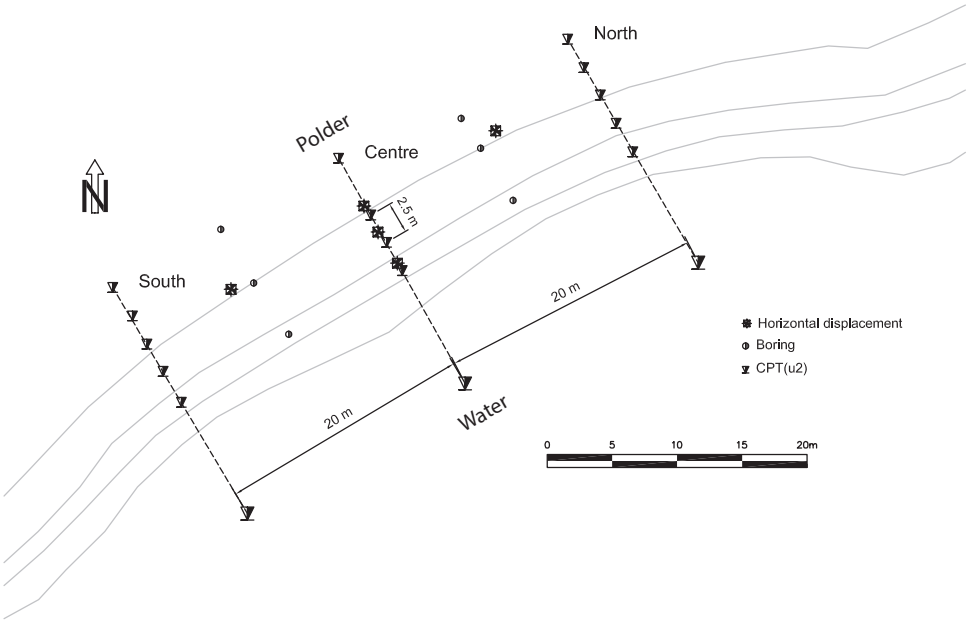

Figure 4.2: Plan view of site investigation: three lines, each with 5 closely spaced CPTs on land and 1 CPT in the water, and two lines of 3 semi-continuous borings in the crest, slope and polder. From left to right, these lines are South, Centre and North (repeated from Figure 2.4)

water pressure behind the cone), and the borehole data, the following four major material layers were identified, starting from the ground surface:

a) Dyke material: this had been placed over time, since ~1600 AD, initially for the original construction and subsequently by adding to the dyke periodically for maintenance.

b) Peat: this layer has been affected by the overlying dyke material and, in the polder, by constant dewatering. The thickness of the layer varies from 1.0–1.8 m under the dyke to 1.8 – 2.2 m in the polder.

c) Organic clay: the layer starts with a high organic fraction at the top, decreasing with depth. Its thickness is 1.6–1.8 m under the dyke to 2.4–2.5 m in the polder.

d) Silty clay: as the organic content decreases, the silt fraction increases and the clay layer continues until NAP –16 m, beyond which sand is found

Figure 4.1 shows a cross-section through the stratigraphy detected by each of the three CPT rows, as well as a single representative stratigraphy. All four stratigraphies have been considered in the numerical analyses

The dyke was saturated with water by using a water sprinkler system that was left on continuously for a period of one week, and then the soil in front of the toe was excavated in stages and replaced by water, effectively increasing the height of the dyke (full elaboration

in Chapter 2). Eventually, the ditch was excavated to the bottom of the peat layer (i.e., NAP –4.4 m), at 2.5 m below the ground surface (NAP–1.9 m). Then, in the final stage of the experiment, the water in the excavation was removed and the dyke failed under its own weight, with the main failure occurring just south of the centre of the excavation. Large differential displacements were measured in the toe, and in the organic clay layer just below the boundary between the peat and organic clay. The failure occurred at a drawdown somewhere between 1.5 m and 2.0 m (i.e. between NAP –3.4 m and NAP –3.9 m), and was estimated to be at 1.6 m (i.e., NAP –3.5 m).

4.3. MATERIAL PROPERTIES

The point and spatial statistics of undrained shear strength were determined prior to the wetting stage using the 17 CPT tests (Figure 4.2), as well as data from laboratory tests on the borehole samples. The wetting was thought to have a limited effect as the pore pressure increments were observed to be small (see Figure 2.14). The undrained shear strength profiles for the soil layers were determined from the CPT data using the relation (Robertson, 2009),

$$s_u = \frac{q_t - \sigma_v}{N_{kt}} \tag{4.1}$$

where q_t is the total cone resistance, σ_v is the total vertical stress and N_{kt} is an empirical correction factor. Robertson (2009) suggested values for N_{kt} in the range 10–20. The procedure used here to estimate the N_{kt} values was as follows (Chapter 2): (1) the laboratory data, comprising 20 consolidated triaxial compression tests and four direct simple shear tests (Ponzoni, 2017; Muraro, 2019), were used to determine the maximum shear strength as a function of depth; (2) the mean and standard deviation of the q_t data were determined for each 0.25 m depth interval; (3) Equation 4.1 was used to calculate an N_{kt} value for each material, so that the s_u determined from the CPT data best fitted the laboratory data. The values of N_{kt} determined for the four soil layers were: dyke material, $N_{kt} = 20$; peat, $N_{kt} = 15$; organic clay, $N_{kt} = 10$; and silty clay, $N_{kt} = 10$.

Using the derived values of N_{kt}, the CPT data were transformed to s_u profiles, and the mean (or mean trend) and standard deviation of s_u for each soil layer then found. Table 4.1 summarises the point statistics based on all CPT profiles, as well as those based on the three CPT rows individually. The mean trend was computed for the peat and both clay layers, but no clear trend was identified for the dyke material. The standard deviation was calculated relative to the depth-dependent mean for the peat and clay layers. Figure 4.3 shows the CPT profiles for s_u, which are plotted with respect to local horizontal axes (with the shown scale representing 0–10 kPa). The figure shows how the shear strength varies with respect to depth, for each CPT row and for each material, especially for the clay layers. When approximating the distribution of s_u data for each soil layer, a normal distribution relative to the depth-dependent mean was adopted for the peat and clay layers, whereas a lognormal probability density function was found to be the best fit for the dyke material. Note that a small number of extreme data values, for example, as are apparent for the Centre row CPTs in Figure 4.3(b), were considered anomalous and not included in the derived statistical values listed in Table 4.1.

Table 4.2 summarises the computed vertical and horizontal scales of fluctuation for

Table 4.1: Derived point statistics of undrained shear strength (in kPa)

CPTs used:	All		North row		Centre row		South row	
	$s_{u;\mu}$	$s_{u;\sigma}$	$s_{u;\mu}$	$s_{u;\sigma}$	$s_{u;\mu}$	$s_{u;\sigma}$	$s_{u;\mu}$	$s_{u;\sigma}$
Dyke material	17.69	12.98	18.89	11.63	14.78	10.05	19.46	16.36
Peat	4.88 -1.90z	5.07	8.76 -1.17z	5.09	3.39 -2.46z	3.57	4.94 -1.45z	5.61
Organic clay	-8.32 -4.43z	5.22	3.21 -2.64z	4.93	-17.26 -6.25z	6.27	-6.95 -3.78z	2.97
Silty clay	-5.68 -3.62z	4.02	-3.10 -3.61z	4.72	-7.11 -3.80z	2.63	-6.08 -3.37z	2.25

N.B. z is the location relative to NAP

the four soil layers. These were obtained by minimising, in both the vertical and horizontal directions, the squared difference ($Er(\theta)$) between the experimental autocorrelation function ($\hat{\rho}(\tau)$) obtained from the CPT data and a theoretical (Markov) autocorrelation function ($\rho(\tau) = e^{\frac{-2|\tau|}{\theta}}$), as shown in Figures 4.4(a)–4.4(b) (Chapter 2). Specifically, the error to be minimised is

$$Er(\theta) = \sum(\rho(\tau_i) - \hat{\rho}(\tau_i))^2 \tag{4.2}$$

where τ_i are all available lag distances for which data are available and $\rho(\tau)$ is given by

$$\hat{\rho}(\tau) = \frac{\hat{\gamma}(\tau)}{\hat{\gamma}(0)} \tag{4.3}$$

where $\hat{\gamma}(\tau)$ is the experimental covariance function, and $\hat{\gamma}(0)$ is the experimental covariance function when $\tau = 0$ (i.e. the point variance). For unequally spaced data, this is given by (Vanmarcke, 1983)

$$\hat{\gamma}(\tau) = \frac{1}{t-1}\sum_{j=1}^{t}(y_j - \hat{\mu})(y'_j - \hat{\mu}) \tag{4.4}$$

where y_j and y'_j are two data at locations separated by lag distance τ,$\hat{\mu}$ is the estimated mean (or trend) of the dataset, and $j = 1,2,\ldots,t$ is a counter representing the number of pairs of data at lag distance τ. In this chapter, for the purpose of deriving the experimental autocorrelation functions, and thereby θ_v and θ_h, the CPT data were first de-trended (i.e., with respect to the actual depth-dependent mean). Table 4.2 shows the scales of fluctuation to be small (0.3–0.8 m) in the vertical direction, as has generally been found by other researchers for other soils, and as found for the same soil layers at the adjacent test site at Leendert de Boerspolder (de Gast *et al.*, 2017, 2019b). The scales of fluctuation in the horizontal direction were found to be 4–8 times larger than the vertical scales of fluctuation. However, it should be noted that θ_h was determined along the CPT rows perpendicular to the dyke (Figure 4.2), with the CPTs in each row positioned at 2.5 m centres on average. Due to the derived values of θ_h being similar in magnitude to the CPT spacing, there is some doubt as to their accuracy, although they are generally consistent with values obtained at the adjacent test site which used CPT spacings of only 1.25 m (de Gast *et al.*, 2017, 2019b). Moreover, it seems reasonable that θ_h would be at least several times greater than θ_v, due to the natural process of deposition, and there is confidence in the derived values of θ_v due to the large number of closely spaced data available to construct the experimental autocorrelation functions in the vertical direction.

Table 4.2: Derived scales of fluctuation

	θ_v [m]	θ_h [m]
Dyke material	0.40	2.13
Peat	0.76	2.84
Organic clay	0.76	2.84
Silty clay	0.26	2.10

The estimation of the spatial statistics for the organic clay layer using Equation 4.4 is illustrated in Figures 4.4(a) and 4.4(b). The experimental autocorrelation function in the vertical direction (Figure 4.4(a)) is equivalent to the average of 17 experimental functions, as obtained from each of the 17 CPTs. In contrast, the experimental autocorrelation function in the horizontal direction (Figure 4.4(b)) is equivalent to the average of a larger number of experimental functions, with each one corresponding to a different depth interval but based on the number of CPTs in the row. Figure 4.4 illustrates how the experimental autocorrelation function is less reliable at larger lag lengths, due to the fewer pairs of data then available for input into Equation 4.4.

The unit weights for the four soil layers are (Ponzoni, 2017): dyke material, γ_{sat} = 18 kN/m^3; peat, γ_{sat} = 10 kN/m^3; organic clay, γ_{sat} = 15 kN/m^3; and silty clay, γ_{sat} = 17 kN/m^3. No information on the variability of the unit weights was determined, although previous researchers have generally found the coefficient of variation to be low and typically in the range 0.05–0.1 (Phoon & Kulhawy, 1999). In any case, any variability in the unit weights should have a minimal impact on the presented numerical analyses for two reasons: (i) the analyses are total stress, so that the soil resistance is independent of the unit weight; and (ii) the scales of fluctuation are small relative to the geometry of the sliding mass, so that there will be significant spatial averaging of unit weights and thereby minimal influence on the overturning moment.

4.4. NUMERICAL MODELLING

The dyke has been analysed using the random finite element method (RFEM) (Griffiths & Fenton, 1993; Fenton & Griffiths, 2008). In this method, multiple realisations of the boundary value problem are analysed by the finite element method, with the spatial variability of material properties being modelled by different random fields in each realisation. These fields are based on an assumed probability density function and the point statistics (mean μ and standard deviation σ) of each spatially varying soil property, and by an assumed covariance function and the spatial correlation statistics (i.e., the scales of fluctuation in the vertical and horizontal directions, θ_v and θ_h, respectively, which represent the spatial scales over which the soil property values are significantly correlated). For a given set of point and spatial soil property statistics, RFEM computes an ensemble of responses for the boundary value problem (based on the different random fields), leading to a reliability-based safety assessment (as opposed to a single factor of safety).

One advantage of using the finite element method to analyse the boundary value problem is that no prior assumptions are needed regarding the failure mechanism

geometry or its location (Hicks & Boughrarou, 1998), in contrast to the simpler limit equilibrium methods such as those based on the traditional method of slices. This is particularly relevant when accounting for the effects of soil spatial variability, as failure mechanisms can take on many forms when attracted to paths of least resistance (Hicks & Samy, 2002; Hicks & Spencer, 2010; Hicks *et al.*, 2014). Although more advanced limit equilibrium methods can analyse more general mechanisms (Cho, 2007; Javankhoshdel *et al.*, 2017), finite elements are also able to account for more realistic soil constitutive behaviour (Hicks & Onisiphorou, 2005). An obvious disadvantage of RFEM, especially when considering problems in three dimensions, is that it is computationally expensive, although recent advances in computer power (e.g. through grid and cloud computing) are making such analyses more accessible (Li *et al.*, 2015; Hicks & Li, 2018).

In this chapter, the spatial variation of material properties has been modelled by random fields generated using covariance matrix decomposition with local averaging for unstructured meshes (van den Eijnden & Hicks, 2017). The method starts by generating a random field with values at locations matching the Gauss points of the finite element spatial discretisation, based on a standard normal distribution and a spatial correlation function incorporating the scales of fluctuation. The standard normal field is then transformed to the appropriate distribution using the marginal distribution of the property being modelled. In any realisation, each soil layer is modelled by a separate random field characterised by the soil property statistics for that layer. Figures 4.5(a) to 4.5(d) show typical random field realisations of shear strength for the dyke (before excavation of the ditch), in which a log scale has been adopted to improve the clarity of the visualisations. For any given soil layer, the spatial distributions of shear strength are statistically similar (but spatially different) across the realisations, because they are based on the same point and spatial statistics in each realisation. Figures 4.5(e) to 4.5(h) show typical realisations in which the random fields are conditioned to measurement data (i.e., so that the random field values match the CPT data (van den Eijnden *et al.*, 2017) at the Centre row CPT locations (Figure 4.2); hence, because the properties at the CPT locations are the same in each realisation, there is less uncertainty in the spatial variability (Lloret-Cabot *et al.*, 2012; Li *et al.*, 2016).

Various cross-sections through the dyke failure test have been analysed in plane strain. Figure 4.6(a) shows the finite element mesh and problem geometry based on the North row stratigraphy in Figure 4.1, in which the boundaries of the domain are located far enough from the dyke so as not to influence the results. The bottom boundary is fixed, whereas the vertical boundaries allow only vertical displacement, and, as only the stability of the dyke is of interest, only one side of the excavated ditch has been modelled. On each side of the dyke an external hydrostatic load was applied representing the water load: on the canal side the water level was at NAP –0.6 m, whereas on the polder side the water level in the excavation depended on the particular stage of the test being modelled. The finite element mesh comprised 4388 eight-node quadrilateral elements, with each element using 2×2 Gaussian integration. Similar finite element meshes were generated for analyses involving the stratigraphy encountered at the Centre and South rows, as well as for analyses involving the representative stratigraphy at the site (Figure 4.1).

In this chapter, each RFEM analysis has involved 1000 realisations, and, in each realisation of the RFEM analysis, the factor of safety of the dyke has been computed using

Table 4.3: Overview of the inital condition and final stage RFEM and deterministic analyses

Geometry	Water level [m to NAP]	RFEM analysis conditioned by CPT row? Unconditional	North	Centre	South	Deterministic
		✓(All*),✓(Centre*)	-	✓	-	✓(Mean, med., 5 %*)
Initial	-	✓(All*)	✓	✓	✓	-
Ditch	-1.9	✓(All*)	✓	✓	✓	-
Ditch	-2.4	✓(All*)	✓	✓	✓	-
Ditch	-2.9	✓(All*)	✓	✓	✓	-
Ditch	-3.4	✓(All*)	✓	✓	✓	-
Ditch	-3.9	✓(All*)	✓	✓	✓	-

* data used in the unconditional analysis

the strength reduction method. Specifically, the dyke has been repeatedly analysed, by generating the in situ stresses due to gravity loading and external water loading, and by sequentially scaling down the soil shear strength, with the factor of safety being the smallest scaling factor required to bring the dyke to failure under its own weight. Each realisation typically took 15 minutes on a standard PC; however, grid computing was used to enable many realisations to be undertaken at the same time. Figures 4.6(b) and 4.6(c) show a typical undrained shear strength distribution before strength reduction and the resulting failure mechanism after strength reduction, respectively, for a single RFEM realisation using the finite element mesh in Figure 4.6(a). A total stress analysis has been performed, using an elastic, perfectly plastic Tresca soil model and material properties based on the data presented by Chapter 2. However, only the shear strength has been taken as spatially random, while other parameters have been assumed constant for each layer. The shear strength profile for each layer has been defined by either a lognormal or normal probability density function (characterised by a mean $s_{u;\mu}$ and standard deviation $s_{u;\sigma}$, see Table 4.1, where z is the location relative to NAP), and by a Markov covariance function (characterised by θ_v and θ_h, see Table 4.2).

Table 4.3 summarises the analyses carried out, in which two stages of the test have been investigated in detail: the initial condition, before any excavation, and at the final stage leading up to the dyke failure, in which the water level in the excavated ditch was gradually lowered until failure at a water level in the range of NAP –3.4 m to NAP –3.9 m. For each stage and/or water level considered, up to four RFEM analyses have been performed: one based on unconditional random fields, and three based on random fields conditioned against one of the three CPT rows shown in Figure 4.2 (North, Centre or South). In addition, deterministic analyses based on single "representative" strengths (i.e., mean, median, and 5-percentile[1] s_u values), for the individual soil layers, have been carried out for comparative purposes for the initial condition.

[1] A 5-percentile value is often chosen to satisfy the Eurocode requirement of a cautious estimate of the mean ensuring a 95% reliability of the structure.

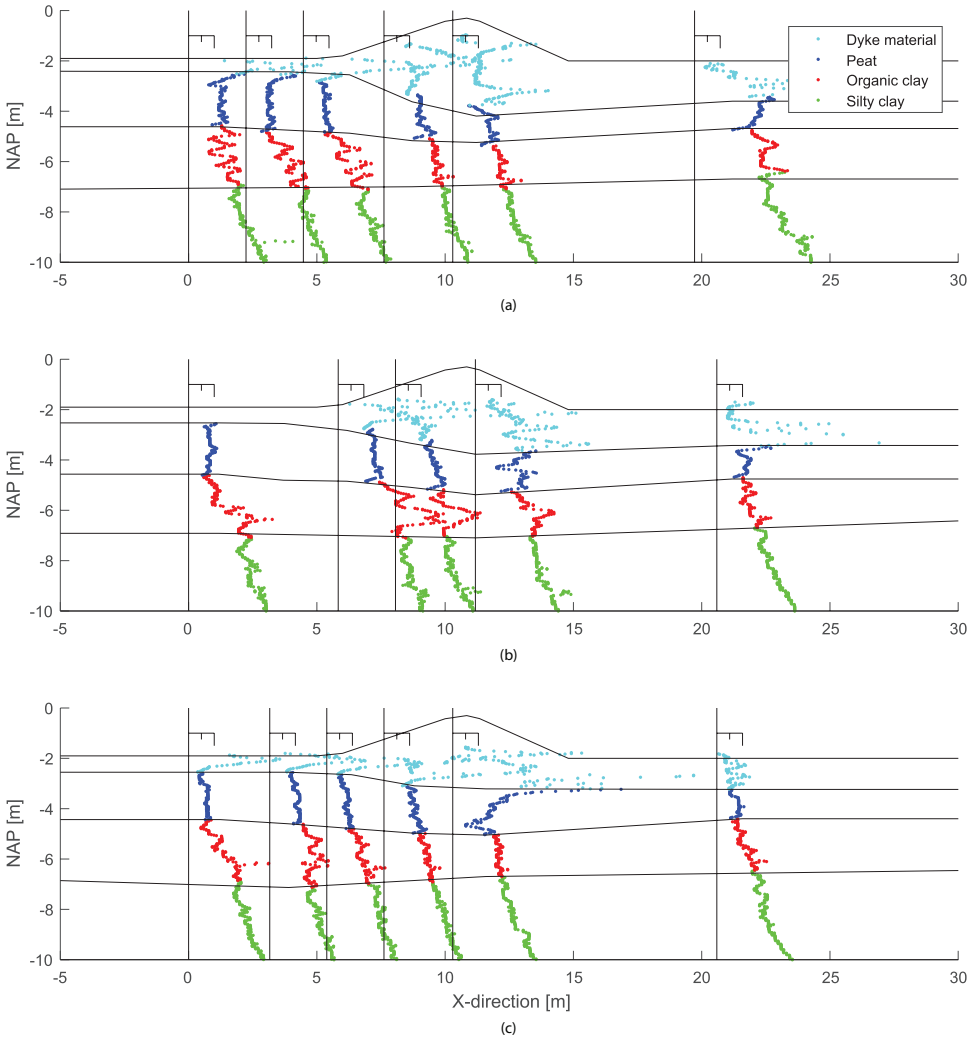

Figure 4.3: Input data for conditioning random fields. Three rows of CPTs with the normalised CPT data per (coloured) soil layer: (a) North row; (b) Centre row; (c) South row

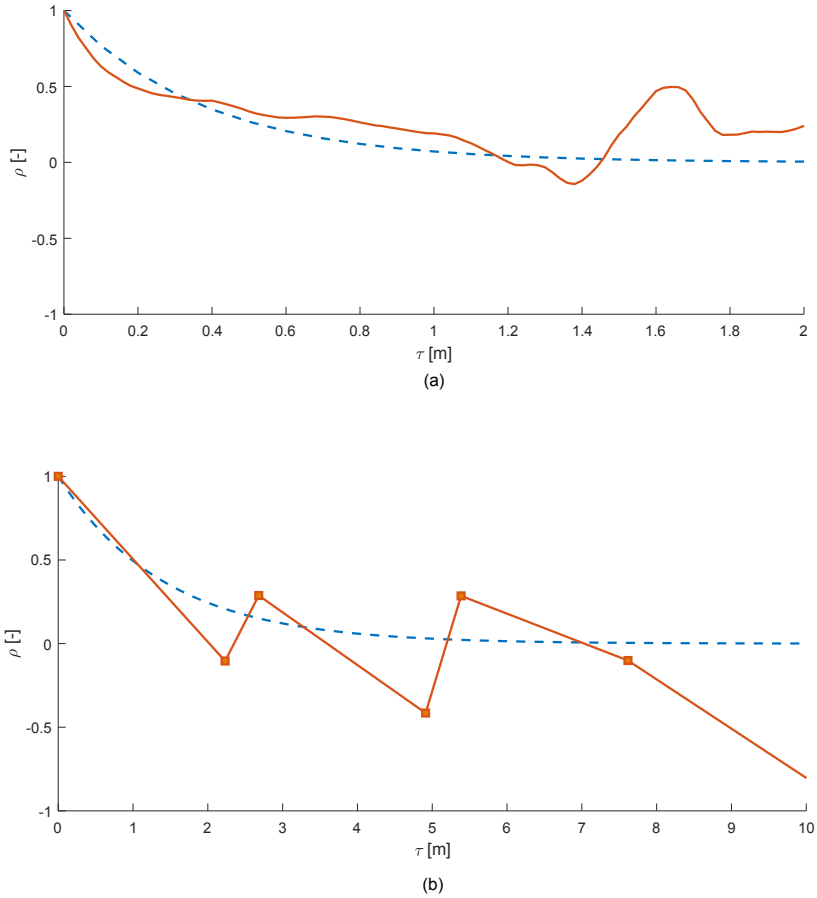

Figure 4.4: Derivation of point and spatial statistics for organic clay layer: (a) vertical autocorrelation functions (experimental, solid line; theoretical, broken line); (b) horizontal autocorrelation functions (experimental, solid line; theoretical, broken line)

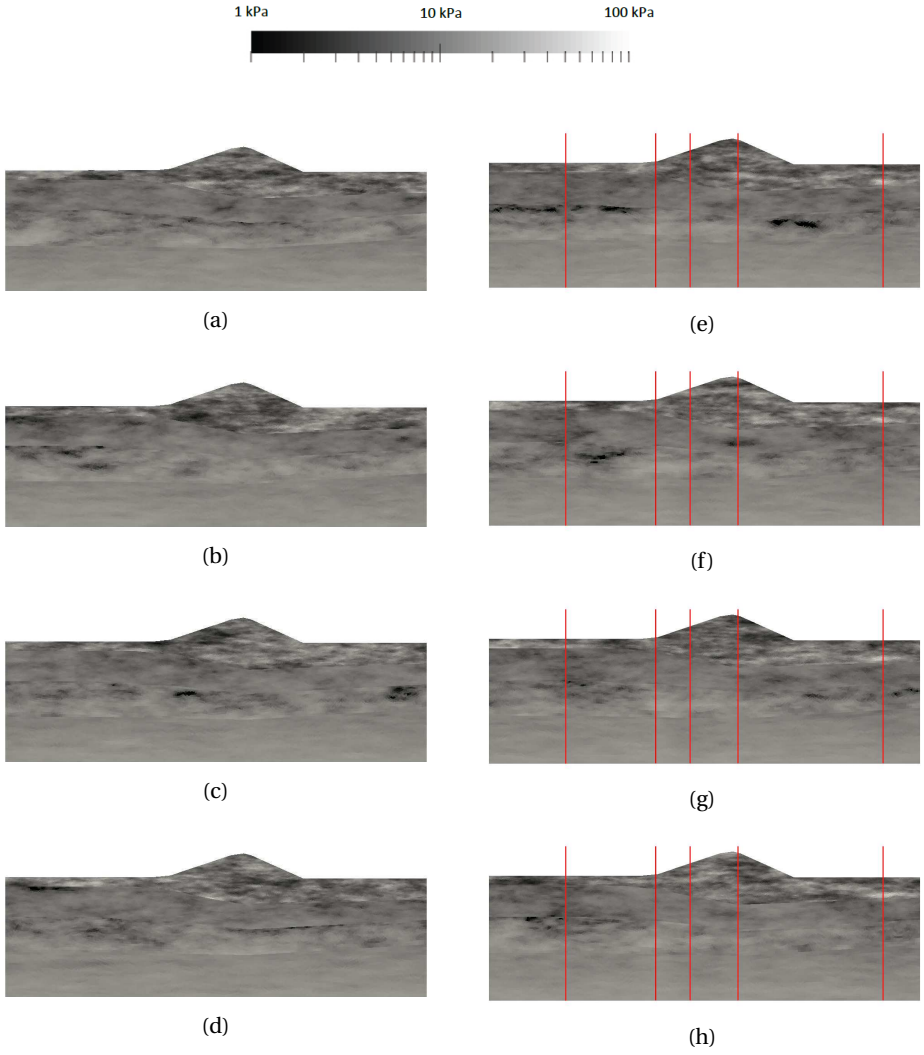

Figure 4.5: Typical random fields of undrained shear strength for Centre row (in kPa on a logarithmic scale): (a)-(d) unconditional random fields; (e)-(h) conditional random fields, conditioned to Centre row CPTs at locations indicated by vertical lines

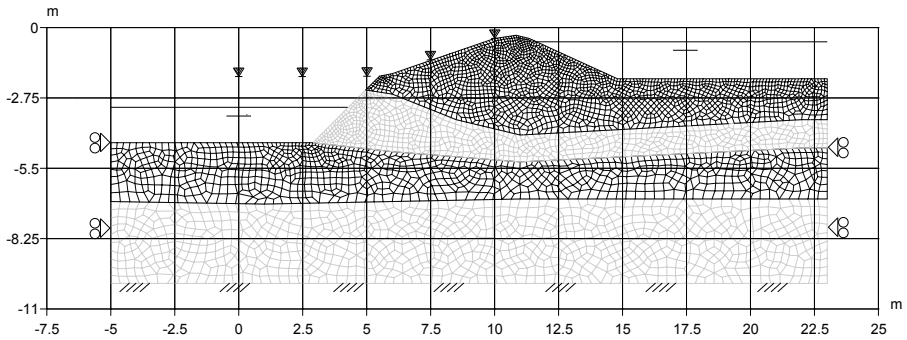

(a)

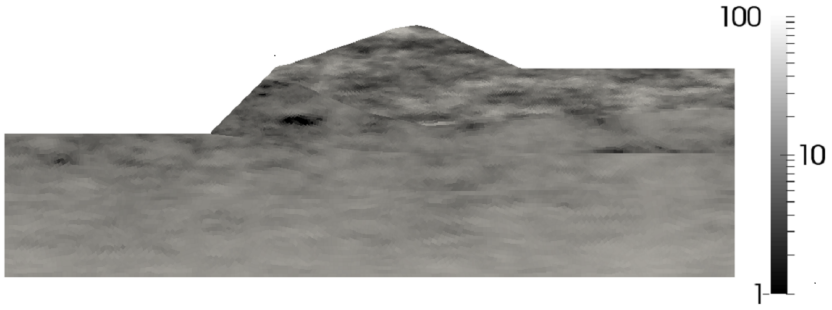

(b)

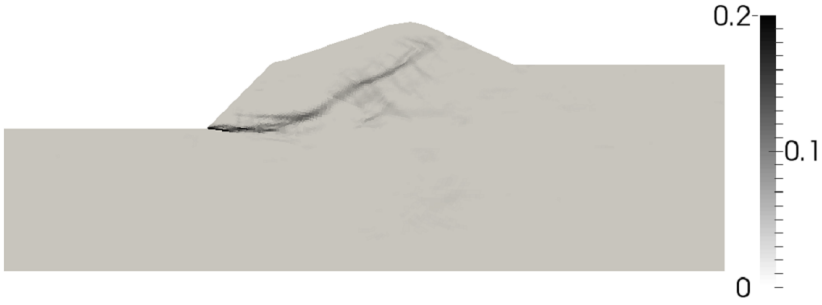

(c)

Figure 4.6: Analysis of embankment after ditch excavation: (a) the finite element mesh of North row; (b) example random field of undrained shear strength (in kPa on a logarithmic scale); (c) contours of deviatoric strain at slope failure

4.5. ANALYSIS

In each RFEM analysis, 1000 realisations have been performed to obtain a distribution of possible factors of safety (F). For a typical RFEM analysis, Figure 4.7 shows how the mean and standard deviation of F evolve as more realisations are analysed. In this figure, the mean and standard deviation of F have been normalised by their respective values after 1000 realisations. It is seen that 1000 realisations are more than enough to achieve sufficient convergence of the output statistics for interpreting the results.

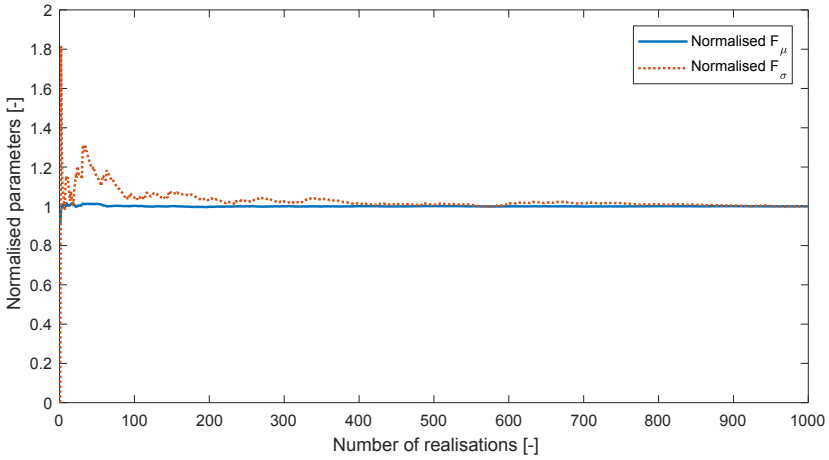

Figure 4.7: Illustration of convergence of mean and standard deviation of F in typical RFEM analysis

4.5.1. RELIABILITY AT INITIAL CONDITIONS

Figure 4.8 presents the results of RFEM and deterministic analyses carried out for the initial condition; that is, before excavation of the ditch had commenced. This was analysed using a comparable finite element mesh to Figure 4.6(a), but with a horizontal ground surface in place of the ditch. For each RFEM analysis, the results are presented as (a) a cumulative distribution function (cdf), and (b) a probability density function (pdf). A pdf defines the range of possible factors of safety and their relative likelihoods, whereas a cdf is the cumulative area under the pdf. In Figure 4.8, the probability of failure predicted by each RFEM analysis is the area under the pdf for $F < 1$, and the reliability is the area under the pdf for $F \leq 1$. Alternatively, the probability of failure is equal to the cdf when $F = 1$, whereas the reliability is equal to (1 – cdf) at $F = 1$. As one would expect for a slope that has remained standing for centuries, the computed probability of failure is almost 0% for the initial condition of the test.

Figure 4.8 compares the results of three RFEM simulations: one based on the statistics obtained from all 17 CPTs but without conditioning of the random fields to the CPT data ("UC all data"); and two further simulations based only on the statistics obtained from the Centre row CPTs, one using random fields conditioned to the Centre row CPTs ("C Centre") and the other using unconditional random fields ("UC Centre"). The figure

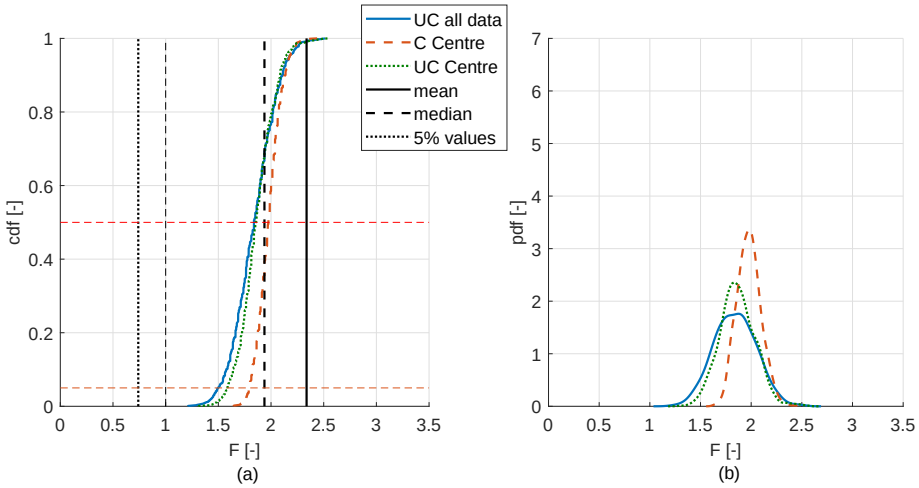

Figure 4.8: Comparison of deterministic (mean, median and 5% values) and RFEM analyses for initial condition of dyke (prior to excavation of the ditch): (a) cdf; (b) pdf

shows that there is a relatively small difference between the unconditional distributions of factor of safety obtained using statistics of the material parameters derived from only the Centre row CPTs or from all CPTs, and that, for R = 95% (given by cdf = 0.05), the respective values of F are 1.59 and 1.50. Moreover, F = 1.50 may be compared with factors of safety of 0.74, 1.94 and 2.34 from deterministic analyses based on the 5-percentiles, medians and means of the distributions of undrained shear strength for each soil layer, respectively. It is seen that, in almost all cases, the RFEM realisations return a much lower factor of safety than that computed based on mean strengths, due to failure being attracted to weaker zones and avoiding (where possible) the stronger zones; indeed, Figure 4.8 shows the deterministic solution based on mean strengths to be the upper bound solution in this instance. Conversely, the RFEM realisations generally return a much higher factor of safety than that computed based on the 5-percentile strengths, due to the averaging of property values along potential failure planes. Figure 4.8 also shows that the uncertainty in the dyke response is reduced when conditioning the random field against the Centre row CPT measurements, as indicated by the narrower range for the cdf and pdf. Specifically, for R = 95%, based on the statistics derived from the Centre row CPTs, F increases from 1.59 to 1.79 if the random fields are conditioned to the CPT data. Overall, it is clear from Figure 4.8 that a consideration of the spatial correlation of soil properties has a significant impact on the stability assessment. Whereas assessments based on mean strengths may be un-conservative, those based on 5-percentiles may be significantly over-conservative and lead to costly re-designs and mitigation measure

4.5.2. RELIABILITY AT THE FINAL STAGE OF FAILURE TEST

Figure 4.9 summarises results obtained for various drawdown levels during the final stage of the field test, as obtained by RFEM analyses based on unconditional random fields and

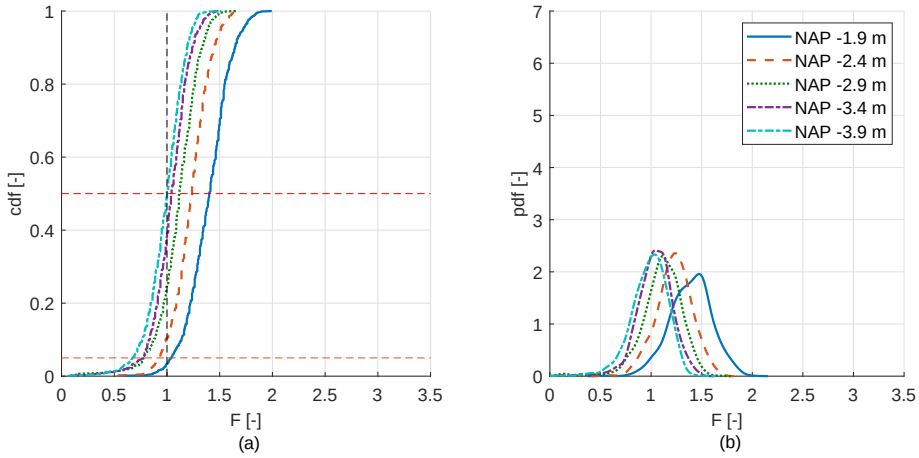

Figure 4.9: Unconditional RFEM analyses for different levels of drawdown: (a) cdf; (b) pdf

Table 4.4: Evolution of failure probabilites (in %) as a function of drawdown level

	Drawdown level to [NAP]				
	-1.9 m	-2.4 m	-2.9 m	-3.4 m	-3.5 m
Unconditional	3.25	10.50	25.00	38.75	50.00
North row	<0.25	<0.25	<0.25	3.50	11.25
Centre row	<0.25	<0.25	0.50	0.60	3.60
South row	<0.25	<0.25	<0.25	0.75	2.25

a finite element mesh similar to that in Figure 4.6(a). By the start of the final stage, the ditch had been excavated to its maximum depth of 2.5 m, with 1 in 1 side-slopes, and filled with water to the brim of the excavation at a level of NAP –1.9 m. Five drawdown levels (in 0.5 m steps) have been analysed and are shown in Figure 4.9, starting with NAP –1.9 m, and ending with NAP –3.9 m corresponding to the lowest possible drawdown level at which the dyke failure occurred. Once again, the results for each analysis are shown as (a) a cdf and (b) a pdf. Considering dyke failure to be represented by a factor of safety less than 1.0, the probability of failure increases from 3.25% before the start of drawdown, to 10.50%, 25.00%, 38.75% and finally to 50.00% for drawdowns of 0.5 m, 1.0 m, 1.5 m and 2.0 m, respectively. Table 4.4 lists the same results for the drawdown levels relative to NAP, and compares them with the results of RFEM analyses using random fields conditioned on the individual CPT rows, using finite element meshes consistent with the stratigraphy at each cross-section being analysed. These analyses are illustrated in Figure 4.10.

Comparing the probabilities of failure for the different analyses shows a clear difference between the unconditional and conditional RFEM analyses. By conditioning the random fields based on known data at specific locations (i.e., at the CPTs), the range of possible spatial distributions of undrained shear strength for the dyke cross-section reduces. This in turn leads to a smaller range of computed factors of safety when the

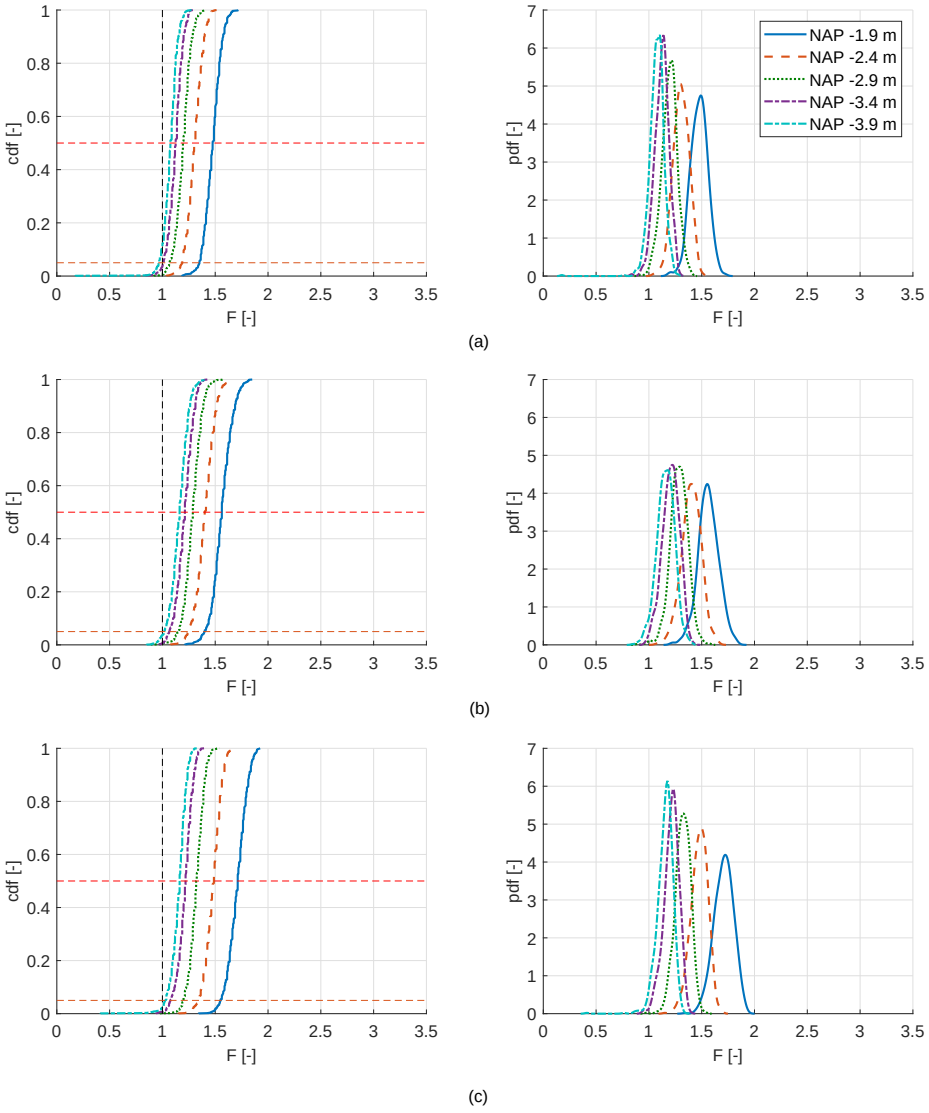

Figure 4.10: Conditional RFEM analyses for different levels of drawdown: (a) North row; (b) Centre row; (c) South row

random fields are used in the RFEM simulations, as is apparent by the factor of safety distributions being narrower in Figure 4.10 than in Figure 4.9. Note, however, that the narrower (conditional) distributions are completely contained within the respective wider (unconditional) distributions.

Figure 4.11 shows the computed failure mechanisms from the weak tail of each pdf (i.e., for those realisations for which $F < 1$), for the three conditional analyses based on the maximum possible drawdown of 2.0 m. The largest number of potential mechanisms is seen for the North cross-section (Figure 4.11(a)) and the lowest number for the South cross-section (Figure 4.11(e)), reflecting the relative differences in failure probability shown in Table 4.4. However, the mechanisms generally follow a similar trend; that is, failure tends to initiate at the bottom of the peat layer, or just inside the clay layer; it then continues just above or just below the boundary between the two layers, before turning upwards and exiting the ground surface on the outward sloping face of the dyke. This mechanism is consistent with the deterministic solution based on mean layer strengths (factored down to trigger failure), as shown by the thicker lines drawn on three cross-sections. It is also consistent with measurement data from the test itself, as recorded using inclinometers positioned at the locations indicated in Figure 4.2. This included 3 inclinometers in-line with the Centre row CPTs, plus single inclinometers between the North and Centre rows, and between the Centre and South rows. Figure 4.11(c) includes the horizontal displacements recorded at the Centre cross-section at three times; just before failure t0 and at two times (separated by around 1 minute) during the failure, t1 and t2. It is seen that failure occurs suddenly and involves large horizontal displacements. Moreover, the measurements indicate a similar failure surface location and geometry to the numerical analyses. Figures 4.11(b) and 4.11(d) show the displacements recorded by the inclinometers located between rows, which for convenience have been plotted relative to the stratigraphies at the North and South rows, respectively. The measurements indicate that failure was confined to the southern half of the failure test, and visual observations, including a filmed recording, of the test itself confirmed that failure started between the Centre and South rows. This is at variance with the RFEM results, which suggest a greater tendency to fail at the Northern end of the test, although the failure probabilities in Table 4.4 and Figure 4.10 also indicate that the three rows are in similar states as failure of the dyke is approached.

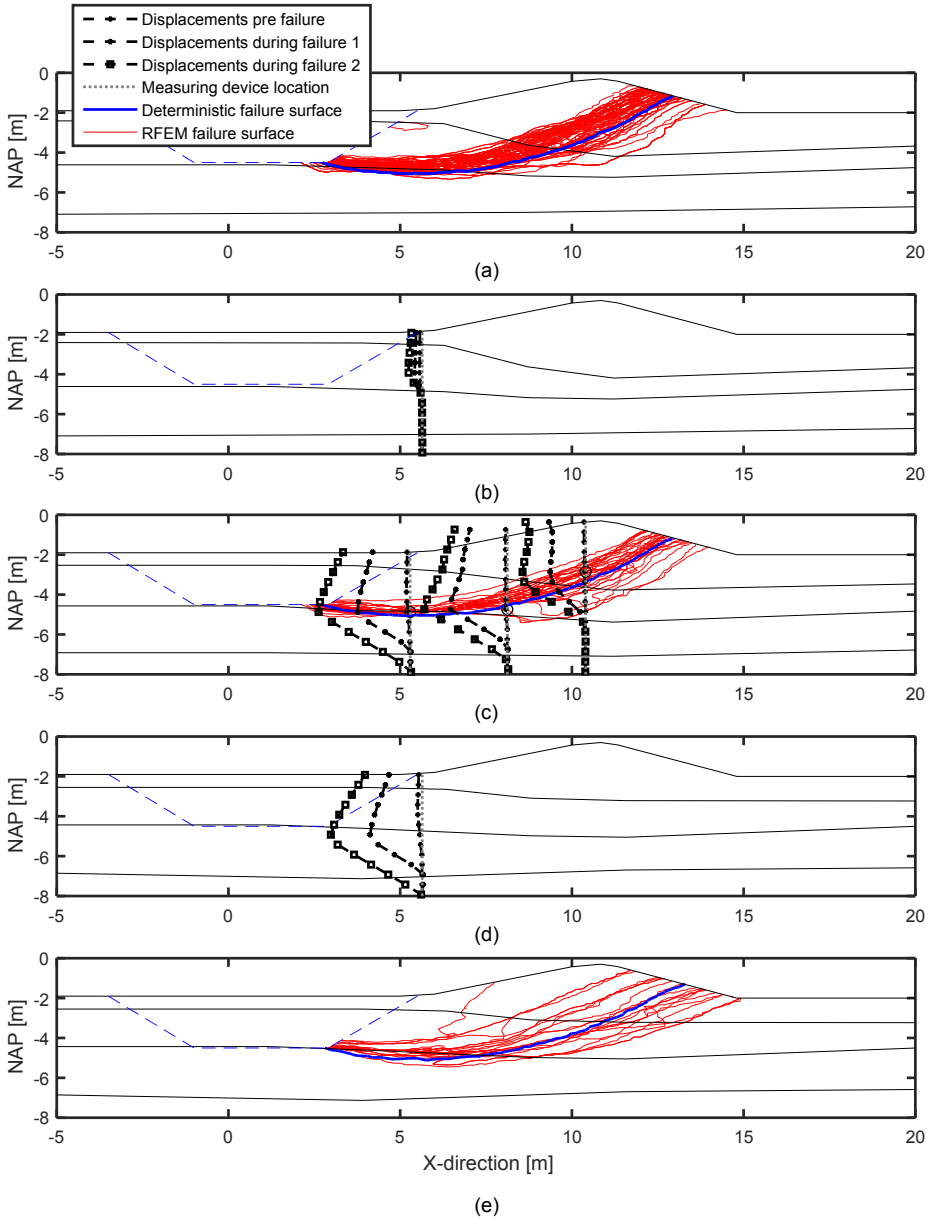

Figure 4.11: Computed failure mechanisms for 2.0 m drawdown, and comparison with deterministic mechanisms and measured horizontal displacements (to scale): (a) North row; (b) between North and Centre rows; (c) Centre row; (d) between Centre and South rows; (e) South row

4.6. DISCUSSION

The failure probabilities approaching failure, listed in Table 4.4, are supplemented in Table 4.5 by the (a) 5th percentile, (b) 50th percentile (i.e., median) and, (c) mean factors of safety back-figured from the probability distributions in Figures 4.9 and 4.10. This table shows that for all analyses, there is very little (or no) difference between the median and mean values of F, thereby reinforcing the impression given in Figures 4.9 and 4.10 that the distributions of F are approximately symmetrical. The table also shows that the mean values of F obtained from the conditional simulations are around 10-15 % greater than the mean values for the corresponding unconditional simulations, which is slightly surprising given that both sets of simulations are based on the same statistics that have been derived from the same CPT data. While it is clear that conditioning the random fields will result in a reduction in the standard deviation of F, as is apparent by comparing the widths of the distributions in Figures 4.9 and 4.10, it might seem counter-intuitive that all three cross-sections return mean values of F that are greater than that for the unconditional simulation. However, from the CPT data in Figure 4 it may be observed that the s_u profiles have a tendency to be stronger under the dyke (most likely due to the extra load imposed and consequential consolidation of the soil layers). As these profiles are in the immediate vicinity of the failure mechanism and therefore more influential, this is the likely explanation for the increase in mean factors of safety.

Because, for any stage in the failure test, the conditional distribution of F is narrower than in the unconditional simulation, and has a higher mean, the probability of failure is smaller in the conditional simulations. Table 4.4 shows that, whereas the probability of failure increases steadily in the unconditional analyses as the drawdown level lowers, it remains very low in the conditional analyses until the drawdown moves between NAP –3.4 m and NAP –3.9 m, whereupon there is a rapid increase in the failure probability. Between these two drawdown levels, corresponding to the approximate situation at failure in the test, the computed probability of failure in the unconditional analysis rises from 38.75% to 50.00%, giving a strong indication of failure. Conversely, at NAP –3.9 m, the computed probabilities of failure in the conditional analyses vary between 2.25% and 11.25%, which, although an indication that failure may be imminent (or has been reached), is not conclusive. This may in part be a reflection of the failure itself initiating between the Centre and South rows, rather at the cross-sections that have been analysed. However, it may also be a sign that, while conditioning the random fields significantly reduces the uncertainty in the influence of the spatial variability on the dyke performance, there are other uncertainties that have not been accounted for which may be influential (van den Eijnden & Hicks, 2019). The narrower distributions also mean that any additional load, reduction in strength or any additional factors (e.g. partial factors as in Eurocode), for example governing the amount of safety margin or confidence in material parameters, has the potential to decrease the calculated reliability more strongly than for the unconditional analyses or analyses based on point statistics.

Overall, for the two larger drawdowns considered of 1.5 m and 2.0 m, the failure probabilities in Table 4.4 and factors of safety in Table 4.5 are reasonably consistent with the outcome of the failure test. However, no account has been taken of the case history's three-dimensionality, other than to consider three cross-sections along the length of the failure test. Chapter 2 conducted simple comparative deterministic analyses in 2D

Table 4.5: Evolution of safety factors back-figured from Figures 10 and 11 as a function of drawdown level: (a) based on 5th percentile; (b) based on 50th percentile; (c) based on mean

		Drawdown level [NAP]				
		-1.9 m	-2.4 m	-2.9 m	-3.4 m	-3.9 m
Unconditional	5th percentile	**1.04**	**0.93**	**0.79**	**0.76**	**0.67**
North row		1.35	1.19	1.07	1.01	0.96
Centre row		1.40	1.24	1.15	1.06	1.02
South row		1.55	1.34	1.20	1.08	1.03
		(a)				
Unconditional	50th percentile	**1.40**	**1.24**	**1.12**	**1.04**	**1.00**
North row		1.48	1.30	1.19	1.12	1.08
Centre row		1.56	1.40	1.29	1.21	1.16
South row		1.71	1.49	1.32	1.22	1.16
		(b)				
Unconditional	mean	**1.39**	**1.23**	**1.11**	**1.04**	**0.98**
North row		1.48	1.30	1.20	1.12	1.07
Centre row		1.56	1.40	1.29	1.21	1.16
South row		1.71	1.48	1.32	1.21	1.15
		(c)				

and 3D, and demonstrated an increase in F of around 15% (due to end effects) when analysing the problem in 3D. However, no account was taken of spatial variability, and it is clear from the field test that 3D variability has a significant impact on the mechanism location and extent. Previous parametric studies by Hicks & Spencer (2010); Hicks *et al.* (2014); Hicks & Li (2018), investigating the influence of spatial variability in 3D analyses of embankment slope stability, have shown that the reliability may be lower in 3D than in 2D due to the tendency for discrete failures to initiate in weaker zones in the direction of the embankment length.

4.7. CONCLUSIONS

A reliability-based analysis framework, accounting for uncertainty arising from the spatial variability of soil properties, has been validated for the controlled, well-instrumented slope failure of an historic dyke in the Netherlands. Using soil property statistics derived from the results of laboratory and CPT data for the different soil layers at the site, the dyke was analysed for the initial (i.e., operating) conditions, as well as for the later stage of the test leading up to failure. The computed probabilities of failure and back-figured factors of safety were broadly consistent with the point at which failure occurred in the test, as was the range of possible failure mechanisms. However, it was not possible to detect the correct location of the failure mechanism in the third dimension, suggesting that the consideration of 3D variability and 3D analysis may be important in such assessments.

It has been shown that, by considering the spatial nature of soil variability, there is a significant reduction in the calculated uncertainty of the structure response, particularly with respect to deterministic and stochastic assessments based only on the point statistics (i.e., the mean and standard deviation) for which there is a much larger range of possible solutions. For example, for the initial configuration of the dyke, a deterministic

assessment based on mean soil properties gave an upper bound (unsafe) solution for the factor of safety, due to failure mechanisms in reality seeking out the weakest path. Conversely, a deterministic assessment based on 5-percentile strengths gave a lower bound (and highly over-conservative) solution, due it failing to account for the averaging of properties along potential failure planes.

The results have shown how the uncertainty in dyke assessments may be further reduced, by conditioning analyses to actual site (e.g., CPT) data, and that, for practical (i.e. high) levels of slope reliability, the probability of failure generally reduces as more data is used. However, the results have also highlighted that conditional results can be under-cautious without a proper consideration of other sources of uncertainty than those associated with spatial variability, e.g. 3D effects, and that they may be important and should be considered. The reliability-based approach provides a rational framework for quantifying the effects of uncertainties, and enables more informed stability assessments that could make the difference between a dyke being assessed as safe or requiring costly improvement.

REFERENCES

Alonso, E. E. (1976). Risk analysis of slopes and its application to slopes in canadian sensitive clays. *Géotechnique* **26**, No. 3, 453–472.

Ang, A. & Tang, W. (1984). *Probability concepts in engineering planning and design: Decision, risk and reliability*. Wiley.

Been, K. & Jefferies, M. G. (1985). A state parameter for sands. *Géotechnique* **35**, No. 2, 99–112.

Cami, B., Javankhoshdel, S., Yacoub, T. & Bathurst, R. J. (2018). 2d spatial variability analysis of sugar creek embankment: Comparative study. In *Advances in Numerical Methods in Geotechnical Engineering* (Shehata, H. & Desai, C. S., eds.), Cham: Springer International Publishing, pp. 118–125.

Campanella, R. G., Wickremesinghe, D. S. & Robertson, P. K. (1987). Statistical treatment of cone penetrometer test data. In *Proceedings of the 5th International Conference on Applications of Statistics and Probability in Soil and Structural Engineering*, vol. 2, pp. 1011–1019.

Cho, S. E. (2007). Effects of spatial variability of soil properties on slope stability. *Engineering Geology* **92**, No. 3, 97–109.

de Gast, T., van den Eijnden, A. P., Vardon, P. J. & Hicks, M. A. (2018). A practical case study of slope stability analysis using the random finite element method. *NUMGE2018* , 531–534.

de Gast, T., Vardon, P. J. & Hicks, M. A. (2017). Estimating spatial correlations under man-made structures on soft soils. *Geo-risk 2017* **GSP 284**, 382–389.

de Gast, T., Vardon, P. J. & Hicks, M. A. (2019a). Assessment of soil variability for linear infrastructure. *Submitted for review* .

de Gast, T., Vardon, P. J. & Hicks, M. A. (2019b). Observations and considerations regarding estimating horizontal scales of fluctuation around linear infrastructure. *ISGSR 2019* , 340–345.

El-Ramly, H., Morgenstern, N. R. & Cruden, D. M. (2002). Probabilistic slope stability analysis for practice. *Canadian Geotechnical Journal* **39**, No. 3, 665–683.

El-Ramly, H., Morgenstern, N. R. & Cruden, D. M. (2003). Probabilistic stability analysis of a tailings dyke on presheared clay-shale. *Canadian Geotechnical Journal* **40**, No. 1, 192–208.

El-Ramly, H., Morgenstern, N. R. & Cruden, D. M. (2005). Probabilistic assessment of stability of a cut slope in residual soil. *Géotechnique* **55**, No. 1, 77–84.

Fenton, G. A. & Griffiths, D. V. (2008). *Risk assessment in geotechnical engineering*. John Wiley and Sons, Inc.

Fenton, G. A., Naghibi, F. & Hicks, M. A. (2018). Effect of sampling plan and trend removal on residual uncertainty. *Georisk: Assessment and Management of Risk for Engineered Systems and Geohazards* **12**, No. 4, 253–264.

Griffiths, D. V. & Fenton, G. A. (1993). Seepage beneath water retaining structures founded on spatially random soil. *Géotechnique* **43**, No. 4, 577–587.

Hicks, M. A. (2005). Risk and variability in geotechnical engineering. *Géotechnique* **55**, No. 1, 1–2.

Hicks, M. A. & Boughrarou, R. (1998). Finite element analysis of the nerlerk underwater berm failures. *Géotechnique* **48**, No. 2, 169–185.

Hicks, M. A. & Li, Y. (2018). Influence of length effect on embankment slope reliability in 3D. *International Journal for Numerical and Analytical Methods in Geomechanics* **42**, No. 7, 891–915.

Hicks, M. A., Nuttall, J. D. & Chen, J. (2014). Influence of heterogeneity on 3D slope reliability and failure consequence. *Computers and Geotechnics* **61**, 198 – 208.

Hicks, M. A. & Onisiphorou, C. (2005). Stochastic evaluation of static liquefaction in a predominantly dilative sand fill. *Géotechnique* **55**, No. 2, 123–133.

Hicks, M. A. & Samy, K. (2002). Influence of heterogeneity on undrained clay slope stability. *Quarterly Journal of Engineering Geology and Hydrogeology* **35**, No. 1, 41–49.

Hicks, M. A. & Spencer, W. A. (2010). Influence of heterogeneity on the reliability and failure of a long 3D slope. *Computers and Geotechnics* **37**, No. 7, 948 – 955.

Hicks, M. A., Varkey, D., van den Eijnden, A. P., de Gast, T. & Vardon, P. J. (2019). On characteristic values and the reliability-based assessment of dykes. *Georisk: Assessment and Management of Risk for Engineered Systems and Geohazards* **13**, No. 4, 313–319.

Javankhoshdel, S., Luo, N. & Bathurst, R. J. (2017). Probabilistic analysis of simple slopes with cohesive soil strength using RLEM and RFEM. *Georisk: Assessment and Management of Risk for Engineered Systems and Geohazards* **11**, No. 3, 231–246.

Jiang, S.-H., Li, D.-Q., Cao, Z.-J., Zhou, C.-B. & Phoon, K.-K. (2014). Efficient system reliability analysis of slope stability in spatially variable soils using Monte Carlo simulation. *Journal of Geotechnical and Geoenvironmental Engineering* **141**, No. 2, 04014096.

Li, Y., Hicks, M. A. & Vardon, P. J. (2015). High performance computing strategies for nonlinear finite element analysis of long heterogeneous soil slopes. In *Proceedings of the 3rd UK Conference of the Association for Computational Mechanics in Engineering, Swansea (United Kingdom)*, pp. 427–430.

Li, Y. J., Hicks, M. A. & Vardon, P. J. (2016). Uncertainty reduction and sampling efficiency in slope designs using 3D conditional random fields. *Computers and Geotechnics* **79**, 159–172.

Lloret-Cabot, M., Fenton, G. A. & Hicks, M. A. (2014). On the estimation of scale of fluctuation in geostatistics. *Georisk: Assessment and Management of Risk for Engineered Systems and Geohazards* **8**, No. 2, 129–140.

Lloret-Cabot, M., Hicks, M. A. & van den Eijnden, A. P. (2012). Investigation of the reduction in uncertainty due to soil variability when conditioning a random field using kriging. *Géotechnique Letters* **2**, No. July-September, 123–127.

Muraro, S. (2019). *The deviatoric behaviour of peat: a route between past empiricism and future perspectives*. Ph.D. thesis, Delft University of Technology.

Phoon, K.-K. & Kulhawy, F. H. (1999). Characterization of geotechnical variability. *Canadian Geotechnical Journal* **36**, No. 4, 612–624.

Ponzoni, E. (2017). *Historical constructions on natural silty soils accounting for the interaction withthe atmosphere*. Ph.D. thesis, Università degli Studi di Brescia.

Robertson, P. K. (2009). Interpretation of cone penetration tests — a unified approach. *Canadian Geotechnical Journal* **46**, No. 11, 1337–1355.

Rosenblueth, E. (1972). Point estimates for probability moments. *Proceedings of the National Academy of Sciences* **72**, No. 10, 3812–3814.

van den Eijnden, A. P. & Hicks, M. A. (2017). Efficient subset simulation for evaluating the modes of improbable slope failure. *Computers and Geotechnics* **88**, 267–208.

van den Eijnden, A. P. & Hicks, M. A. (2019). On the importance of a complete characterization of site investigation data uncertainty: a computational example. *ISGSR 2019* , 340–345.

van den Eijnden, A. P., Hicks, M. A. & Vardon, P. J. (2017). Investigating the influence of conditional simulation on small-probability failure events using subset simulation. In *Proceedings of the 6th International Symposium on Geotechnical Safety and Risk*, pp. 130–139.

Vanmarcke, E. (1983). *Random fields, analysis and synthesis*. Cambridge, Mass.: MIT Press.

Vanmarcke, E. H. (1977). Reliability of earth slopes. *Journal of the Geotechnical Engineering Division-ASCE* **103**, No. 11, 1247–1265.

Wickremesinghe, D. & Campanella, R. G. (1993). Scale of fluctuation as a descriptor of soil variability. In *Proceedings of the Conference of Probabilistic Methods in Geotechnical Engineering*, pp. 233–239.

5

SUMMARY AND CONCLUSIONS

The work presented in this thesis links a controlled field experiment where a dyke was brought to failure, via a theoretical investigation into the accuracy of quantifying spatial correlation using Cone Penetration Test (CPT) data, to a statistical analysis of the field experiment conducted using the Random Finite Element Method (RFEM).

In the failure experiment, a site investigation and laboratory investigation were performed, and the subsequent failure design, failure monitoring, execution and analysis provided insight and data relating to the behaviour during normal operation, as well as during the experiment where the dyke was stressed in steps up to failure.

In a site-investigation to assess the stability of a dyke, CPT provides data at close (vertical) intervals, which can be used to estimate the vertical spatial correlation. Estimating horizontal scales of fluctuation provides more of a challenge for which this thesis provides guidance.

The comparison of a calculation including spatial variation with the failure experiment, shows that the method is capable of predicting realistic probabilities of failure taking account of the spatial variability of material properties.

5

5.1. DYKE FAILURE EXPERIMENT

A controlled experiment in which an existing dyke was brought to failure by saturating the dyke and excavating a ditch in front of it was presented in chapter 2. To prepare for the test, an extensive site investigation was performed, consisting of CPTu tests and borings to collect material used in laboratory testing. Based on the site investigation, sensors were installed to track the behaviour of the dyke during the experiment; these included horizontal and vertical deformation sensors and pore water pressure sensors.

Using a wetting system on top of the dyke, before the start of the experiment the dyke was saturated. Initially, a small ditch was excavated in front of a 50 m dyke length and filled with water. Then, to generate displacements in the dyke, the water in the ditch was first lowered by 1.0 m, and the cross-sectional area of the ditch then increased twice by additional excavation; the first increase in size generated larger displacements and the second induced the failure. This approach provided a large amount of pre-failure data that have been analysed by several master students and Muraro (2019) of the Geo-Engineering Section of Delft University of Technology.

The size and location of the excavated ditch were designed using Limit Equilibrium Method (LEM) analyses, and the displacements and pore pressures during the test have been modelled using Finite Element Method (FEM). In these numerical analyses, variation in material properties were not taken into account. The results of the deterministic numerical analyses and data of the failure experiment have similar features. The calculated displacements and water pressures follow the same trend as the observed displacements and water pressures.

5.2. MEASURING SPATIAL VARIATION

Two methods for estimating the scale of fluctuation of soils in both the vertical and horizontal directions were introduced and compared in chapter 3. Using either an auto-correlation function or an Non-uniform Discrete Fourier Transform (NDFT) has been shown to give equally accurate results, and can therefore be seen as viable alternative

methods.

From a theoretical investigation using synthetically generated data, the importance of the amount and spacing of information for making a reliable estimate of the Scale of Fluctuation (SoF) was demonstrated. A method has been proposed for estimating the Coefficient of Variation (CoV) of the calculated SoF. The accurate estimation of the horizontal SoF using CPT within a budget is a difficult task, given the large range of values that may be expected for θ_h. However, grouping CPTs can yield an improved estimate of the SoF with limited CPTs, given no prior knowledge of the SoF.

The field data considered show a distinct difference between the vertical and horizontal scales of fluctuation. Based on these data, the horizontal scale of fluctuation was better represented by the weighted average of two component scales of fluctuation, whereas the vertical scale of fluctuation was adequately described by a single scale of fluctuation.

5.3. COMBINING THE DYKE FAILURE WITH SPATIAL VARIATION

In the last technical chapter, the failure described in Chapter 2 has been analysed including estimates of the spatial variation discussed in Chapter 3. The conditions before the experiment started and at failure were compared in a series of numerical analyses using both deterministic FEM and RFEM approaches. The observed and calculated failure modes were similar, although the computed factors of safety differed significantly depending on the adopted approach (deterministic FEM versus RFEM) and on the relative use of data (i.e. conditional versus unconditional analysis). Accounting for soil variability allows the quantification of uncertainty, and by incorporating spatial variability the confidence in the stability assessment can be increased. By incorporating the measurement data at specific locations (i.e. by conditioning random fields), the confidence can be further increased. As the uncertainty of the spatial variation decreases, other uncertainties e.g. model uncertainty and transformation uncertainty start playing a larger role in the overall assessment.

5.4. RECOMMENDATIONS FOR FURTHER RESEARCH

While, in this work, progress has been made in reducing uncertainties in dike assessment, there are several opportunities to further reduce uncertainties, which may lead to more robust and less (over-) conservative assessments.

One of the main uncertainties, not discussed in this thesis, is the transformation uncertainty in going from observed material behaviour, in either insitu or laboratory experiments, e.g. CPT and triaxial tests including uncertainties related to different operators (Kardan *et al.*, 2016), to material properties for soil models (Ching *et al.*, 2016). An attempt should be made to unify the different results from laboratory test programmes in order to further characterise correlations between material parameters. There is a substantial amount of data held in different databases. One leap forward in the understanding of geotechnical structures will come from fully utilising these databases. This can be in (further) determining uncertainty in material parameters, different distributions and correlations for the material properties for different constitutive models, and characteristic values for different geotechnical structures.

For indicating the strength of a dyke, the material and the deposition of the material is of importance. In this thesis only the material uncertainty is considered. Geometric uncertainties have not been taken into account, although they may play an important role for critical dyke sections.

With a greater understanding of the theoretical and practical (geotechnical) structural responses to the effects of spatially correlated properties, the required characteristic material properties can be chosen based on the spatial variability found at the site and geotechnical structure considered. This requires several benchmark studies not only for slope stability but other geotechnical structures as well (Varkey *et al.*, 2019).

Other uncertainties have yet to be well characterised. For example, in this study the uncertainties regarding the phreatic level have not been taken into account (as a total stress analysis was used). Moreover, soil atmosphere interaction can be implemented in order to show the stability factor based on past and future climate and weather predictions (as this is a major driver of the water forces) (Jamalinia *et al.*, 2019).

Moving to possible new assessment methods, including post-failure effects, requires calculation methods that are able to predict the behaviour of the geotechnical structure under large deformations. If the size and shape of a failure can be predicted, the subsequent consequences, e.g. rate of flooding, can be used in choices of maintenance. MPM (Wang *et al.*, 2019; González Acosta *et al.*, 2019; Remmerswaal *et al.*, 2019) can be a good tool to assist in full system and consequences analysis.

REFERENCES

Ching, J., Phoon, K.-K. & Wu, T.-J. (2016). Spatial correlation for transformation uncertainty and its applications. *Georisk: Assessment and Management of Risk for Engineered Systems and Geohazards* , 1–18.

González Acosta, J. L., Vardon, P. J., Remmerswaal, G. & Hicks, M. A. (2019). An investigation of stress inaccuracies and proposed solution in the material point method. *Computational Mechanics* **Ahead of print**.

Jamalinia, E., Vardon, P. J. & Steele-Dunne, S. C. (2019). The effect of soil-vegetation-atmosphere interaction: a numerical study. *Environmental Geotechnics* **Ahead of print**.

Kardan, C., Viking, K., Nik, L. & Larsson, S. (2016). Influence of operator performance on quality of CPTu results. *Proceedings of the 17th Nordic Geotechnical Meeting* , 153–158.

Muraro, S. (2019). *The deviatoric behaviour of peat: a route between past empiricism and future perspectives*. Ph.D. thesis, Delft University of Technology.

Remmerswaal, G., Hicks, M. A. & Vardon, P. J. (2019). Influence of residual dyke strength on dyke reliability using the random material point method. *ISGSR 2019* , 775–780.

Varkey, D., Hicks, M. & Vardon, P. J. (2019). An improved semi-analytical method for 3D slope reliability assessments. *Computers and Geotechnics* **111**, 181–190.

Wang, B., Hicks, M. A. & Vardon, P. J. (2019). Slope failure analysis using the random material point method. *Géotechnique Letters* **6**, No. 2, 113–118.

ACKNOWLEDGEMENTS

For this thesis to come to its full completion I would like to thank my supervisory team Mike and Phil for the discussions their support and their ability to enrich my English vocabulary. I would also like to thank my PhD committee who added insightful comments in the final stage of completion. Special thanks to Henk who started my early reasearch carreer at bachelor level and who was instrumental in initiating this work.

The field test would not have been able to have been performed was it not for Hoogheemraadschap van Rijnland combining a 'normal' project with a research opportunity. The design of the field test would not have been possible without the collaboration with Cristina, with whom all the design choices have been discussed in detail, or the help of my university colleagues, Stefano, Elisa and Hong-Fen, for their work in the laboratory. The site investigation, additional lab tests, monitoring and management of the field test was able to become a success by the valuable collaborations with Wiertsema & partners, Inpijn-Blokpoel, Structon, Gemeentewerken Rotterdam and Deltares. For their help of installing miscellaneous equipment or performing last minute tests at the site I would like to thank all colleagues and students who sacrificed their time behind the computer to help at the site. The field test would not have been carried out to the quality it is was it not for the contractor Gebroeders van der Poel and their patience and ability reaching the required accuracy requested when working with academia.

I would like to especially thank Bram and Divya for our many discussions on RFEM, helping me by running the RFEM analysis on the SURFsara grid and sharing their experience in setting-up the analysis and analysing the result.

I will never forget the support of Tilly, my parents, my brothers, and my friends – who all supported me unconditionally and allowed me the freedom to focus on starting and completing this thesis and reminding me to relax or allowing me to vent every now and then.

For their financial contribution to this work I would like to thank RPS, STOWA, provinces Noord-Holland, Zuid-Holland & Utrecht, Hoogheemraadschappen van Rijnland, Delfland, Hollands Noorderkwartier & de Stichtse Rijnlanden, Wetterskip Fryslân, Waternet, Waterschap Rivierenland, Deltares, Plaxis and NWO.

CURRICULUM VITÆ

Tom DE GAST

28-03-1986 Born in Den Helder, the Netherlands.

EDUCATION

2014–2020 Ph.D. Candidate in Geotechnical Engineering
Technische Univeristeit Delft, the Netherlands
Thesis: Dykes and Embankments: a Geostatistical Analysis on Soft Terrain
Promotor: prof. dr. M. (Michael) A. Hicks
Promotor: dr. P. (Philip) J. Vardon

2009–2013 Master of Science, Civil Engineering (Geo-Engineering)
Technische Univeristeit Delft, the Netherlands

WORK

2018–current Geo-Engineering Consultant & Researcher
RPS advies- en ingenieursbureau, Delft

2014–current Ph.D. Candidate Geo-Engineering
Delft University of Technology, Delft

2013 Junior Researcher Geo-Engineering
Delft University of Technology, Delft

2012–2013 Geotechnical Researcher (Master thesis)
Shell Global Solutions, Rijswijk

2011–2013 Project Engineer Geo-Engineering and Water Safety (part-time)
RPS advies- en ingenieursbureau, Delft

2009–2011	Junior Project Engineer Geo-Engineering (part-time) Fugro Ingenieursbureau B.V., Leidschendam
2008–2009	Geotechnical Researcher (Bachelor thesis) STOWA, Utrecht & Wiertsema en partners, Tolbert
2008	Project Engineer Geo-Engineering (internship) Hoogheemraadschap van Delfland, Delft
2006	Site Supervisor (internship) Witteveen+Bos B.V., Deventer

LIST OF PUBLICATIONS

- T. de Gast, P. J. Vardon & M. A. Hicks, Assessment of soil variability for linear infrastructure, *Submitted for review*
- T. de Gast, M.A. Hicks, A. P. van den Eijnden, & P.J. Vardon, On the reliability assessment of a controlled dyke failure, *Submitted for review*
- M. A. Hicks, D. Varkey, A. P. van den Eijnden, T. de Gast, & P. J. Vardon (2019). On characteristic values and the reliability-based assessment of dykes, *Georisk: Assessment and Management of Risk for Engineered Systems and Geohazards*, **13**, No. 4, 313-319.
- T. de Gast, P.J. Vardon & M.A. Hicks (2019), Observations and considerations regarding estimating horizontal scales of fluctuation around linear infrastructure, *Proceedings of the 7th International Symposium on Geotechnical Safety and Risk*, pp. 340-345.
- T. de Gast, A.P. van den Eijnden, P.J. Vardon & M.A. Hicks (2018), A practical case study of slope stability analysis using the Random Finite Element Method, *Proceedings of the 9th European Conference on Numerical Methods in Geotechnical Engineering (NUMGE 2018)*, pp. 531-534.
- T. de Gast, P.J. Vardon & M.A. Hicks (2018), Detection of soil variability using CPTs, *Proceedings of the 4th International Symposium on Cone Penetration Testing (CPT18)*, pp. 289-294.
- T. de Gast, P.J. Vardon & M.A. Hicks (2017), Estimating spatial correlations under man-made structures on soft soils, *Proceedings of the 6th International Symposium on Geotechnical Safety and Risk*, pp. 382-389.
- T. de Gast, P.J. Vardon, C. Jommi & M.A. Hicks (2015), The history of safety factors for Dutch regional dykes, *Proceedings of the 5th International Symposium on Geotechnical Safety and Risk*, pp. 364-370.